The Dissertation Committee for Micah Sivan Glaz Certifies that this is the approved version of the following dissertation:

Morphological Effects of Organic and Inorganic Semiconducting Materials by Scanning Probe Microscopy

Committee:

David A. Vanden Bout, Supervisor

Lauren J. Webb

Xiaoyang Zhu

Bradley J. Holliday

Brian A. Korgel

Morphological Effects of Organic and Inorganic Semiconducting Materials by Scanning Probe Microscopy

by

Micah Sivan Glaz, BS

Dissertation

Presented to the Faculty of the Graduate School of

The University of Texas at Austin

in Partial Fulfillment

of the Requirements

for the Degree of

Doctor of Philosophy

The University of Texas at Austin

December 2012

Dedication

To my mom and dad for being such wonderful and supportive parents.

To my brother, Josh, my sister-in-law Jackie and their three terrific kids, Jonah, Jordan, and Jaelyn. I love you all.

Acknowledgements

This work is a collaboration of many different people. I am thankful for all their support. This process could not have been possible without them, and for that I am grateful.

First, I'd like to thank Prof. David Vanden Bout, for his support and guidance as my advisor. His optimism, ideas, and thoughtfulness helped mold and make me the scientist I am today.

I'd also like to thank Prof. Ananth Dodabalapur for his support in our collaboration and inviting me to spend time with his research group in Singapore.

I worked directly with a number of people to create this dissertation, including Dr. David Ostrowski, Dr. Brian Goodfellow, Dr. Vahid Akhavan, and Dr. Christopher Lombardo. David and I built the optical setup needed to take most of the measurements, while Brian and Vahid's inorganic solar cell samples started an excellent collaboration between our groups. Chris and I worked together to write two manuscripts on lateral devices. The lateral organic photovoltaics couldn't have happened without his invaluable expertise and guidance. I'd like to thank everyone in my IGERT traineeship, especially Dr. Ken Shih and Annie Harding who taught me the importance of collaboration and that graduate school is more than just working in the lab. Finally, I'd like to thank some of my closest graduate school friends and co-workers, Dr. Takuji Adachi, Amy Bonaparte, Dr. Ryan Cheng, Katie Clark, Dr. Craig Cone, Michelle Fox, Dr. Raluca Gearba, Marlene Gutierrez, Dr. Zhongjian Hu, Shauna Ingle, Katherine Koen, Sai Konda, Leigh Krueger, Andrew Martinez, Dr. Zach Pozun, Oleksiy Slobodyan, Rye Terrel, Jon Travis, Dr. Katie Walker and Ting Yan; you all have been extremely helpful in getting me to this day.

Morphological effects of Organic and Inorganic Semiconducting Materials by Scanning Probe Microscopy

Micah Sivan Glaz, Ph. D.

The University of Texas at Austin, 2012

Supervisor: David A. Vanden Bout

Solution deposition of thin film photovoltaic materials leads to large variations in the morphological and chemical compositions of the film. In order to improve device functionality, it is important to understand how morphology and chemical composition affects charge generation, separation, and collection. This PhD work will first study bulk methods in order to characterize materials in solution and films. The results are then correlated with microscopy studies examining morphology. Other methods used in this PhD work will directly couple spectra and microscopy. Microscopic regions of such films and devices can be illuminated using scanning confocal microscopy or near-field scanning optical microscopy (NSOM), which allows for one to directly probe regions of the film at or below the optical diffraction limit. By scanning the sample over a fixed laser spot we can simultaneously create image maps of the topographical, electrical and optical properties. This technique, known as laser beam induced current (LBIC) allows one to directly probe a local area of a device with 100-300nm resolution. Along with bulk device efficiency studies, near field and confocal data of inorganic and organic materials are investigated. These include devices fabricated with a blend of P3HT (poly[3-

hexylthiophene]) and perylene diimide derivatives, and Cu(InxGa1-x)Se2 [CIGS] nanoparticle devices. Finally, we use a new device architecture, a lateral organic photovoltaic (LOPV) in order to spatially resolve transport in functional organic devices.

Table of Contents

List of Tables

List of Figures

Chapter 1: Introduction to Dissertation: Using scanning probe microscopy to study the effects of morphology on organic and inorganic semiconductors

Chapter 1: Dissertation Overview

As the world becomes more energy dependent with technological advances increasing energy consumption, we need ways to consume less energy and low cost sources of renewable energy. Solution deposited thin film semiconductors made from conjugated polymers, small molecules, or inorganic nanoparticles offer cheap and efficient methods compared to their alternative more expensive bulk inorganic counterparts. Although the most widely used solar cell, silicon, has shown efficiencies upward to 23%, the high processing temperatures and low absorption coefficients have inhibited lower costs preventing wider spread use of the technology.[1-3] Solution deposited materials, on the other hand have shown more versatility because of their low temperature processing and ability to be deposited on flexible substrates. Nanoparticles, for example, such as $Cu(In_{1-x}Ga_x)Se_2$ [CIGS], provide higher stability, but still suffer from low efficiencies and morphological effects. However, there is a lack of understanding the fundamental chemistry and physics of solution deposited materials, which is believed to be the reason for the low efficiencies.[4-18]

Organic materials are of great interest because of the ability to tune the separation of the HOMO and LUMO levels in order to collect more of the solar spectrum.

Furthermore, high absorption coefficients allows for the use of less materials. In order to make charge transfer favorable and overcome the Coulomb attraction of the electron and hole, the difference in energies of the donor and acceptor materials must be greater than 0.1-0.3 eV .[19, 20] However, organic materials have limited efficiencies, 5-10%, due to their low stability, small dielectric constants, and small exciton diffusion lengths as well as high Coulombic attraction of the electron-hole pair. The best organic devices are fabricated by creating bulk heterojunctions (BHJs), which are complex mixtures of polymers and molecules.

As shown in Figure 1, the morphology of the BHJ film varies with domains ranging from crystalline to amorphous consisting of phase segregated aggregates of the donor and acceptor materials. [21],[22] The morphology of a film affects the interface between the donor and acceptor and makes it difficult to understand how charge separation and transfer occurs. Charge separation happens at the interface between donor and acceptor materials and may be affected by morphological changes. However, the mixing of the donor and acceptor materials makes probing the location of exciton separation difficult.

Many analytical techniques are used to study the morphology of mixed blends using a number of techniques, including atomic force microscopy (AFM), kelven probe force microscopy (KPFM), electrostatic force mircroscopy (EFM), photoconductive AFM (PC-AFM), near-field optical microscopy, and confocal microscopy. AFM techniques have the unique ability to measure surface topography at the nanoscale. The non-contact AFM technique works by attaching a probe to a cantilever, which oscillates

at a specific frequency. A drive voltage oscillates the tip at its peak frequency, while a laser is reflected off the cantilever on to a diode to monitor the tip oscillation. As the tip approaches the sample, the tip interacts with the sample governed by van der Waals forces. These forces dampen the oscillation, and the tip can then be held at a constant height above the sample using a feed back loop. Atomic resolution has been achieved using noncontact AFM. However, AFM only measures surface topography and is not chemically specific.

AFM has been coupled with other techniques in order to simultaneously characterize the electrical or optical properties and the topography. For example, KPFM has the unique ability to measure the local work function of a material. This method was used to measure the work function of oligothiophene aggregates,[23] change in photovoltages after photobleaching,[24] as well as correlating morphology to charge trapping.[25] EFM along with time resolved EFM has been used to spatially resolve the time it takes for charging to occur in films and relate it to changes in the composition of blends.[26] Lastly, an AFM tip has been used as a top electrode, in which the photocurrent is collected through the tip (PC-AFM).[27]

Our work focuses on two methods, NSOM and scanning confocal microscopy. Confocal microscopy simply uses a focused laser to image a sample. By scanning the sample across the focused beam, an optical image is formed pixel by pixel. NSOM, on the other hand, produces a topographic and optical image. It has been described elsewhere, but briefly images are collected using a Topometrix Aurora NSOM.[28-30] The

NSOM probes are made in house by coating a tapered single mode fiber optic with ~100nm of aluminum at the end of the tip. The sizes of the tips were imaged using scanning electron micrographs and it was found the apertures are 75-100 nm. The NSOM tips are mounted on to a tuning fork and the tip is held at a constant height above the sample at ~5 nm using a piezo-electric stage detected by shear force. Excitation of 370 nm light was coupled into the fiber optic by first frequency doubling the emission from a Ti:Sapphire laser. Near the near-field probe is an evanescent electric field, which is laterally confined by the size of the aperture and is used to excite the sample to obtain the optical image. The fluorescence is collected through a 0.6 NA objective and is focused onto an avalanche photodiode. Scanning the stage, while holding the tip at a constant distance, creates a topographical and optical image of the sample.

Scanning confocal microscopy along with NSOM has been used to not only study the optical and topography properties, but to also measure the local photocurrent simultanesously.[31-33] The work in this dissertation attempts to understand some of the underlying effects of morphology by studying multilayer organic light emitting diodes (OLEDS), vertical and lateral organic photovoltaics (LOPVs) and inorganic PVs with the use of near-field scanning optical microcopy (NSOM) and scanning confocal microscopy. By developing techniques to study morphology in solution, thin films, and under device operation we hope to further the understanding of how morphology affects device functionality and explain charge separation and transfer in a range of semiconductor materials.

Chapter 2: Morphology of bilayers in OLEDs

In Chapter 2 NSOM is used to understand the morphology of bilayer organic light emitting diodes in order to understand dewetting of the electron transporting layers (ETLs) for OLEDs. The ETL is a polymer or small molecule electrolyte that is spin cast on top of the emissive layer. Because of the water insolubility of most light emitting organic molecules or polymers, the water soluble electrolytes can be directly spin cast over the top layer to create a bilayer device. The electrolytes are important for OLEDs because it lowers the turn on voltage by creating an interfacial dipole at the interface of the emissive layer and the ETL. While the polymer electrolytes are more stable, the small molecules are more mobile on the surface. Small molecules are easier to synthesis and purify making them preferable for OLED applications in comparison to polymers that can have many defects, polydispersity, and are difficult to purify. The dewetting process not favorable and is not well understood and is needed to better understand the effects of ETL layers.[34-36] Atomic force microscopy (AFM) studies have shown the time at which dewetting occur for the small molecule ETL and the formation of islands as a consequence. Even after dewetting of the ETL layer, the devices still worked more efficiently than if no ETL layer was added to the OLED. Although the AFM technique allowed us to see the occurence of dewetting, it did not have chemical specificity which would enable us to quantify the amount of dewetted material. We used near-field scanning optical microscopy in order to further understand this dewetting process. Near-

field has the unique ability to image both the topography and simultaneously optically excite the sample allowing for chemical specificity to study the islands in a dewet sample, as well as the areas in between the islands. [37-41]

Chapter 3: Morphological effects on the photocurrent of $Cu(In_{1-x}Ga_x)Se_2$ Nanoparticles

Chapter 3 describes using scanning confocal microscopy to spatially probe the photocurrent in $Cu(In_{1-x}Ga_x)Se_2$ (CIGS) nanoparticles which are very effective light absorbers. They are a direct bandgap material in the red edge of the solar spectrum with high optical coefficients and are stable under long excitation. Currently, it is very difficult to tune the bulk material due to high temperature and multi-stage evaporation of the materials causing phase segregation and intermetallic phase formation. A method to control this behavior and lower the cost of production is to synthesize nanocrystals with high control of the stoichiometry.[42-44] The nanocrystal "ink" can then be inexpensively casted onto a substrate by drop casting, spin casting, dip coating, or air spraying. This method, however, has shown much lower efficiencies, which in part has to do with the difficulty in controlling and understanding the morphology. In order to increase the efficiencies, a better understanding of the morphology of the crystals must be understood. We built a scanning confocal microscopy setup to simultaneously create image maps of the photocurrent and fluorescence by raster scanning a focused beam across the CIGS

devices. The information was correlated with scanning electron micrographs to understand where photocurrent is being observed and how this correlates to the morphology seen in scanning electron microscope images.

Chapter 4: Supramolecular Aggregation in Solution

In chapter 3 I report on the controlled aggregation of a perylene diimide molecule attached to a polymer backbone. In order to make a device with organic materials, we cannot only account for the properties of a single unit but must understand how the molecules interact as a whole system because of the interactions affecting the optical and electrical properties of a system. Furthermore, it is important the molecules or polymers strongly interact in a well-defined way in order to understand charge separation and transfer. We report that the aggregation of the PDI can be readily controlled by changing the solvent and this aggregation can be quantified using the h-aggregate model developed by Spano et al.[45-50] We find the best solvent leads to the highest extent of aggregation, which is counter-intuitive for molecular aggregation. However, the aggregation is guided by the polymer backbone. In a good solvent, the polymer has a large radius of gyration allowing the pendant molecules to easily align. In a bad solvent, the polymer is collapsed in a more random architecture preventing strong interaction. We also report on the percentage of PDI molecules that are aggregated and the lifetimes of the different states. Figure 2 shows a schematic of the polymer in a good and in a bad solvent.

Chapter 5: Electrical properties of lateral organic photovoltaics for a fundamental

understanding of charge transport

Chapter 5 employs a new device structure developed in Dr. Dodabalapur's group, a lateral organic photovoltaic (LOPV).[51-56] A schematic of such a device is shown in Figure 3, where asymmetric electrodes are fabricated through a two-step photolithography process after which a bulk heterojunction is cast. The length of the channel can range from tens of nanometers to hundreds of microns. Although LOPVs are inefficient, they allow for nanoscale investigation of the BHJ along the transport plane while the device is operated under steady state conditions unlike vertical devices. Many analytical techniques (kelvin probe force microscopy, confocal, etc.) can be used to probe anywhere along the BHJ in order to study charge separation and transport. Theoretical and experimental studies show LOPVs exhibit similar device physics under the same electric fields that are observed in vertical devices. Additionally, these theoretical and experimental studies, which include a confocal microscopy technique used to locally image devices, have shown a space charge region (SCR) exists at each electrode and a recombination zone (RZ) exists in the center of the device. Confocal microscopy on the device reveals high photocurrent (PC) at each of the electrodes and minimal PC in the center. Through confocal microscopy, we can directly study photocurrent and recombination in a single system. We can fit the PC analytically in order to estimate a size of the SCR, which is directly related to the electron and hole mobility, to measure both mobilities in a single experiment under normal operating conditions.

The goal of this project is to understand charge transport in two systems,

Langevin and non-Langevin polymers. The Langevin characteristics of the polymers pertain to the recombination mechanism. If the recombination statistics is bimolecular, it is considered Langervin. However, as the recombination statistics deviate, it is said to become more non-Langevin. Although experimental work has been done to quantify the amount how non-Langevin polymers are, the fundamental understanding of what makes one polymer non-Langevin while another is Langevin is not well understood. This dissertation introduces the first work done using the polymer shown in Figure 4, PSBTBT, donated by the Konarka company for our LOPV devices.

Chapter 6: Photocurrent and fluorescent mapping of P3HT:PDI devices using Near-Field Scanning Optical Microscopy and Scanning Confocal Microscopy

Chapter 6 describes a method for imaging devices with nano- to microscale morphology in organic photovoltaics. Using near-field scanning optical microscopy (NSOM) and scanning confocal microscopy described in earlier chapters, we studied the morphology of poly(3-hexylthiophene) [P3HT] in three different blends based on derivatives of perylene diimide (PDI) because of the combinations resulting in morphological differences as shown in Figure 5.[57] One morphology formed large crystals that were embedded and atop the P3HT, while the second morphology blended well with the P3HT. Finally, the last morphology used the perylene diimide polymer from chapter 4 that phase segregated to form islands of P3HT and islands of PPDI. The photovoltaic

devices were imaged using confocal or near-field microscopy to map the photocurrent, fluorescence, and fluorescence spectra, in order to correlate photocurrent and fluorescence with the chemical composition.

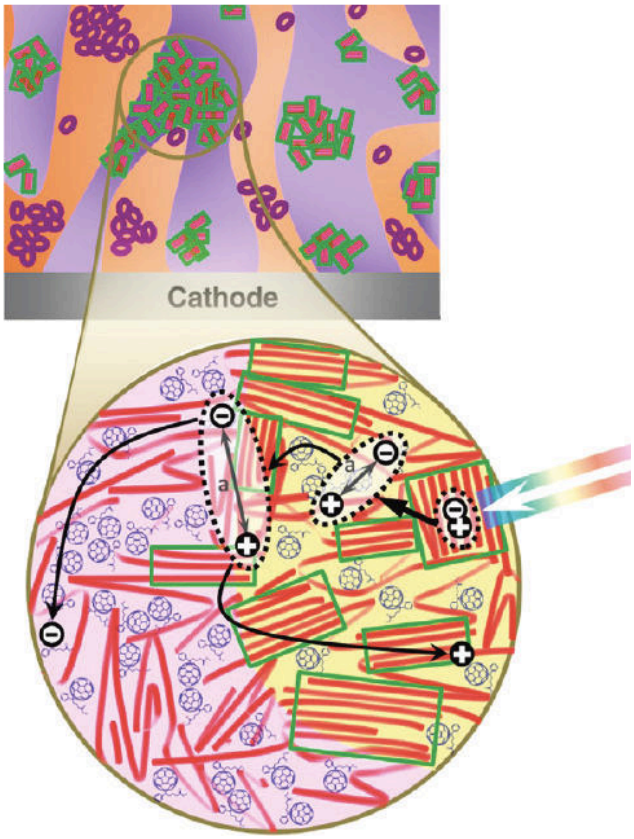

Figure 1.1: Schematic of a bulk heterojunction shows the green box enclosed crystalline, amorphous, and semi-crystalline domains with the polymer and C_{60}-PCBM represented by red lines and spheres, respectively. The image is adapted from the following reference.[21]

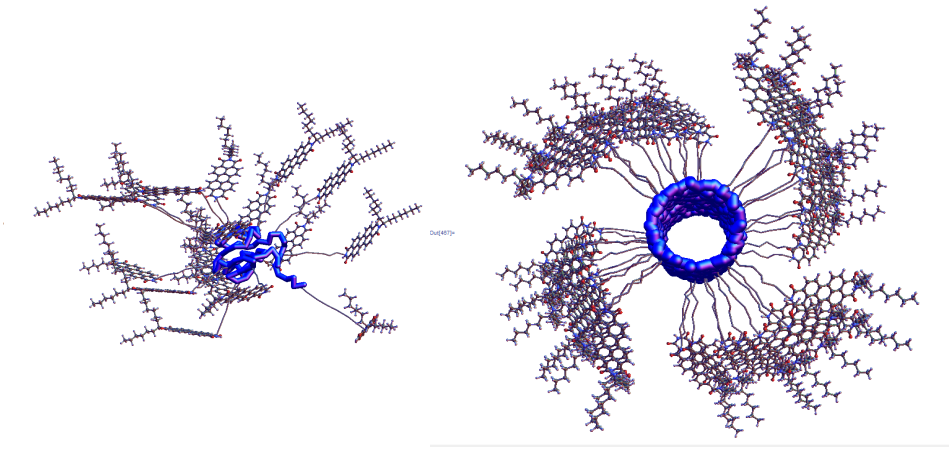

Figure 1.2: Artistic representation of the perylene diimide polymer in a bad solvent (left) and the perylene diimide polymer in a good solvent (right).

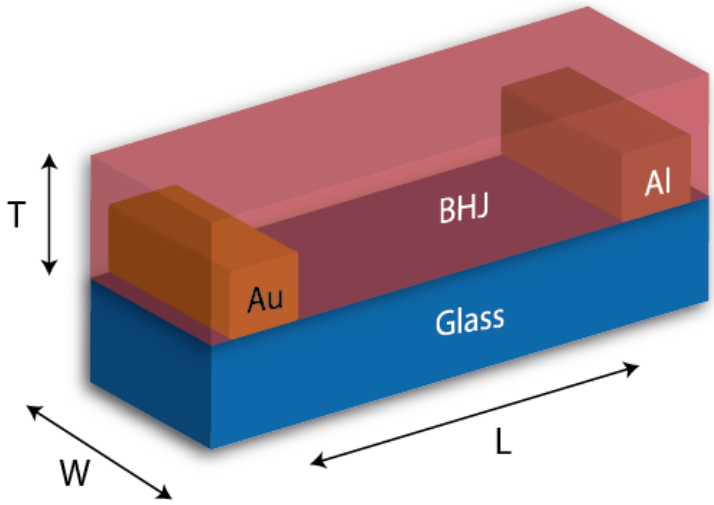

Figure 1.3: Schematic of a lateral organic photovoltaic (LOPV).

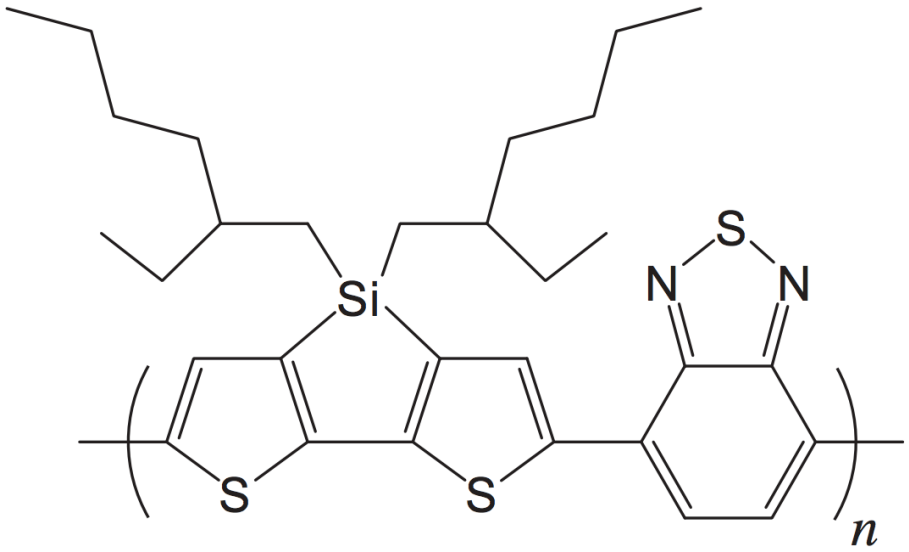

Figure 1.4: PSBTBT polymer donated by the Konarka Company.

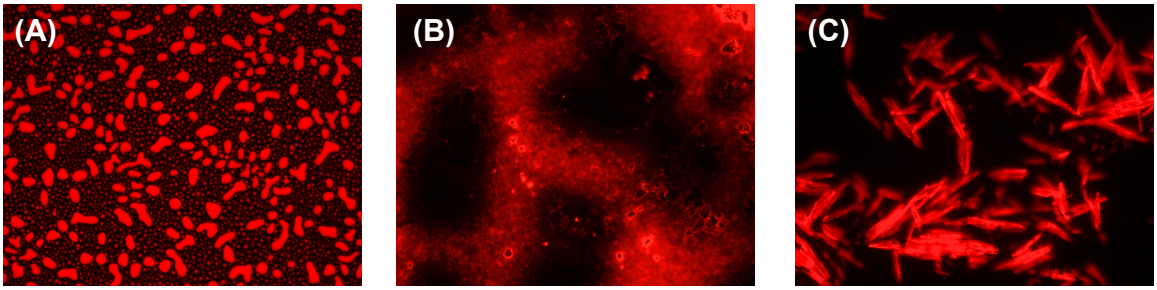

Figure 1.5: Fluorescence microscope images of P3HT:perylene diimide (PDI) blends. (A) P3HT:Poly-PDI, (B) Well blended P3HT:PDI and (C) P3HT:PDI with crystals

1. Green, M. A.; Emery, K.; Hishikawa, Y.; Warta, W.; Dunlop, E. D. *Progress in Photovoltaics: Research and Applications* **2012,** 20, (1), 12-20.

2. Chapin, D. M.; Fuller, C. S.; Pearson, G. L. *Journal of Applied Physics* **1954,** 25, (5), 676-677.

3. Ramanathan, K.; Contreras, M. A.; Perkins, C. L.; Asher, S.; Hasoon, F. S.; Keane, J.; Young, D.; Romero, M.; Metzger, W.; Noufi, R.; Ward, J.; Duda, A. *Progress in Photovoltaics: Research and Applications* **2003,** 11, (4), 225-230.

4. Nelson, J. *Current Opinion in Solid State and Materials Science* **2002,** 6, (1), 87-95.

5. Spanggaard, H.; Krebs, F. C. *Solar Energy Materials and Solar Cells* **2004,** 83, (2–3), 125-146.

6. Coropceanu, V.; Cornil, J.; da Silva Filho, D. A.; Olivier, Y.; Silbey, R.; Bredas, J. L. *ChemInform* **2007,** 38, (29), no-no.

7. Blom, P. W. M.; Mihailetchi, V. D.; Koster, L. J. A.; Markov, D. E. *Advanced Materials* **2007,** 19, (12), 1551-1566.

8. Todorov, T.; Mitzi, D. B. *European Journal of Inorganic Chemistry* **2010,** 2010, (1), 17-28.

9. Emin, S.; Singh, S. P.; Han, L.; Satoh, N.; Islam, A. *Solar Energy* **2011,** 85, (6), 1264-1282.

10. Shaheen, S. E.; Brabec, C. J.; Sariciftci, N. S.; Padinger, F.; Fromherz, T.; Hummelen, J. C. *Applied Physics Letters* **2001,** 78, (6), 841-843.

11. Maturová, K.; van Bavel, S. S.; Wienk, M. M.; Janssen, R. A. J.; Kemerink, M. *Advanced Functional Materials* **2011,** 21, (2), 261-269.

12. Yang, X.; Loos, J.; Veenstra, S. C.; Verhees, W. J. H.; Wienk, M. M.; Kroon, J. M.; Michels, M. A. J.; Janssen, R. A. J. *Nano Letters* **2005,** 5, (4), 579-583.

13. Minemoto, T.; Hashimoto, Y.; Satoh, T.; Negami, T.; Takakura, H.; Hamakawa, Y. *Journal of Applied Physics* **2001,** 89, (12), 8327-8330.

14. Wada, T.; Kohara, N.; Nishiwaki, S.; Negami, T. *Thin Solid Films* **2001,** 387, (1–2), 118-122.

15. Brabec, C. J.; Zerza, G.; Cerullo, G.; De Silvestri, S.; Luzzati, S.; Hummelen, J. C.; Sariciftci, S. *Chemical Physics Letters* **2001,** 340, (3–4), 232-236.

16. Veldman, D.; Ipek, O. z.; Meskers, S. C. J.; Sweelssen, J. r.; Koetse, M. M.; Veenstra, S. C.; Kroon, J. M.; Bavel, S. S. v.; Loos, J.; Janssen, R. A. J. *Journal of the American Chemical Society* **2008,** 130, (24), 7721-7735.

17. Gélinas, S.; Paré-Labrosse, O.; Brosseau, C.-N.; Albert-Seifried, S.; McNeill, C. R.; Kirov, K. R.; Howard, I. A.; Leonelli, R.; Friend, R. H.; Silva, C. *The Journal of Physical Chemistry C* **2011,** 115, (14), 7114-7119.

18. Lee, J.; Vandewal, K.; Yost, S. R.; Bahlke, M. E.; Goris, L.; Baldo, M. A.; Manca, J. V.; Voorhis, T. V. *Journal of the American Chemical Society* **2010,** 132, (34), 11878-11880.

19. Brédas, J.-L.; Cornil, J.; Heeger, A. J. *Advanced Materials* **1996,** 8, (5), 447-452.

20. Alvarado, S. F.; Seidler, P. F.; Lidzey, D. G.; Bradley, D. D. C. *Physical Review Letters* **1998,** 81, (5), 1082-1085.

21. Chen, W.; Xu, T.; He, F.; Wang, W.; Wang, C.; Strzalka, J.; Liu, Y.; Wen, J.; Miller, D. J.; Chen, J.; Hong, K.; Yu, L.; Darling, S. B. *Nano Letters* **2011,** 11, (9), 3707-3713.

22. Uchida, S.; Xue, J.; Rand, B. P.; Forrest, S. R. *Applied Physics Letters* **2004,** 84, (21), 4218-4220.

23. Ostrowski, D. P.; Lytwak, L. A.; Mejia, M. L.; Stevenson, K. J.; Holliday, B. J.; Vanden Bout, D. A. *ACS Nano* **2012,** 6, (6), 5507-5513.

24. Reid, O. G.; Rayermann, G. E.; Coffey, D. C.; Ginger, D. S. *The Journal of Physical Chemistry C* **2010,** 114, (48), 20672-20677.

25. Ellison, D. J.; Lee, B.; Podzorov, V.; Frisbie, C. D. *Advanced Materials* **2011,** 23, (4), 502-507.

26. Giridharagopal, R.; Rayermann, G. E.; Shao, G.; Moore, D. T.; Reid, O. G.; Tillack, A. F.; Masiello, D. J.; Ginger, D. S. *Nano Letters* **2012,** 12, (2), 893-898.

27. Coffey, D. C.; Reid, O. G.; Rodovsky, D. B.; Bartholomew, G. P.; Ginger, D. S. *Nano Letters* **2007,** 7, (3), 738-744.

28. Teetsov, J.; Vanden Bout, D. A. *The Journal of Physical Chemistry B* **2000,** 104, (40), 9378-9387.

29. Kwak, E.-S.; Kang, T. J.; Vanden Bout, D. A. *Analytical Chemistry* **2001,** 73, (14), 3257-3262.

30. Kitts, C. C.; Bout, D. A. V. *The Journal of Physical Chemistry B* **2009,** 113, (35), 12090-12095.

31. Ostrowski, D. P.; Glaz, M. S.; Goodfellow, B. W.; Akhavan, V. A.; Panthani, M. G.; Korgel, B. A.; Vanden Bout, D. A. *Small* **2010,** 6, (24), 2832-2836.

32. McNeill, C. R.; Frohne, H.; Holdsworth, J. L.; Dastoor, P. C. *Nano Letters* **2004,** 4, (12), 2503-2507.

33. Brenner, T. J. K.; McNeill, C. R. *The Journal of Physical Chemistry C* **2011,** 115, (39), 19364-19370.

34. Thejo Kalyani, N.; Dhoble, S. J. *Renewable and Sustainable Energy Reviews* **2012,** 16, (5), 2696-2723.

35. Kulkarni, A. P.; Tonzola, C. J.; Babel, A.; Jenekhe, S. A. *Chemistry of Materials* **2004,** 16, (23), 4556-4573.

36. Chen, Z.; Dang, X.-D.; Gutacker, A.; Garcia, A.; Li, H.; Xu, Y.; Ying, L.; Nguyen, T.-Q.; Bazan, G. C. *Journal of the American Chemical Society* **2010,** 132, (35), 12160-12162.

37. Betzig, E.; Finn, P. L.; Weiner, J. S. *Applied Physics Letters* **1992,** 60, (20), 2484-2486.

38. Higgins, D. A.; Kerimo, J.; Vanden Bout, D. A.; Barbara, P. F. *Journal of the American Chemical Society* **1996,** 118, (17), 4049-4058.

39. Higgins, D. A.; Vanden Bout, D. A.; Kerimo, J.; Barbara, P. F. *The Journal of Physical Chemistry* **1996,** 100, (32), 13794-13803.

40. Teetsov, J.; Vanden Bout, D. A. *Langmuir* **2001,** 18, (3), 897-903.

41. Vanden Bout, D. A.; Kerimo, J.; Higgins, D. A.; Barbara, P. F. *The Journal of Physical Chemistry* **1996,** 100, (29), 11843-11849.

42. Repins, I.; Contreras, M. A.; Egaas, B.; DeHart, C.; Scharf, J.; Perkins, C. L.; To, B.; Noufi, R. *Progress in Photovoltaics: Research and Applications* **2008,** 16, (3), 235-239.

43. Scheer, R.; Walter, T.; Schock, H. W.; Fearheiley, M. L.; Lewerenz, H. J. *Applied Physics Letters* **1993,** 63, (24), 3294-3296.

44. Contreras, M. A.; Egaas, B.; Ramanathan, K.; Hiltner, J.; Swartzlander, A.; Hasoon, F.; Noufi, R. *Progress in Photovoltaics: Research and Applications* **1999,** 7, (4), 311-316.

45. Schwartz, E.; Palermo, V.; Finlayson, C. E.; Huang, Y.-S.; Otten, M. B. J.; Liscio, A.; Trapani, S.; González-Valls, I.; Brocorens, P.; Cornelissen, J. J. L. M.; Peneva, K.; Müllen, K.; Spano, F. C.; Yartsev, A.; Westenhoff, S.; Friend, R. H.; Beljonne, D.; Nolte, R. J. M.; Samorì, P.; Rowan, A. E. *Chemistry – A European Journal* **2009,** 15, (11), 2536-2547.

46. Spano, F. C. *The Journal of Chemical Physics* **2005,** 122, (23), 234701-15.

47. Spano, F. C. *Chemical Physics* **2006,** 325, (1), 22-35.

48. Spano, F. C. *Accounts of Chemical Research* **2009,** 43, (3), 429-439.

49. Cornil, J.; Beljonne, D.; Calbert, J. P.; Brédas, J. L. *Advanced Materials* **2001,** 13, (14), 1053-1067.

50. Otsubo, T.; Aso, Y.; Takimiya, K. *Journal of Materials Chemistry* **2002,** 12, (9), 2565-2575.

51. Ooi, Z. E.; Chan, K. L.; Lombardo, C. J.; Dodabalapur, A. *Applied Physics Letters* **2012,** 101, (5), 053301-5.

52. Lombardo, C. J.; Glaz, M. S.; Ooi, Z.-E.; Vanden Bout, D. A.; Dodabalapur, A. *Physical Chemistry Chemical Physics* **2012,** 14, (38), 13199-13203.

53. Lombardo, C.; Dodabalapur, A. *Applied Physics Letters* **2010,** 97, (23), 233302-3.

54. Lombardo, C.; Danielson, E.; En Ooi, Z.; Dodabalapur, A. *Journal of Photonics for Energy* **2012,** 2, (1), 021007-1.

55. Lombardo, C.; Ooi, Z.-E.; Danielson, E.; Dodabalapur, A. *Organic Electronics* **2012,** 13, (7), 1185-1191.

56. Danielson, E.; Lombardo, C.; Dodabalapur, A. **2012**, 84770F-84770F.

57. Balakrishnan, K.; Datar, A.; Naddo, T.; Huang, J.; Oitker, R.; Yen, M.; Zhao, J.; Zang, L. *Journal of the American Chemical Society* **2006,** 128, (22), 7390-7398.

Chapter 2: Chemical Mapping of an Electron Transporting Layer Using Near-Field Scanning Optical Microscopy

Introduction

Analytical techniques for understanding the morphology of multilayer organic semiconductor devices are critical for developing efficient organic optoelectronic devices. Small molecule conjugated organic electrolytes (COEs) and conjugated polyelectrolytes (CPEs) have shown promise as electron transporting layers (ETL) for polymer light emitting diodes (PLEDs).[1] These electrolytes can enhance the devices by lowering their turn-on voltages. This effect is thought to arise as a result of a self-assembled dipole moment between the emissive layer and the electrode. This dipole in turn lowers the effective work function of the electrode and allows for lower power consumption.[2] COEs and CPEs are also water soluble, allowing for multi-step processing of the layers without intermixing with the emitting layer.[3] Although CPEs make very uniform layers whose thickness can be precisely controlled, COEs display better performance because of greater control of molecular structure and ease of purification.[4] Even though controlling the layer morphology of COEs is more difficult than CPEs, because of their other advantageous properties, they are more promising for PLEDs. Therefore, it is important to determine the effects of morphology on device functionality to understand the mechanism of electron transport in these materials.

Controlling the morphology of COE films is difficult because after deposition the molecules are mobile on the surface. This is due to the fact that in contrast to polymers,

small molecules have higher diffusion constants and are therefore more prone to dewetting. For example, previous studies have shown that when exposed to air, the COE layer dewets from the underlying polymer layer leading to small islands of material. These studies have utilized atomic force microscopy (AFM) experiments to not only probe the formation of these islands but quantified the time it takes for this dewetting to occur. They have shown that the primary dewetting mechanism involves pinholes acting as nucleation sites, followed by increasingly raised features.[5] However, other studies on similar COE materials have also observed that, PLED devices that incorporate an ETL have higher efficiency than devices without this layer despite the dewetting of the COE from the emitting polymer layer.[6] This suggests that the dewetting may be incomplete and a continuous layer of COE could remain behind. To test this hypothesis, we performed near-field scanning optical microscopy to chemically map the COE layer, FPF-BIm_4, on top of an emitting layer of Poly[2-methoxy-5-(2′-ethylhexyloxy-1,4-phenylenevinylene)] (MEH-PPV).

Experimental:

For this study, devices were fabricated, in order to measure the luminance after exposure to air, as previously reported.[4] A typical device structure for the multilayer PLED is shown in Figure 1A. Briefly, poly(ethylenedioxythiophene):poly(styrenesulfonic acid) (PEDOT:PSS), the hole transporting layer, was spin-coated onto indium tin oxide (ITO), followed by Poly[2-methoxy-5-(2′-ethylhexyloxy-1,4-phenylenevinylene)] (MEH-PPV), the light emitting layer, shown in figure 1B. FPF-BIm_4, the ETL, also shown in figure 1B was spin-coated

from methanol on top of the MEH-PPV layer, and Al was thermally deposited to complete the device. In order to characterize the optical properties of these materials, absorption and photoluminescence measurements were performed. Figure 1C and 1D show the absorption and photoluminescence spectra of MEH-PPV and FPF-BIm_4, respectively. The absorption maximum of MEH-PPV, the emissive layer, is at 500 nm, with a minimum near 370 nm, and the emission maximum is at 600 nm. The absorption of the ETL layer, FPF-BIm_4, is blue shifted from MEH-PPV, and steadily increases into the UV. FPF-BIm_4 has an emission maximum at 400 nm, with a long tail that extends out to 550 nm. While the absorption spectra overlapped there is little spectral overlap in the emission spectra of the two species (Figure 1E). This allows one to chemically map the layers using the fluorescence spectrum to identify the composition.

Results and discussion:

Figure 2 shows the luminance of a PLED device containing a FPF-BIm_4/MEH-PPV layer that was exposed to air for 0 to 8 min. Exposure of the FPF-BIm_4/MEH-PPV to air before adding the top electrode lead to devices with a lower luminance. However, even at 8 minutes of exposure, the devices were still more efficient than if no ETL layer was cast. This is consistent with previous studies, which suggest that dewetting is not complete and a residual layer of FPF-BIm_4 remains. Previous microscopy techniques used to study the morphology of the multilayer films, such as AFM, are limited in detecting this residual layer as they only map the topography of the thin film. The current study employs near-field optical microscopy (NSOM) in order to simultaneously probe the topography and the fluorescence of these films to determine if a conformal

layer of FPF-BIm_4 remains. By probing the emission of both the raise features generated during dewetting as well as the thin film materials between them, it is possible to determine if there is a residual FPF-BIm_4 layer.

Figure 3A shows a schematic of the NSOM, which functions by illuminating the sample through a sub-wavelength aperture at the end of a tapered fiber optic probe. This instrument is described in detail elsewhere;[7] briefly, home-pulled fiber optic tips (diameter < 100 nm) are coated with Al and attached to a 100 kHz tuning fork. The tip and tuning fork is mounted above the sample, and the sample is raised to approximately 5 nm below the tip. Excitation of the sample is accomplished by coupling 370 nm laser light into the fiber. The sample is raster scanned using a XYZ piezoelectric stage, which simultaneously creates two images, one of the emission (collected on a single photon counting avalanche photodiode detector) and the second of the surface topography, similar to AFM. Figure 3B and 3C shows the topography and fluorescence images of MEH-PPV/FPF-BIm_4, respectively. The topography image is 10x10 um and shows raised features throughout the image. These raised bumps on the surface are very similar to those previously observed by AFM. The AFM studies assumed these to be FPF-BIm_4 aggregates formed during the dewetting process. NSOM measures not only measure the topography but also a corresponding fluorescence image (Figrue 3C). The total fluorescence image was obtained by removing the excitation with a 400 nm long pass filter. The fluorescence image is not uniform but shows many of the same features found in the topography. In regions of raised topography the total fluorescence is lower (~600 counts) compared to the averages intensity (900 counts/s). Since the raised features are

associated with FPF-BIm_4 that has dewet from the surface, this fluorescence decrease is either due to the FPF-BIm_4 layer having a lower quantum efficiency compared to MEH-PPV or scattering of the excitation light preventing absorption and emission from the MEH-PPV layer. This experiment probes the total fluorescence, which is the sum of the MEH-PPV and the FPF-BIm_4. However, it is also possible to filter the emission to collect only the emission from the FPF-BIm_4.

As seen in Figure 1, the emission of the FPF-BIm_4 can be selectively detected from 380-530 nm by inserting a band pass filter in the emission path before the detector. The band pass filter was centered at 450 nm (range 380-530 nm), which adequately removed all excitation (370 nm), as well as the emission from the MEH-PPV layer. Additonally, the MEH-PPV emission is suppressed due to the small absorbance of the polymer at the excitation wavelength. Figure 4A and 4B show the near-field topography and FPF-BIm4 fluorescence, respectively. The topography image shows similar features as Figure 3B, that have the same raised features. The fluorescence image still correlates strongly to the topography image, however now the raised features in the topography image exhibit increased fluorescence. This confirms that these features are in fact FPF-BIm_4 that has dewet the surface and gathered into clumps on top of the polymer layer. They appear darker in the total fluorescence image since the MEH-PPV has a higher quantum yield than the FPF-BIm_4. Most interesting is the region between these raised features. The FPF-BIm_4 emission between the aggregates on the surface never goes below the background (~100 counts/s). This does indeed prove the FPF-BIm_4 has not completely dewet and a layer is left behind, which is fluorescent. To double check if the

regions that are not raised aggregates do in fact have FPF-BIm_4 images were collected of the identical region for the total fluorescence. Figure 4C and 4D are the respective topography and total fluorescence images collected immediately after Figure 4A and 4B were obtained. The same features appear in both topography image demonstrating the same area was scanned. As before, the image contrast on the fluorescence images is reversed with the total fluorescence showing a reduced emission over the aggregates. This is a result of FPF-BIm_4 effectively blocking the absorption of the excitation in the higher quantum yield MEH-PPV layer. Based on the total emission spectrum in figure 1E one would expect that on average intensity of film in the FPF-BIm_4 image would be about 20% of the intensity in the total image. The observed ratio is slightly lower likely the result of photochemistry as the total fluroscence image was collected after the image of the FPF-BIm_4 and the fact that some of the FPF-BIm_4 has dewet the polymer layer. This result supports the general conclusion that the ETL layer is continuous despite the formation of aggregates upon dewettting.

Conclusions:

In summary, NSOM has been used to map the different compounds in a multilayer LED thin film after dewetting. Overall, luminance measurements show that even after extensive dewetting, the presence of FPF-BIm_4 as an ETL still performs better than devices with no ETL, suggesting that FPF remains as a continuous layer. Using NSOM we probed an FPF-BIm_4 ETL layer on top of MEH-PPV. We've shown that the large FPF-BIm4 islands do not account for the total fluorescence alone and that even after dewetting a continuous layer of FPF-BIm_4 is retained on the surface of the MEH-PPV

layer. In conclusion, the increased device performance upon addition of the ETL layer is due to this continuous FPF-BIm_4 layer. NSOM provides the high spatial resolution and chemical selectivity to map nanoscale features. The utility of NSOM is not limited to these materials and can be used to understand many device architectures. It is a useful technique to understand the morphology of layers within a multiple layer device, and this method could easily be adapted to understand a range of thin film materials in order to gain a more complete picture of the device physics.

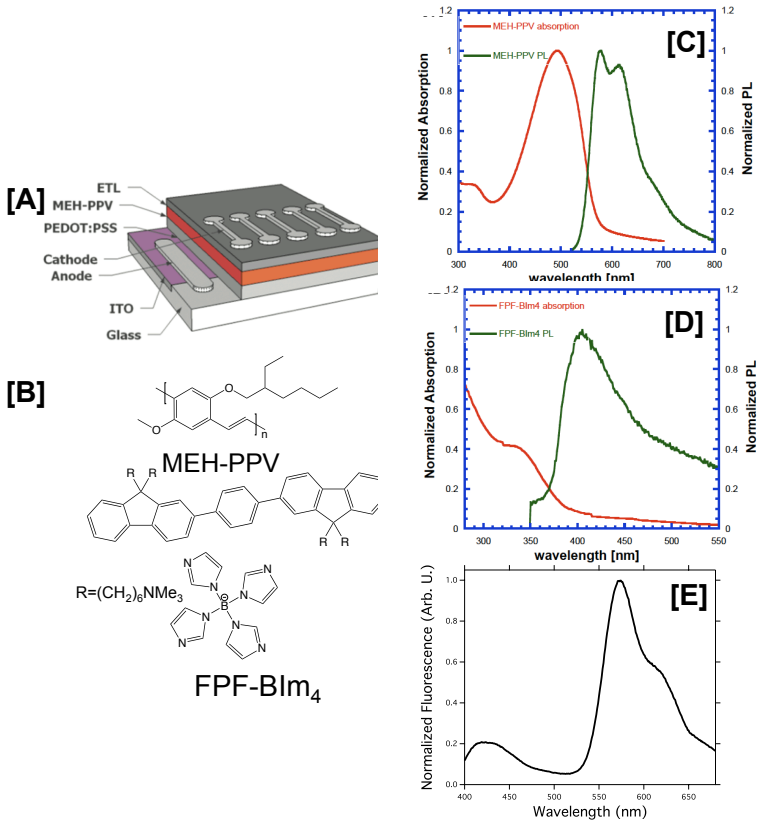

Figure 2.1: A) Schematic of OLED device. B) Molecular structures of MEH-PPV and FPF-BIm_4. C) and D) Absorption and photoluminescne of MEH-PPV and FPF-BIm_4. E) Total fluorescence spectrum of MEH-PPV and FPF-BIm_4

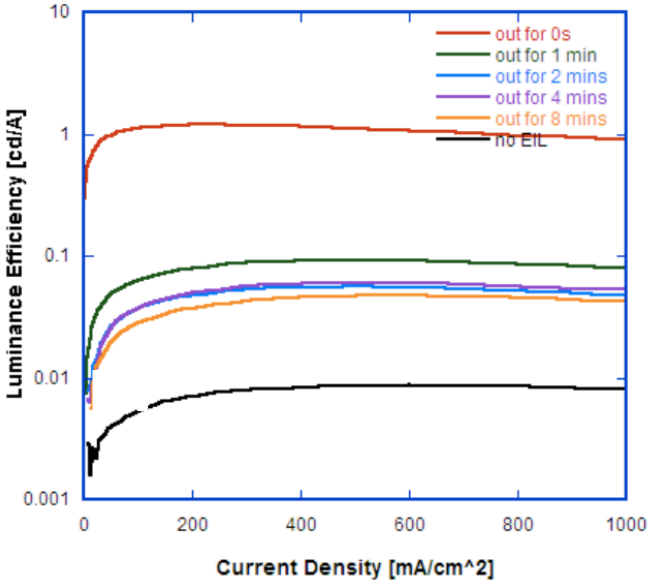

Figure 2.2: Luminance of MEH-PPV:FPF-BIm$_4$ after being exposed to air for 0, 1, 2, 4, 8 minutes, as well as with no additional ETL layer.

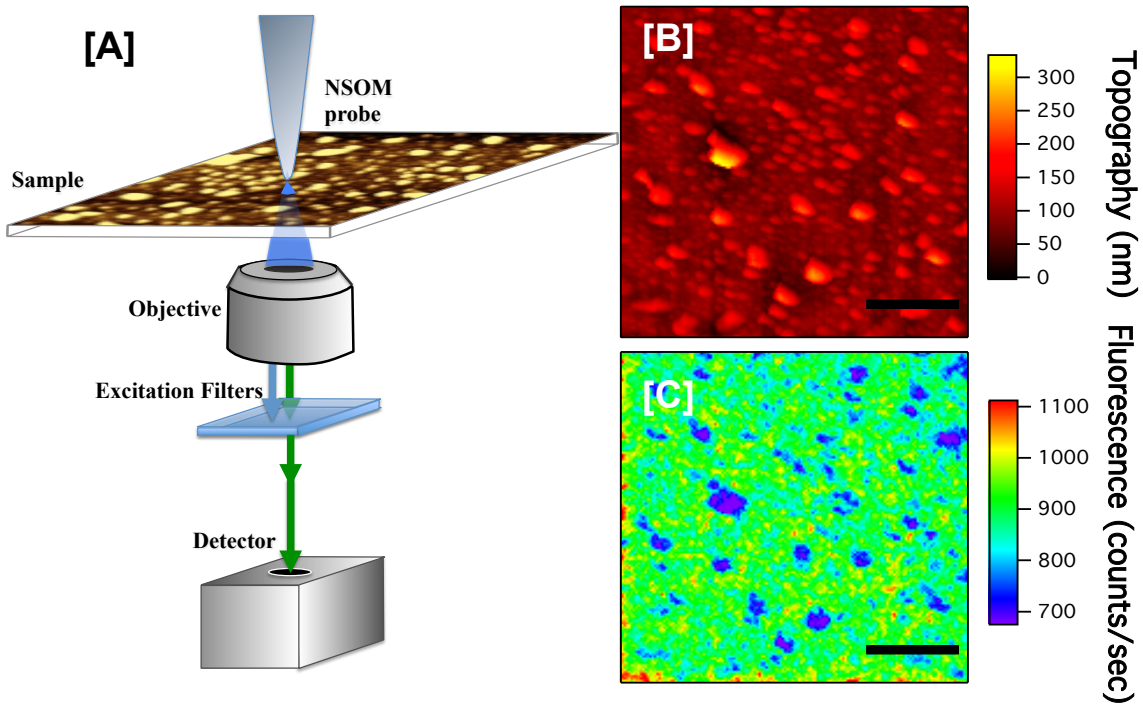

Figure 2.3: A) Near field Optical Microscopy (NSOM) schedmatic. The sample is excited at 370nm through the fiber optic. Emission is collected after filtering of the excitation using an MPD. Near-field images of C) topography and D) fluorescence of MEH-PPV/FPF-BIm$_4$. Fluorescence was obtained by filtering the excitation with a 400nm long pass filter. The scale bar is 2.5 um.

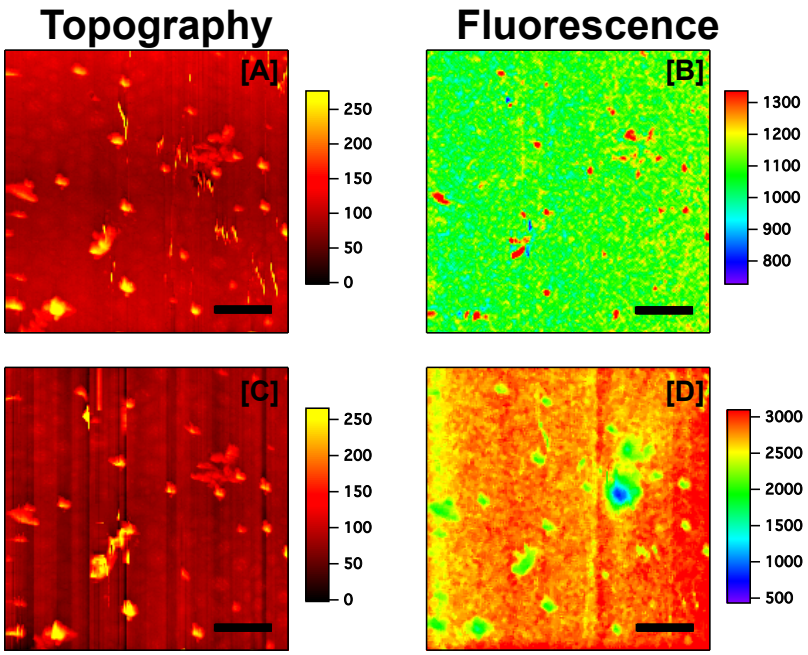

Figure 2.4: Near-Field Scanning Optical Microscopy (NSOM) of FPF-BIm_4/MEH-PPV films excited at 370nm. A) Topography and B) fluorescence were collected simultaneously with a band pass filter between 380nm-500nm in order to collect the FPF-BIM_4 emission. C) Topography and D) fluorescence were collected simultaneously with a long pass filter selected at 400 nm, in order to collect the total fluorescence of the sample.

1. Teunis van, W.; Jurjen, W.; Paul, W. M. B. *Semiconductor Science and Technology* **2006,** 21, (3), 387.

2. Seo, J. H.; Gutacker, A.; Walker, B.; Cho, S.; Garcia, A.; Yang, R.; Nguyen, T.-Q.; Heeger, A. J.; Bazan, G. C. *Journal of the American Chemical Society* **2009,** 131, (51), 18220-18221.

3. Wu, H.; Huang, F.; Mo, Y.; Yang, W.; Wang, D.; Peng, J.; Cao, Y. *Advanced Materials* **2004,** 16, (20), 1826-1830.

4. Kahn, A.; Koch, N.; Gao, W. *Journal of Polymer Science Part B: Polymer Physics* **2003,** 41, (21), 2529-2548.

5. Gong, X.; Wang, S.; Moses, D.; Bazan, G. C.; Heeger, A. J. *Advanced Materials* **2005,** 17, (17), 2053-2058.

6. Liu, G.; Li, A.-Y.; An, D.; Wu, H.-B.; Zhu, X.-H.; Li, Y.; Miao, X.-R.; Deng, W.-L.; Yang, W.; Cao, Y.; Roncali, J. *Macromolecular Rapid Communications* **2009,** 30, (17), 1484-1491.

7. Yang, R.; Xu, Y.; Dang, X.-D.; Nguyen, T.-Q.; Cao, Y.; Bazan, G. C. *Journal of the American Chemical Society* **2008,** 130, (11), 3282-3283.

8. Chen, Z.; Dang, X.-D.; Gutacker, A.; Garcia, A.; Li, H.; Xu, Y.; Ying, L.; Nguyen, T.-Q.; Bazan, G. C. *Journal of the American Chemical Society* **2010,** 132, (35), 12160-12162.

9. Xu, Y.; Yang, R.; Peng, J.; Mikhailovsky, A. A.; Cao, Y.; Nguyen, T.-Q.; Bazan, G. C. *Advanced Materials* **2009,** 21, (5), 584-588.

10. Teetsov, J.; Vanden Bout, D. A. *The Journal of Physical Chemistry B* **2000,** 104, (40), 9378-9387.

11. Barbara, P. F.; Adams, D. M.; O'Connor, D. B. *Annual Review of Materials Science* **1999,** 29, (1), 433-469.

Chapter 3: Mapping Spatial Heterogeneity in Cu(In1−xGax)Se2 Nanocrystal-Based Photovoltaics with Scanning Photocurrent and Fluorescence Microscopy

Introduction

The widespread use of photovoltaic (PV) devices to harvest energy from the sun requires significant reduction in the cost of solar cell technology.[1,2] One approach to lowering manufacturing cost is to use solution-processable materials that can be printed onto various substrates, including plastics, under ambient conditions with high throughput techniques like roll-to-roll printing.[3,4] While many soluble photovoltaic materials have been developed in recent years, the efficiency of these devices is still too low for commercial viability.[5-7] In order to improve efficiency, a more detailed understanding of PV performance is needed. One factor that can limit the performance of thin film PVs is structural, chemical, and electronic heterogeneity in the device.[3,8-16] These variations can occur on the sub-micrometer length scale, thus requiring microscopic techniques that can examine functioning devices with sufficient resolution to observe these kinds of effects. Here, we present a microscopy technique, capable of studying as-fabricated PV devices, that allows local PV performance to be measured with sub-micron resolution and correlated with the optical properties of the materials. The technique is used here to examine PV devices fabricated with $Cu(In_{1-}{}_xGa_x)Se_2$ (CIGS) nanocrystal "inks."

Numerous microscopy techniques have been developed to study local variations in PV performance. Scanning-probe techniques, such as conductive probe atomic force microscopy (AFM) and kelvin force microscopy (KFM), have been used to relate morphology to local variations in properties, including photoresponse and surface potential.[9,17-25] Since these tools operate by monitoring tip-sample interaction, the measurements are localized to the region of the sample directly below the metalized cantilever. These techniques cannot be applied to as-fabricated PV devices, and are instead useful for measuring the electrical properties of model thin films. One way to probe the local photovoltaic response of a device is to only illuminate a small region of the device with a microscopically focused beam of light. Only the light-induced electrical properties of the illuminated region contribute to the measured performance; this technique can map the induced photocurrent and is known as light beam induced current microscopy (LBIC).[24,26-31] The spatial resolution depends on the size of the illumination spot, which through focusing the incident light via a microscope objective can reach the diffraction limit and beyond with near-field techniques. By raster-scanning the device across the focused light spot, a map of local PV response can be generated, highlighting spatial heterogeneities in photocurrent generation across the device.

LBIC measurements have been used to test for fabrication defects and performance quality in silicon-based PVs,[27,32] and to study heterogeneity in organic bulk heterojunction PVs.[24,28-31,33] Most of these studies have utilized conventional microscopy; a few studies achieved higher spatial resolution on the order of 200 nm by utilizing near-field scanning optical microscopy.[28-30,33]

Here we report a novel approach of LBIC microscopy coupled with fluorescence microscopy that we apply to study the response of as-fabricated, functional PV devices. As this technique illuminates the PV through the transparent electrode, there is no need for constructing planar devices[33] or ones with a thin, semi-transparent metal electrode.[28-30] Simultaneous collection of fluorescence and PV response enables spatial correlation of the optical and electronic properties with the morphology of the device. It should also be possible to couple other optical microscopy techniques with the LBIC method, such as time-resolved fluorescence, polarized fluorescence, and absorption or reflection modes, which can yield valuable information into specific PV characteristics such as charge separation, molecular orientation, local crystallinity and absorption.[12,14-16,31] For example, LBIC coupled with Resonance Raman spectroscopy has recently been demonstrated.[31] In addition to imaging, the technique presented here is capable of collecting local voltage-dependent photocurrent data. Here, the technique is applied to a solution-processed CIGS nanocrystal-based PV device.

Results and discussion

Morphology of Spray Casted CIGS

Figure 1A shows the structure of the CIGS nanocrystal PV device that was studied. The device consists of a light-absorbing layer of CIGS nanocrystals deposited on a gold back-contact. Cadmium sulfide (CdS) is added as a buffer layer on top of the nanocrystal layer by chemical bath deposition, followed by a 50 nm thick zinc oxide (ZnO) window layer and 300 nm of indium tin oxide (ITO) deposited by RF sputtering. Figure 1B shows the device response in the dark and under AM1.5 illumination. The

short-circuit current density (J_{sc}), open-circuit voltage (V_{oc}), fill factor (FF), and power conversion efficiency (PCE) were 3.5 mA cm^{-2}, 0.38 V, 0.41, and 0.51%, respectively. Figure 1C shows the wavelength-dependent external quantum efficiency (EQE) measured for the same device. The EQE is a measure of zero-bias current generated per incident photon on the device. The excitation source for the LBIC measurements had a wavelength of 408 nm, on the high energy edge of the EQE spectrum. The shape of the EQE curve is a result of the optical characteristics of both the CIGS nanocrystal absorber layer and the ZnO/ITO window layer.[34]

Figure 3 shows a schematic of the LBIC microscopy setup. The sample is illuminated with 408 nm laser-light focused to a 275 nm diameter spot size. The photogenerated current is measured, along with fluorescence from the sample. As the sample is raster-scanned across the illumination spot, measurements are collected at each step to generate an image map of the measured, local properties.

One challenge of mapping the photocurrent is that the entire device is active but only a microscopic region is being illuminated. The induced photocurrent (IPC) signals from the focused laser spot are on the order of 1 and 40 nA. However, these signals are on top of a comparatively large background from the dark current of the full device, which also varies nonlinearly with applied bias voltage. As such, current amplification and lock-in detection were necessary to obtain sufficient signal to noise. Signal amplification was accomplished with a transimpedance amplifier (or current to voltage converter) built in-house with a gain of 10 000×. The incident light beam is chopped and the output signal of the device is measured with a lock-in amplifier. Therefore, the IPC

that is measured represents the difference between the current measured during illumination and the dark current.

An LBIC image map of a CIGS nanocrystal based PV is shown in Figure 3A. There is significant heterogeneity in device response, with micrometer-scale regions of both increased and decreased IPC generation compared to the average response of the device. The higher performance regions appear filamentary (Region B), while the lowest performance regions have a circular shape with typical diameters of 1–2 μm (Region C). These regions of high and low response are scattered throughout relatively homogeneous regions with average device response (Region A). From the image it is observed that Regions A, B, and C correspond to 75%, 20%, and 5% of the device, respectively (see figure 9). Figure 3B shows the fluorescence microscopy image that was acquired simultaneously with the LBIC measurement. It is clear that the local variations in IPC have corresponding variations in fluorescence. The fluorescence intensity, which relates to the local chemical composition and the extent of radiative charge recombination, is inversely correlated with the IPC signal in the image. For instance, areas of the device like Region C have high fluorescence intensity with low IPC, and areas like Region B show lower fluorescence and exhibit higher IPC (see also supporting information). This is consistent with what one would expect: regions with higher fluorescence have higher radiative recombination and fewer charge carriers available for extraction as IPC.

This technique provides another useful feature: after an image map is collected, the beam can be repositioned to illuminate a selected region of the sample to measure the

local voltage-dependent photocurrent (LVPC). Figure 4 shows the local photocurrent traces obtained at points labeled A, B, and C in Figure 3; the traces are representative of the three distinct types of regions found across the device. The main difference between regions is the magnitude of the photocurrent at zero bias. The general shape of the LVPC curve is similar for the three different regions. There is a slight decrease of ~0.06 V for Region C in the bias at which the LVPC is zero; however, the decrease is close to the error in the voltage measurement of ±0.05 V. This difference may result from lower charge carrier densities in these regions as they have an associated high fluorescence intensity, which is shown to be from CdS (see further discussion below).

It is important to note the LVPC is not the same as the conventional *I–V* response measured with the device exposed to light. As a result of the lock-in detection, the measured current reflects only the additional current induced by the local illumination since the dark current has been subtracted from the signal. This means that the bias at which the LVPC is zero (induced photocurrent equals zero) is not the same as the V_{oc}(total current equals zero). As a result, a local power conversion efficiency cannot be calculated. However, relative efficiencies can be estimated since the only significant difference between the LVPC response of the different regions is the current at zero bias. From the data in Figure 4, the LVPC at zero bias in Regions A, B, and C are 18.3, 31.6, and 11.6 nA, respectively, with an error of ±1.5 nA. Thus, the regions of higher photocurrent are nearly a factor of two more responsive than the average, while the regions of low response are over one-third decreased from the average. It is interesting to consider that if the device was composed entirely of the regions of greatest photocurrent

(Region B), there would be more than 50% enhancement in the power conversion efficiency of the device. While this would still be far below other reported CIGS device efficiencies,[35] these results identify specific pathways for substantially improving the performance of this emerging, solution-deposited photovoltaic system.

The high IPC regions in the device, Regions B, have a filamentary morphology. As shown in Figure 5A, cracks in the nanocrystal films observed by SEM have a similar morphology. Therefore, it appears that these cracked regions are giving rise to the observed increased photocurrent in the device. Higher IPC is most likely due to the fact that the nanocrystal film is thinner in this region and therefore, more of the photogenerated carriers can be extracted from the layer before being eliminated by recombination. Increased photocurrent could also stem from increased interfacial contact area between the CdS layer and CIGS nanocrystal film, as a result of CdS penetrating into the cracks. This type of structure would also require shorter distances for minority charge carriers to travel to reach the interface. These regions also have lower fluorescence (see Figure 3 and Supporting Information), indicating that there is less radiative charge recombination.

AFM images of the CdS buffer layer showed that occasionally large aggregates form in the thin film as a result of homogeneous nucleation in the deposited solution (see Supporting Information). To investigate if Region C areas corresponded to CdS aggregates, fluorescence image maps were separately collected from each layer of the device on glass: ZnO/ITO, CdS, CIGS nanocrystal, and blank glass. While the fluorescence image of the CdS showed highly fluorescent features, Figure 5B, none of

the other layers showed fluorescence contrast. The similarity between the fluorescence images of the CdS films (Figure 5B) and the fluorescence from the device (Figure 3B) confirms that Regions C correspond to places in the device in which the CdS aggregates are present. As the illumination must pass through the CdS layer before reaching the photoactive layer, one possibility for the lower response of these regions is that the aggregate may absorb most of the incident light, limiting transmission to the photoactive CIGS nanocrystal layer. The thickness of the CdS aggregates was assessed with a height analysis of the AFM topography images and the aggregates were found to range from 250 nm to greater than 1000 nm in height. The transmission of the aggregates was estimated to be at most 1.7% for the 250 nm aggregates and even as low as 10^{-4}% transmission for aggregates at 1000 nm.[36] Thus, when the aggregates are present, essentially no light is reaching the photoactive CIGS nanocrystal layer and one may expect the IPC in these regions to drop to zero. However, the IPC in these regions falls by at most half the IPC from that of Region A (average IPC). This could be a result of fluorescence from or incident light scattered off of the aggregates being reabsorbed by the CIGS nanocrystal layer and leading to IPC. Alternatively, light absorbed by the CdS layer may also generate current, albeit not as efficiently as the CIGS nanocrystal layer.

Selenization of CIGS Nanocrystals

In a single step, CIGS films can be deposited with desired composition and crystal phase directly from solution using inks of CIGS nanocrystals. Without high temperature processing, however, devices using these materials have achieved only up to 3% power conversion efficiency (PCE).[38] Hillhouse and Agrawal recently demonstrated 12% PCE

by converting $Cu(In,Ga)S_2$ nanocrystals to CIGS with high temperature selenization.[39,40] They have also explored selenization of $Cu(In,Ga)Se_2$ nanocrystal films, but have not been able to obtain efficiencies greater than only a few percent, claiming that selenized nanocrystal devices perform very poorly unless sulfide nanocrystals are used as starting material and proposed that Se addition leads to a volume expansion needed to eliminated voids in the selenized film.[40]

Nanocrystal dispersions were deposited on the Mo back contacts by spray deposition of 20 mg/ml dispersion of nanocrystals in toluene using a commercial spray gun (Iwata Eclipse HP-CS) operated at 50 psig head pressure. Films were sprayed in one step to a targeted thickness of 1.5 μm. The films were annealed in a hollow graphite cylinder with excess elemental selenium. The cylinder was firmly capped but not gastight. A two-step annealing process was used: 10 minutes at 350°C to remove organic ligands followed by an increase in temperature to 500°C for 1 hour. Excess Se provides a partial pressure to ensure limited loss of selenium content from the particles.

Using the same technique as discussed earlier. We compare two different morphologies the selenization technique in figure 10. The $CuInSe_2$ nanocrystals were very Cu-poor [Cu]/[In]=0.65 and the film sintered with large islands of amorphous material as shown in Figure 10A. This amorphous C/Se coating blocked incident photons from reaching the CIGS crystals underneath, limiting photogenerated current (Figure 1-C). The exposed grains surrounding the larger amorphous islands yield a significantly higher photocurrent than the rest of the device and are the main source of power on this device. The higher efficiency CIGS device had significantly less amorphous coating and

higher density of exposed grains, Figure 10D. These films were much less copper deficient, with [Cu]/[In+Ga]=0.82—similar to that of record efficiency CIGS devices.[37] The LBIC map of this device, 9F, reveals a high spatial density of photoactive regions across the film as compared to the LBIC map of the $CuInSe_2$ device shown in Figure 10.

Conclusion

In summary, microscopic imaging of a CIGS nanocrystal-based PV device has revealed substantial spatial heterogeneity in the photoresponse. Distinct regions of both higher and lower photocurrent could be observed on a variety of length scales ranging from hundreds of nanometers to tens of microns. Two morphological features were found to cause the heterogeneity: CdS aggregates that lowered IPC and cracks in the CIGS nanocrystal absorber layer that produced higher IPC. The performance differences between regions could be quantified using LVPC measurements and show the cracked regions to have had a zero bias photocurrent that was nearly double that of an average region. This information along with the photocurrent maps allow for an estimation of efficiency from a theoretical device composed entirely of the high IPC regions; such a device would have an increase of more than 50% in power conversion efficiency compared to the device studied. Efforts are currently underway to leverage this information to design new fabrication techniques that will improve the device efficiency of CIGS nanocrystal PVs. The coupling of microscopy, spectroscopy, and electrical characterization presented here is applicable not only to these systems but any PV device. As such, direct measurements of how morphology affects performance can be used to guide device design and fabrication in the development of future high efficiency PVs.

Experimental

Synthesis of CIGS Nanocrystal Ink: $Cu(In_{1-x}Ga_x)Se_2$ (x = 0.25 targeted) nanocrystals were synthesized by arrested precipitation using standard Schlenk line techniques as previously reported.[34] The washed and purified CIGS NPs were dispersed in toluene at a concentration of 20 mg mL^{-1} to make the 'ink' used in device fabrication.

CIGS Nanocrystal-Based PV Device Fabrication: Polished float glass substrates with dimensions 25 mm × 25 mm × 1.1 mm (Delta Technologies, Ltd.) were cleaned by sonication in a 50/50 mixture of acetone and isopropanol followed by sonication in deionized water. Each sonication lasted 5 min and was followed by drying in a nitrogen stream. The glass substrates were then exposed to a 100 W oxygen plasma for 5 min to remove any organic residue on the surface. After cleaning, 5 nm of chromium and 60 nm of gold was thermally evaporated to form the metal back contact of the devices. A 600 nm CIGS nanocrystal absorber layer was then deposited by spray coating from an ink (described above) using a commercially available airbrush (iwata Eclipse HP-CS) operated at 50 psig of head pressure. A CdS buffer layer was deposited by a modified chemical bath deposition following procedures outlined by McCandless and Shafarman.[37] The device was placed on a hotplate at 90°C for 5 min after which an aqueous solution of 3 mM cadmium sulfate ($CdSO_4$, Aldrich, 99.999%), 0.53 M thiourea (Fluka, 99.999%), and 8.1 Mammonium hydroxide (NH_3, Fisher, ACS certified) was deposited onto the device which was then covered with a glass petri dish to prevent evaporation. After 2 min, the device was removed from the hotplate and rinsed with deionized water and then left flat to dry. Next a window layer consisting of i-ZnO and

ITO were deposited by RF sputtering. A 50 nm layer of ZnO (target 99.9%, Lesker) was first sputtered in an atmosphere of 0.5% O_2 in Ar (99.95%, Praxair) with a 150 W plasma. This was followed by a 300 nm layer of ITO (target 99.99% In_2O_3: SnO_2 90:10, Lesker) sputtered in an Ar atmosphere (research grade, Praxair) with a 180 W plasma. The final active area of the device was 8 mm^2 (a 4 mm × 2 mm rectangle). A small dab of conductive silver paint (SPI supplies) was placed on all contact pads to improve contact with the testing apparatus.

'Bulk' Photovoltaic Characterization: Conventional *J-V* response was measured with a Keithley 2400 General Purpose Sourcemeter using a Xenon Lamp Solar Simulator (Newport) equipped with an AM1.5 filter as an illumination source. External Quantum Efficiency (EQE) spectra were gathered using a chopper (Stanford Research Systems, model SR540), a lock-in amplifier (Stanford Research Systems, model SR830), a monochromator (Newport Cornerstone 260 1/4M), and a Si photodiode calibrated by the manufacturer (Hamamatsu).

Morphological and Spectral Characterization: Scanning electron microscopy (SEM) images were acquired using a Zeiss Supra 40 VP SEM operating at 10 keV accelerating voltages and using an in-lens detector. Atomic force microcopy (AFM) images were acquired using a Digital Instruments multimode AFM (model MMAFM-2). UV-VIS spectra were collected using an Agilent 8453 UV-VIS.

Photocurrent and Fluorescence Image Maps: The image maps were obtained using a Coherent 408 nm diode laser as the excitation light source, which was focused through a 50x Olympus objective. The size of the focal spot was ~275 nm in diameter as

determined by scanning across a step edge in a patterned metal film. The typical incident laser power was 1.5 μW, which yields a power density of ~2.53 kW cm^{-2} after the light is focused through the objective. For sample scanning capabilities a Physik Instrumente (PI) piezoelectric stage (model E-501.00) was mounted onto a Nikon Diaphot 300 inverted microscope. The excitation beam was chopped at 174 Hz using a Digirad chopper (model C-980) and the photocurrent of the device was amplified 10^4 times using a transimpedance amplifier built in house. The fluorescence was collected using a Perkin Elmer APD (model SPCM-CD290) and the amplified current was collected using an EG&G DSP lock-in amplifier (model 7220). The LVPC curves were obtained by sweeping the applied voltage across the device, sourced from a serial digital to analog (D/A) converter built onto the circuit board of the pre-amplifier, and recording the output signal from the lock-in with a Keithley 2400 General Purpose Sourcemeter. The serial D/A was controlled with LabVIEW.

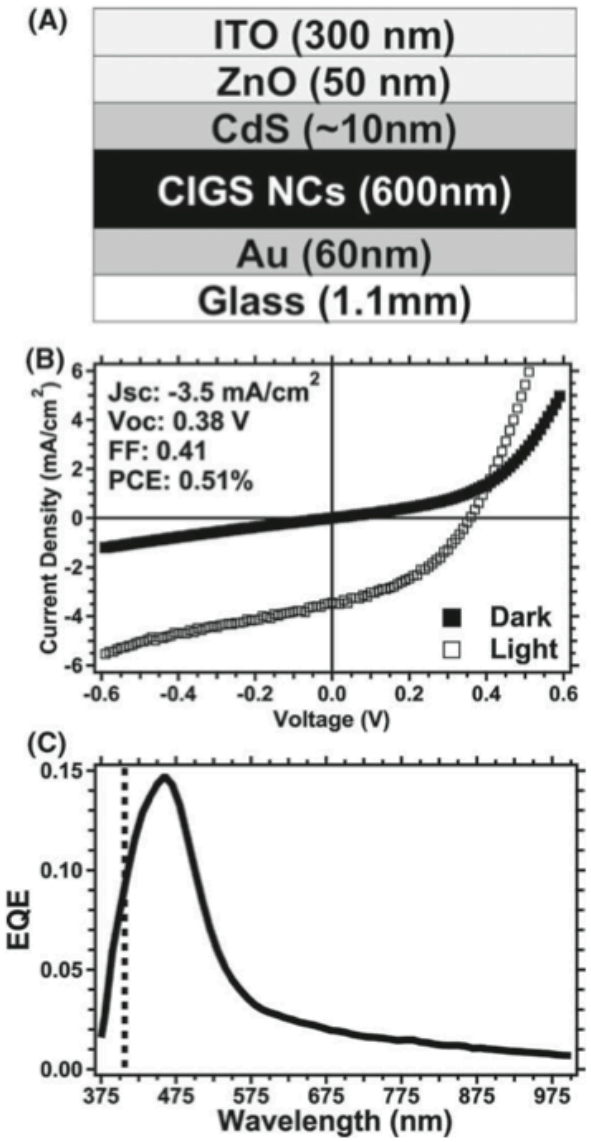

Figure 3.1. A) Schematic of a CIGS nanocrystal (NC) based PV device.B) *J–V* measurements performed under dark and AM1.5 illuminationconditions. C) External Quantum Efficiency (EQE) measured as afunction of wavelength (vertical dotted line marks the laser excitationwavelength used for LBIC, 408 nm).

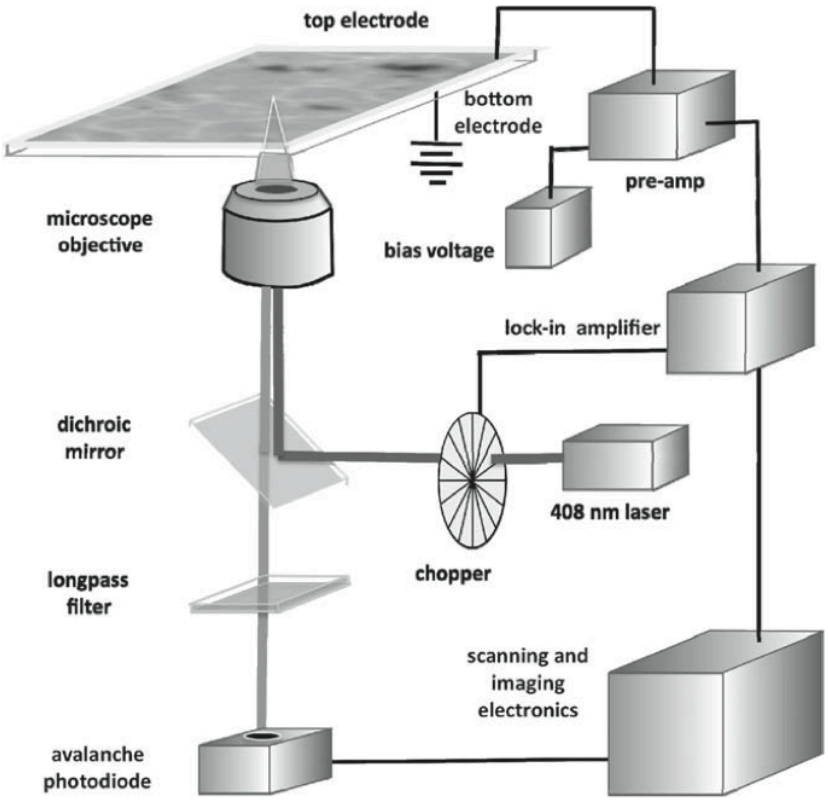

Figure 3.2. Schematic of the scanning light beam induced current (LBIC) and fluorescence microscopy experimental setup.

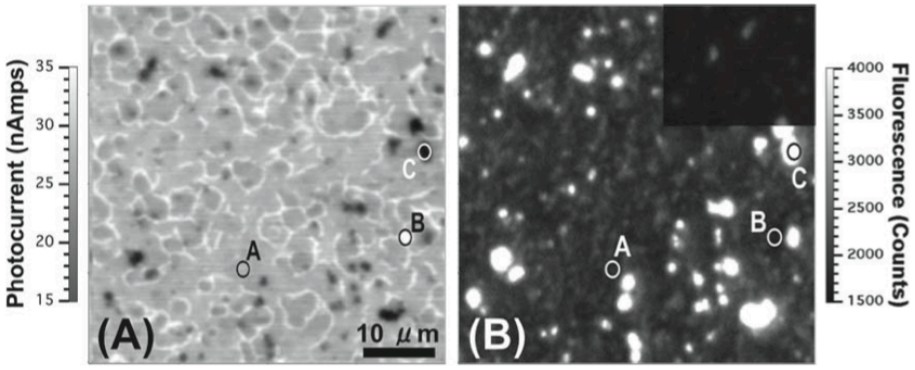

Figure 3.3: Image maps of A) zero-bias induced photocurrent (IPC) and B) fluorescence intensity for a CdS-capped CIGS nanocrystal PV device. Overlay in upper right corner of (B): that area of the fluorescence image shown at a different, nonsaturated contrast scale of 1500 to 27 000 counts.

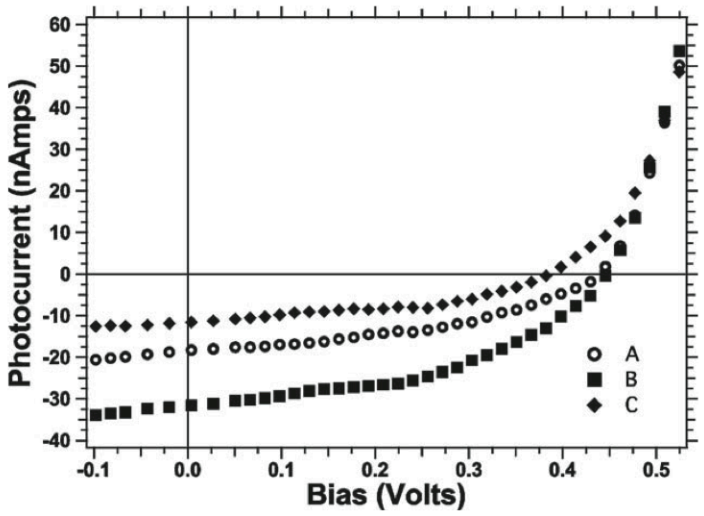

Figure 3.4: Local voltage-dependent photocurrent (LVPC) measured with the focused light beam positioned at locations A, B, and C labeled on the images shown in Figure 3. These LVPC measurements are representative of the response from regions of the device with average, high and low IPC.

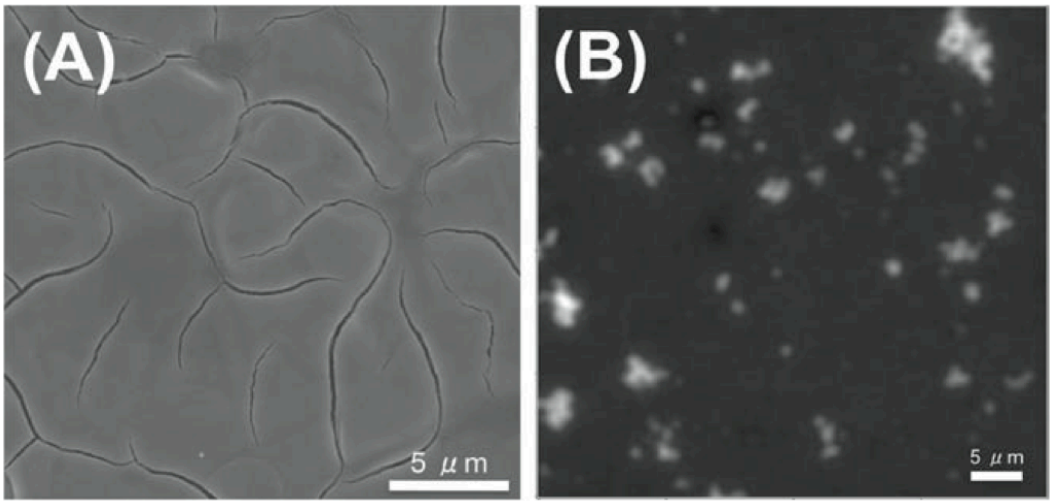

Figure 3.5: A) Scanning electron microscope image of the CIGS nanocrystal layer of the device. B) Fluorescence image of a CdS layer deposited on glass, intensity scale is 10000 to 50000 counts.

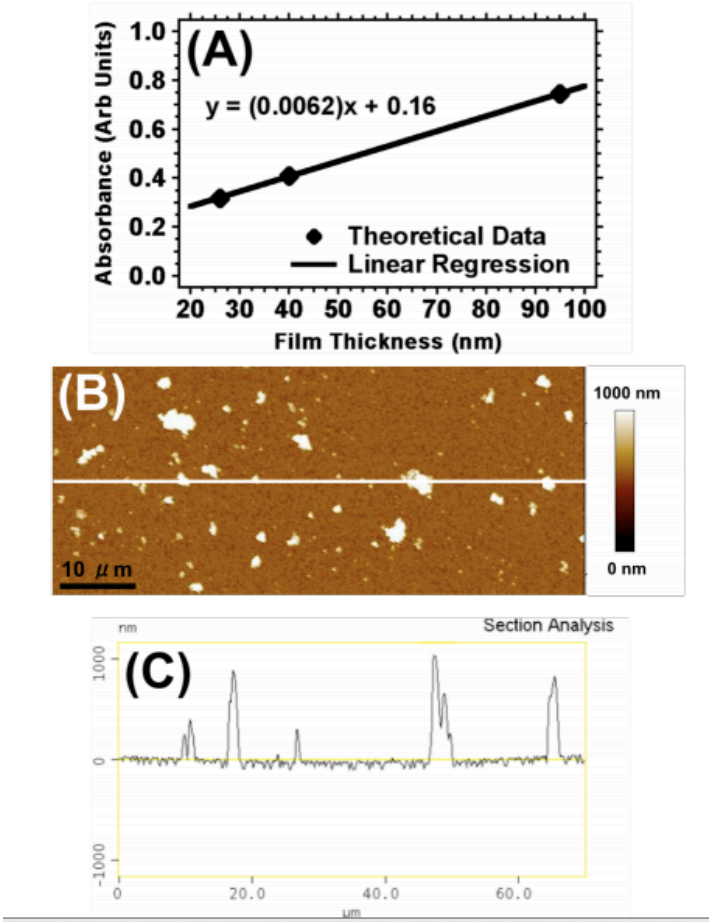

Figure 3.6: (A) Beer's Law plot of CdS absorbance at 408 nm wavelength light, constructed from theoretically calculated data from Derkaoui and co-workers.[36] (B) Topographic AFM image of CdS layer deposited on a glass substrate. (C) Line scan (section analysis) of the AFM topography taken along the white line in (B).

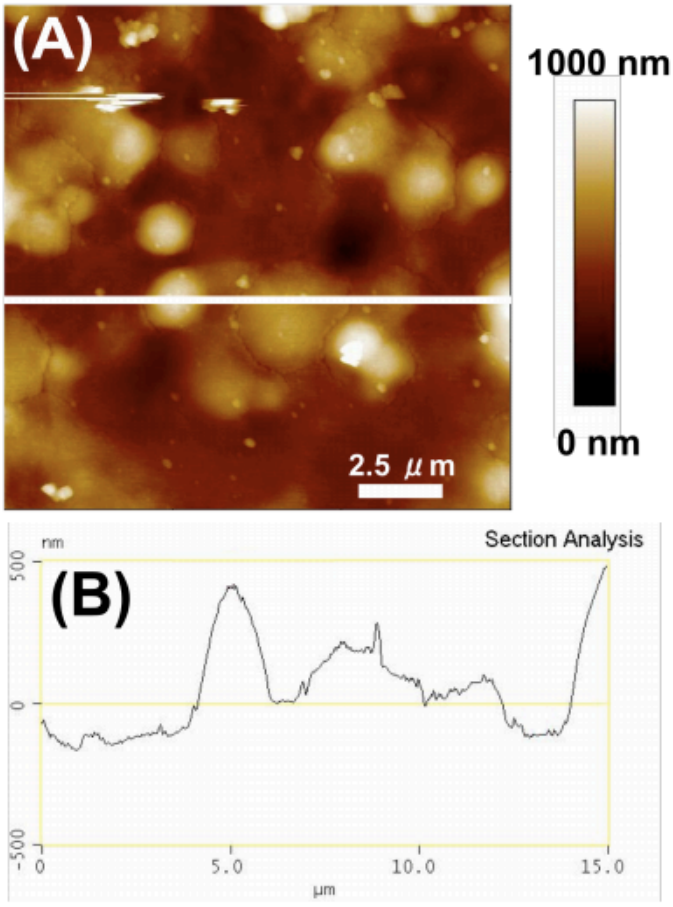

Figure 3.7: (A) Topographic AFM image of CdS layer on the CIGS nanocrystal film. (B) Line scan (section analysis) of the AFM topography taken along the white line in image (A).

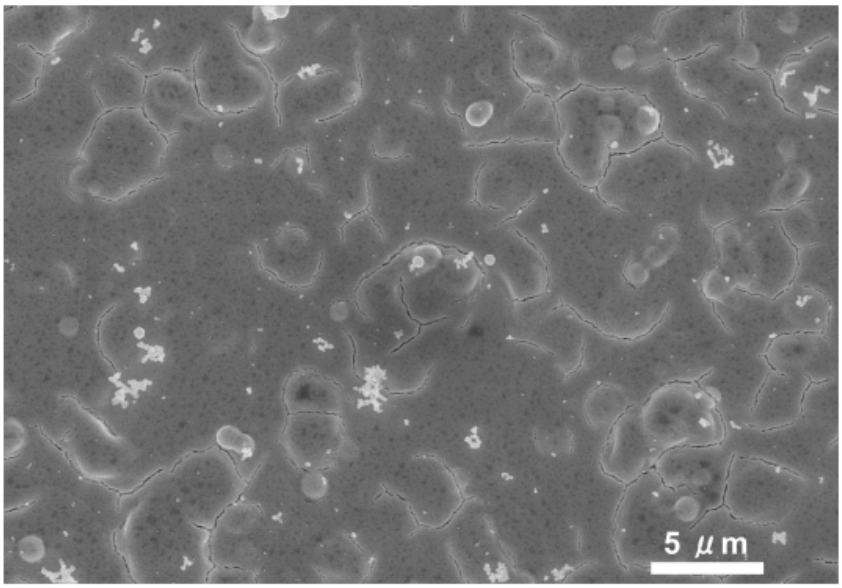

Figure 3.8: Scanning electron micrographs image of the CIGS nanocrystal layer of the device capped with the CdS layer.

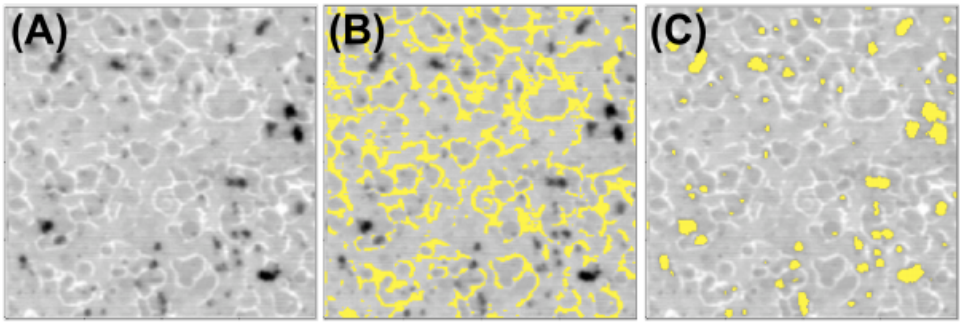

Figure 3.9: Image map of (A) zero-bias induced photocurrent (IPC) from Figure 3, and images with a threshold set to highlight areas of (B) high photocurrent and (C) low photocurrent.

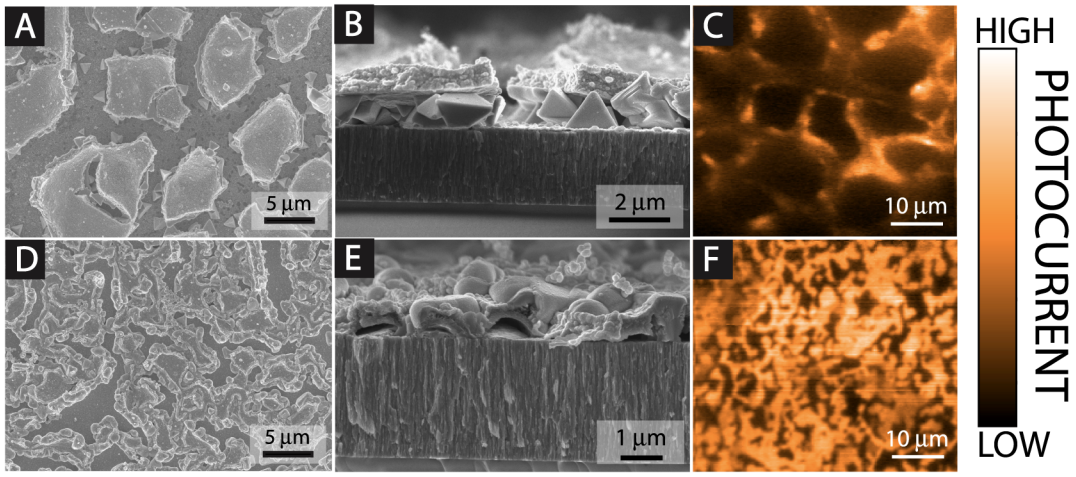

Figure 3.10: SEM images (top view A and D, cross sectional view B and E) and LBIC (C and F) maps of two different devices with selenized layers: A–C are of a $CuInSe_2$ device and C–F are of the highest efficiency CIGS device from Table 1 with actual compositions of $Cu_{0.65}InSe_2$ and $Cu_{0.82}In_{0.68}Ga_{0.32}Se_2$, respectively. The high photocurrent regions of the absorber layer had approximately 5x the output density of the low photocurrent regions.

1. J.-L. Bredas, J. R. Durrant, *Accounts of Chemical Research* 2009, *42*, 1689–1690.

2. A. Goetzberger, C. Hebling, H. W. Schock, *Materials Science and Engineering R* 2003, *40*, 1–46

3. X. Yang, J. Loos, *Macromolecules* 2007, *40*, 1353–1362.

4. F. C. Krebs, *Sol. Energ. Mater. Sol. C*. 2009, *93*, 394–412.

5. C. J. Brabec, *Solar Energy Materials Solar C*. 2004, *83*, 273–292.

6. B. R. Saunders, M. L. Turner, *Adv. Colloid Interfaces* 2008, *138*, 1–23.

7. H. Spanggaard, F. C. Krebs, *Solar Energy Materials and Solution C*. 2004, *83*, 125–146.

8. C. R. McNeill, B. Watts, L. Thomsen, W. J. Belcher, A. L. D. Kilcoyne, N. C. Greenham, P. C. Dastoor, *Small* 2006, *2*, 1432–1435.

9. L. S. C. Pingree, O. G. Reid, D. S. Ginger, *Advanced Materials* 2009, *21*, 19–28.

10. P. V. Kamat, *Journal of Physical Chemistry C* 2008, *112*, 18737–18753.

11. D. C. Olson, S. E. Shaheen, R. T. Collins, D. S. Ginley, *Journal of Physical Chemistry C* 2007, *111*, 16670–16678.

12. A. Cadby, G. Khalil, A. M. Fox, D. G. Lidzey, *Journal of Applied Physics* 2008, *103*, 093715.

13. L. J. Rozanski, C. W. Cone, D. P. Ostrowski, D. A. Vanden Bout, *Macromolecules* 2007, *40*, 4524–4529.

14. E. S. Kwak, T. J. Kang, D. A. Vanden Bout, *Analytical Chemistry* 2001, *73*, 3257–3262.

15. J. Teetsov, D. A. Vanden Bout, *Langmuir* 2002, *18*, 897–903.

16. Y. Q. Gao, J. K. Grey, *Journal of the American Chemical Society* 2009, *131*, 9654–9662.

17. D. C. Coffey, D. S. Ginger, *Nature Materials* 2006, *5*, 735–740.

18. D. C. Coffey, O. G. Reid, D. B. Rodovsky, G. P. Bartholomew, D. S. Ginger, *Nano Letters* 2007, *7*, 738–744.

19. V. Palermo, M. B. J. Otten, A. Liscio, E. Schwartz, P. A. J. de Witte, M.A.Castriciano,M.M.Wienk,F.Nolde,G.DeLuca,J.J.L.M.Cornelissen, R. A. J. Janssen, K. Müllen, A. E. Rowan, R. J. M. Nolte, P. Samorì, *Journal of the American Chemical Society* 2008, *130*, 14605–14614.

20. H. Hoppe, T. Glatzel, M. Niggemann, A. Hinsch, M. C. Lux-Steiner, N. S. Sariciftci, *Nano Letters* 2005, *5*, 269–274.

21. O. Douhéret, A. Swinnen, S. Bertho, I. Haeldermans, J. D'Haen, M. D'Olieslaeger, D. Vanderzande, J. V. Manca, *Progress Photovoltaics* 2007, *15*, 713–726.

22. V. Palermo, M. Palma, P. Samori, *Advanced Materials* 2006, *18*, 145–164.

23. L. S. C. Pingree, O. G. Reid, D. S. Ginger, *Nano Letters* 2009, *9*, 2946–2952.

24. T. A. Bull, L. S. C. Pingree, S. A. Jenekhe, D. S. Ginger, C. K. Luscombe, *ACS Nano* 2009, *3*, 627–636.

25. M. J. Romero, A. J. Morfa, T. H. Reilly, J. van de Lagemaat, M. Al-Jassim, *Nano Letters* 2009, *9*, 3904–3908.

26. K. Durose, S. E. Asher, W. Jaegermann, D. Levi, B. E. McCandless, W. Metzger, H. Moutinho, P. D. Paulson, C. L. Perkins, J. R. Sites, G. Teeter, M. Terheggen, *Progress in Photovoltaics* 2004, *12*, 177–217.

27. M. Acciarri, S. Binetti, A. Racz, S. Pizzini, G. Agostinelli, *Solar Energy Materials and Solution C*. 2002, *72*, 417–424.

28. C. R. McNeill, H. Frohne, J. L. Holdsworth, P. C. Dastoor, *Synthesis Methods* 2004, *147*, 101–104.

29. C. R. McNeill, H. Frohne, J. L. Holdsworth, P. C. Dastoor, *Nano Letters* 2004, *4*, 2503–2507.

30. C. R. McNeill, H. Frohne, J. L. Holdsworth, J. E. Furst, B. V. King, P. C. Dastoor, *Nano Lettes* 2004, *4*, 219–223.

31. Y. Q. Gao, T. P. Martin, A. K. Thomas, J. K. Grey, *Journal of Physical Chemical*

Letters 2010, *1*, 178–182.

32. N. M. Thantsha, E. Q. B. Macabebe, F. J. Vorster, E. E. van Dyk, *Phys. B-Condensed Matter* 2009, *404*, 4445–4448.

33. R. Riehn, R. Stevenson, D. Richards, D.-J. Kang, M. Blamire, A. Downes, F. Cacialli, *Advanced Functional Materials* 2006, *16*, 469–476.

34. M. G. Panthani, V. Akhavan, B. Goodfellow, J. P. Schmidtke, L. Dunn, A. Dodabalapur, P. F. Barbara, B. A. Korgel, *Journal of the American Chemical Society* 2008, *130*, 16770–16777.

35. I. Repins, M. A. Contreras, B. Egaas, C. DeHart, J. Scharf, C. L. Perkins, B. To, R. Noufi, *Progress in Photovoltaics* 2008, *16*, 235–239.

36. Z. Derkaoui, Z. Kebbab, R. Miloua, N. Benramdane, *Solid State Communununications* 2009, *149*, 1231–1235.

37. B. E. McCandless, W. N. Shafarman, Chemical Surface Deposition of Ultra-thin Semiconductors, *U.S. Patent 6,537,845*, March 25, 2003.

38. V.A. Akhavan, M.G. Panthani, B.W. Goodfellow, D.K. Reid, B.A. Korgel, *Energy Express* **2010,** 18, A411–A420.

39. Q. Guo, G.M. Ford, H.W. Hillhouse, R. Agrawal, *Nano Lett.* **2009**, 9, 3060–3065.

40. Q. Guo, G. M. Ford, R. Agrawal, H. W. Hillhouse, Prog. Photovoltaics: Research and Applications **2012**, doi: 10.1002/pip.2200.

Chapter 4: A macromolecular scaffold for supramolecular self-assembly of molecular aggregates

Introduction

Small molecule organic materials have the potential for applications in variety of electronic devices like organic field effect transistors (OFET)[1], and organic photovoltaics (OPV)[2]. Because the properties of the materials can vary greatly depending on the details of their molecular packing, one would like to develop schemes by which supramolecular assemblies could be self-assembled from solution.[3] Perylene-bis(dicarboximide) [PDI] has been extensively studied as an electron acceptor due to both its electronic structure and its high chemical stability.[4] Studies on PDI include examining the mateiral in solution,[5] thin films,[6] crystals and aggregates,[7] as well as liquid crystalline systems.[8] In the condensed phase, the PDI molecule can easily stack cofacially leading to electornic coupling of the dye molecules and new aggregated electronic states. PDI aggregation has shown that it conforms to different architectures, including the predominant face-to-face geometry that leads to a H-type aggregate.[9] Recent works has also demonstrated that by inducing a slight offset in the molecule packing J-type aggregates can be formed.[10] The typical stacking geometry of PDI leads to an H-type aggregate in which the emission yield is strongly suppressed. In particular, weakly coupled H-aggregates exhibit a characteristic change in the ratio of the vibronic peaks in their absorption spectrum with

the aggregates leading to a suppression in the lowest energy, 0-0, vibrational band. While the aggregates can greatly affect both the electronic and optical properties of the PDI, it is difficult to control the extent of aggregation. This is particularly true for molecules such as PDI that are extremely insoluble. Generally to increase solubility, bulky alkly chains are added to the PDI, but this can alter the aggregation of the molecule. Schwartz et. al. have shown that an excellent method for both improving solution processing and controlling the PDI aggregation is to attach PDI to a polymer backbone.[11] In their work, they show that the perylene appended to a peptide will aggregate in a good solvent compared to the monomer, and forms films that display a high density of charge carriers. This work utitlizes solvent quality and the weakly coupled H-aggregate model to systematically study the change in aggregation as a quantified using the weakly-coupled H-aggregate model.

Experimental

Figure 1 illustrates the synthetic steps starting with commercially available norbornadiene. The diene is mixed with glacial acetic acid and heated, in a closed vessel, to yield the exo-5-norbornene-2-yl acetate intermediate, 1. The hydrolysis of the acetate group using base in methanol yields the exo-5-norbornene-2-ol 2. The deprotonation of this material allows its use as a powerful nucleophile for substitution type reactions. In this case, after deprotonation, the anion is exposed to 6-chloro-1-hexyl ptoluenesulfonate. The resulting substitution reaction yields an alkyl halide norbornene monomer (3). The Gabriel amine synthesis is then utilized to result in, 6-amino-1-(exo-5-norbornene-2-oxy)hexane (4). When beginning with 3,4,9,10-Perylenetetracarboxylic

acid dianhydride, the addition of alkyl groups to provide solubility is a required first step (Scheme 2). Through a reaction in molten imidazole, with a simple secondary amine, the N,N'-Bis(1-nonyloctyl)-perylene-3,4,9,10-tetracarboxylic diimide (5) is obtained and easily purified. Then through hydrolysis of one end of the molecule, it is possible to obtain N-(1-nonyloctyl)perylene-3,4,9,10-tetracarboxy-3,4-anhydride-9-10-imide (6). Finally, 3 is condensed with 6 through a short reflux in toluene resulting in the final PDI containing monomer (7). Polymerization of 7 using 1st generation Grubbs' catalyst in CHCl3 resulted in a ring-opened metathesis polymer (Poly-PDI).

All polymer and monomer samples were diluted to have a maximum absorption less than 0.05. All absorption spectra were obtained using an Agilent 8453 UV-VIS. Fluorescence was measured using a Fluorolog-3 lifetime fluorimeter purchased from Horiba Jobin-Yvon. Samples were excited with a 450W Xenon Lamp and fluorescence was collected using right angle geometry, a double monochromator, and a thermoelectrically cooled InGaAs detector. All lifetime data was collected on the same fluorimeter. The samples were excited using a NanoLED with excitation at 482 nm and a pulse width of less than 200 ps. The data was fit to one or two exponentials using DAS6 v2.6 fitting software. Films were made using a concentration of 15 mg/mL of PPDI in hexane, toluene or ortho-dichlorobenzene (ODCB) and spin cast at 1000rpm for 60 seconds. Fluorescence Correlation Spectroscopy (FCS) measurements were done on a confocal microscope using an extended beam of the collimated 488 nm line of an Ar+ gas laser to a diameter of about 1 cm and coupled into the objective. The fluorescence signal

was focused on two avalanche photo diodes (SPCM-AQR-16, Perkin-Elmer) for detection and the signal was correlated by an ALV-5000 fast hardware correlation card.

Results and Discussion

The monomer used for all experiments is N,N'-Bis(1-nonyloctyl)-perylene-3,4,9,10-tetracarboxylic diimide (PDI) shown in **5** of figure 1 and the polymer PDI (P-PDI) is shown in the last step. Figure 2 shows both the absorption spectra of PDI monomer as well as the polymer in a variety of solvents of different quality. Figure 2A is of the monomer in o-dichlorobenzene (ODCB). The monomer spectrum exhibits a clear vibronic structure, with the largest absorbance coming from the lowest energy, 0-0, vibrational peak at 530nm. The spacing between the vibronic peaks is roughly 1400 cm^{-1} corresponding to a typical C=C stretching mode in the PDI. The polymer spectrum is acquired in three different solvents of varying quality. Figure 2B is P-PDI in hexane, which is the worst solvent (lowest solubility) for the polymer. Figure 2C and 2D show the polymer spectrum in ODCB and toluene. ODCB is a moderate solvent, and toluene is a good solvent. The spectrum of P-PDI in hexane is almost identical to the monomer absorption in its spectral shape, however the peak absorption wavelength is shifted as a result of the solvent polarity. In contrast, the P-PDI spectrum in ODCB (Figure 2C) shows similar vibronic progression, but the ratios of the peak intensities are significantly different. In particular, the intensity of the lowest energy 0-0 transition appears suppressed compared with the monomer and hexane spectra. Similar results are observed for toluene (Figure 2D), but the suppression and broadening is even greater with the 0-0 peak becoming smaller in intensity than the 0-1 peak.

This suppression of the 0-0 band in the spectrum of the polymer in the good solvents is attributed to the formation of H-type aggregates of the PDI molecules along the polymer backbone. While formation of H-aggregates is typically associated with a blue shift of the spectrum, it has been shown that a signature of the formation of weakly coupled H-aggregates is the suppression of the 0-0 band in the absorption with little or no shift in origin of the band. Molecular aggregation is typically associated with lower solvent quality in which the molecules have a preferential interaction with themselves compared to the solvent. However, here the aggregates form in the high quality solvents. As the aggregates are formed along the backbone of the polymer, this process is strongly dependent on the conformation of the polymer backbone. In a good solvent the polymer should have few interchain interactions and adopt an extended conformation with a large radius of gyration. However, in a bad solvent, the polymer will collapse on itself leading to a more random arrangement of the pendant PDI molecules. This random architecture prevents strong interactions of the PDI molecules, and therefore the spectrum is nearly the same as that of the monomer.

Additionally, to verify that the aggregation was intramolecular versus intermolecular the concentration dependence of the aggregate was probed. If multiple polymer chains were aggregating in solution, strong concentration dependence would be expected. However, in all cases the concentration dependence was observed as would be expected for intramolecular aggregation (See figure 7). Additionally, fluorescence correlation spectroscopy (figure 9) measurements were performed in the different solvent conditions to quantify the concentration of the polymers, and the number density of the

fluorescent species was found to be identical in all the solvent conditions indicating that the aggregation is occuring along the polymer backbone.

To quantify the extent of aggregation in each solvent, we analyzed the ratio of the vibronic peaks in the context of the weakly coupled H-aggregate model. First, we fit the monomer spectrum to a Frank-Condon progression to verify that the spectrum was well represented by a single vibronic progression. Figure 3A displays the experimental absorption (black line), individual Lorentzian peak fits (red line), and total fit (black dashed) for the monomer in ODCB. The peaks were fit to 4 loretzians with peak spacing of 1384 cm^{-1}. The first peak is centered at 18900 cm^{-1} and the second peak is centered at 20284 cm^{-1}. The ratio of the peak areas of the 0-0 peak to the 0-1 was found to be 0.74, which is the displacement or Huang-Rhys factor (λ).[12] To characterize the extent of aggregation, the absorption spectra of the P-PDI in each solvent was also fit to a series of loretzians. Figure 3b displays the corrected spectra of P-PDI in hexane (blue), ODCB (green), and toluene (red), where all data was normalized to the 0-1 peak to emphasize the suppression of the 0-0 peak with increase in solvent quality. The peak spacing was held the same for each sample, however the origin of the peaks were changed. The exciton bandwidths were calculated using the work from Frank Spano et al. and modified using the calculated Huang Rhys factor of the monomer.[13] The modified expression is shown below:

$$\frac{A_{0-0}}{A_{0-1}} = \frac{(1-1.26W)^2}{0.74(1+0.95W)^2} \qquad (1)$$

where W is the exiton bandwidth and $A_{0\text{-}0}$ and $A_{0\text{-}1}$ are the corresponding absorption areas of the PDI. As discussed above, the spectrum of P-PDI in hexane appears to resemble the monomer, in which a strict fitting yields an exciton bandwidth of 0.21 meV, which is essentially zero. However, we observe an increasingly higher degree of aggregation in ODCB (110 meV) and toluene (138 meV). These bandwidths are on the same order of magnitude as the peak spacings (171 meV), as seen in the exciton bandwidth.

The exciton bandwidth calculation from the absorbance assumes that aggregation is homogeneous, meaning all the PDI is equally aggregated along the polymer backbone and have a similar vibronic progression. Fluorescence spectroscopy was used to investigate this assumption since a combination of emission spectra and lifetimes allow identification of multiple emitting states. Figure 4a shows the fluorescence spectrum of the monomer, which displays the expected mirror image of the vibronic peaks in the absorption spectrum. The lifetimes, figure 4b, for all 3 peaks are found to be single exponential with a decay constant of 4 ns, which is in good agreement with the literature.[14] The spectrum of the P-PDI in hexane, figure 4c, looks similar to the monomer spectrum, in which the fluorescence is a mirror image of the absorption. Again, the lifetime, figure 4d, is single exponential with a decay constant (4 ns) for all 3 peaks, corresponding to a single emissive state. The polymer in ODCB and toluene are quite different from the monomer and hexane. In ODCB and toluene the emission spectrum is no longer the simple mirror image of the absorption spectrum but now contains the addition of a very broad red shifted peak. In contrast to the hexane and monomer spectra, the lifetime now exhibits wavelength dependence. In Figure 4F, H) the first peak has a

lifetime of 4 ns, which we attribute to PDI that remains unaggregated along the polymer backbone. The decay of the broad red shifted peak is also single exponential but with a much longer lifetime of 25 ns. This long lifetime and broad featureless red-shifted emission is attributed to an excimer state. In an aggregated system, it is common to observe excimer-like emission. The decay at wavelengths in the middle of the spectrum is bi-exponential combination of the 4 ns and 25 ns decays. Therefore, at these wavelengths the decay is a superposition of the monomer and excimer decays. This indicates that overall, the polymer is not homogeneously aggregated, and appears to have two emissive states arising from unaggregated and aggregated PDI pendants.

To quantify the amount of unaggregated PDI along the polymer, the excitation spectra of the polymer was compared with the total absorption. Excitation and emission spectra were taken at all excitation and emission wavelengths to produce a 3D spectrum. Figure 5A shows the 3D plot of P-PDI in hexane, with lines delineating the peak wavelengths used for individual excitation spectra displayed in Figure 5B. The normalized excitation spectra at each of these peaks reveal identical spectra to the absorbance of P-PDI in hexane as would be expected for a single species. Figure 5C and 4E are 3D plots of the P-PDI in ODCB and toluene, which shows the progression from unaggregated to aggregated PDI at longer emission wavelengths. Figures 5D (ODCB) and 4F (Toluene) show representative excitation spectra collected at 525, 680 and 625 nm. The 525 nm peak is an unaggregated peak and the 680 nm peak is the aggregate, while the 625 nm peak is a mixture of the two spectra. The representative aggregate excitation spectrum at 680 nm was selected because it is where the 0-0 peak is at a

minimum. By overlaying the 525 nm excitation spectra and the absorption spectra we calculated the percent of monomer present and contributing to the absorption. The absorption and aggregation excitation spectra are nearly identical to the dye along the polymer backbone and are mostly in an aggregate form. Therefore, only a small fraction (5%) of PDI in both ODCB and toluene is unaggregated and is likely due to defects in the polymer or pendants hanging off the ends of the polymer.

In order to calculate a relative quantum yield as a function of aggregation, the known monomer spectrum was subtracted from the aggregate spectrum (See figure 9). This yielded a fluorescence spectrum of only the aggregated PDI. Comparing the total emission from the aggregate compared to the monomer, we found P-PDI in DCB had a relative quantum yield of 46%, while the P-PDI in toluene had a relative quantum yield of 34%.

Lastly, films were made to determine if the extent of aggregation could be retained for solid-state devices. When spin cast or dropcast from any of the three solvents above, the same extent of aggregation is observed for all samples. Figure 6A displays the absorption (solid) and fluorescence (dotted) of a representative film spincast from toluene compared to the solution phase absorption and fluorescence (blue). Therefore, the aggregate in toluene is nearly identical to that found in films. However, there are some key differences. The emission in films is red shifted and shows no monomer. This is likely due to more efficient energy transfer to low energy sites in the film. This is confirmed by the fast, multiexponential lifetime shown in Figure 6B, which is consistent with previous work.[15]

Conclusions

We have shown a novel polymer with highly ordered pendant molecules. This work details how aggregation can be measured and used as a system to explore an important class of polymers, where supramolecular self-assembly can be controlled in solution. We have shown the extent of aggregation in different solvents and related that to an exciton bandwidth using the weakly coupled H-aggregate model. Furthermore, we have determined we had an H-aggregate based on our fluorescence and lifetime data, and quantified the amount of monomer and aggregate along the polymer backbone, where we have shown there to be very little monomer (less than 5%). Finally, we made films to show we can retain the extent of aggregation for the use in solid-state devices, such as OFETs and photovoltaics. We have also determined an excellent model for observing the photophysics of a film in solution, which simplifies the 3-D framework of films and allows for easier quantification of aggregation. Future work will include introducing different donor and acceptor blocks in the polymer backbone in order to observe energy transfer in this model system.

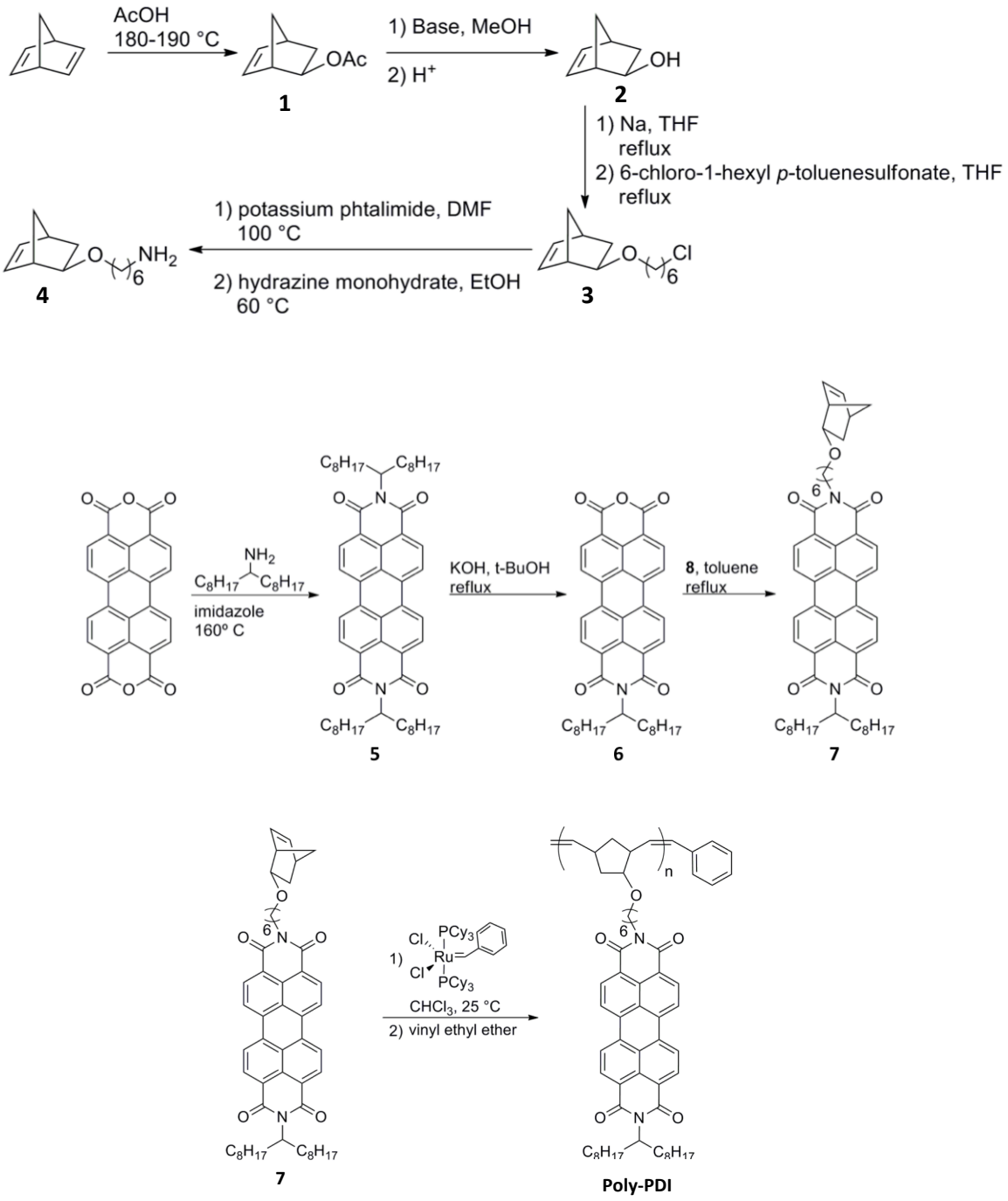

Figure 4.1: Synthesis of the norbornene polymer and Poly-PDI.

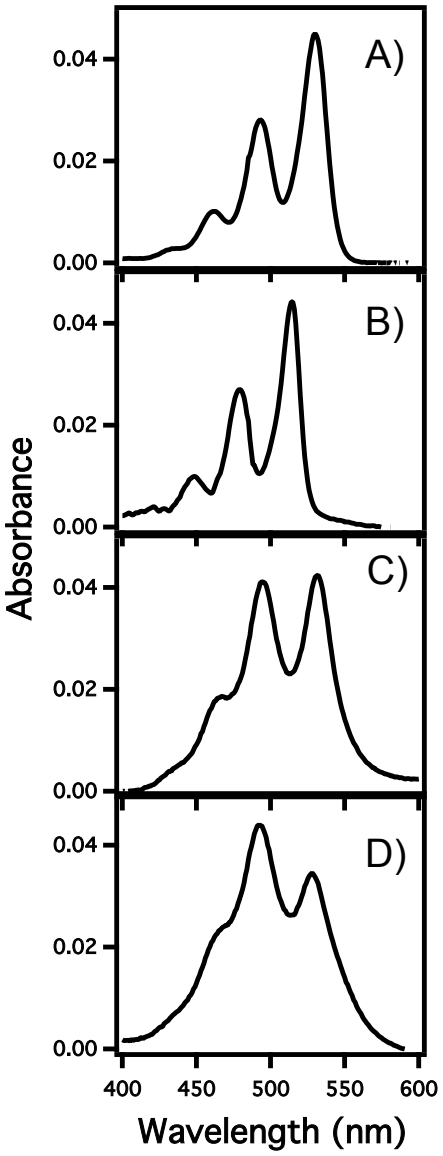

Figure 4.2: Absorption spectra of A) the PDI monomer and PDI Polymer (PPDI) in B) hexane, C) o-dichlorobenzene, and D) in toluene. The 0-0 peak decreases as the polymer becomes better solvated. PPDI is poorly solvated in hexane, while it is highly solvated in toluene.

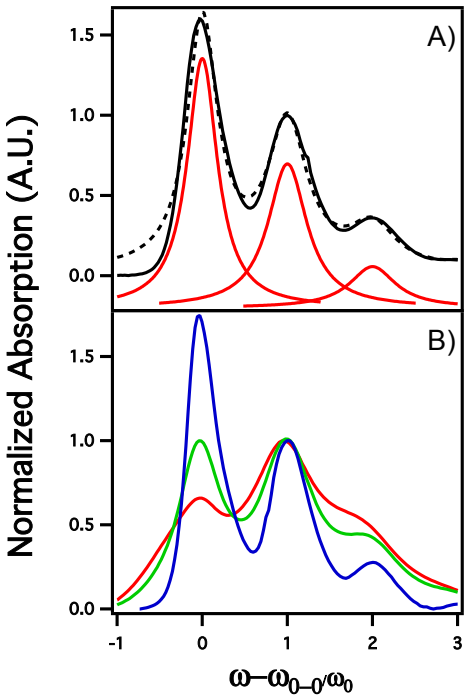

Figure 4.3: (A) Absorption spectra of the monomer PDI in ODCB (Black), the fit (dotted) and the individual peaks (red). B) PDI polymer, where blue is PPDI in hexane, green in ODCB, and red in toluene. The spectra is corrected, in which the 0-0 vibrational peak is at 0, 0-1 peak is at 1, and 0-2 peak is at 2.

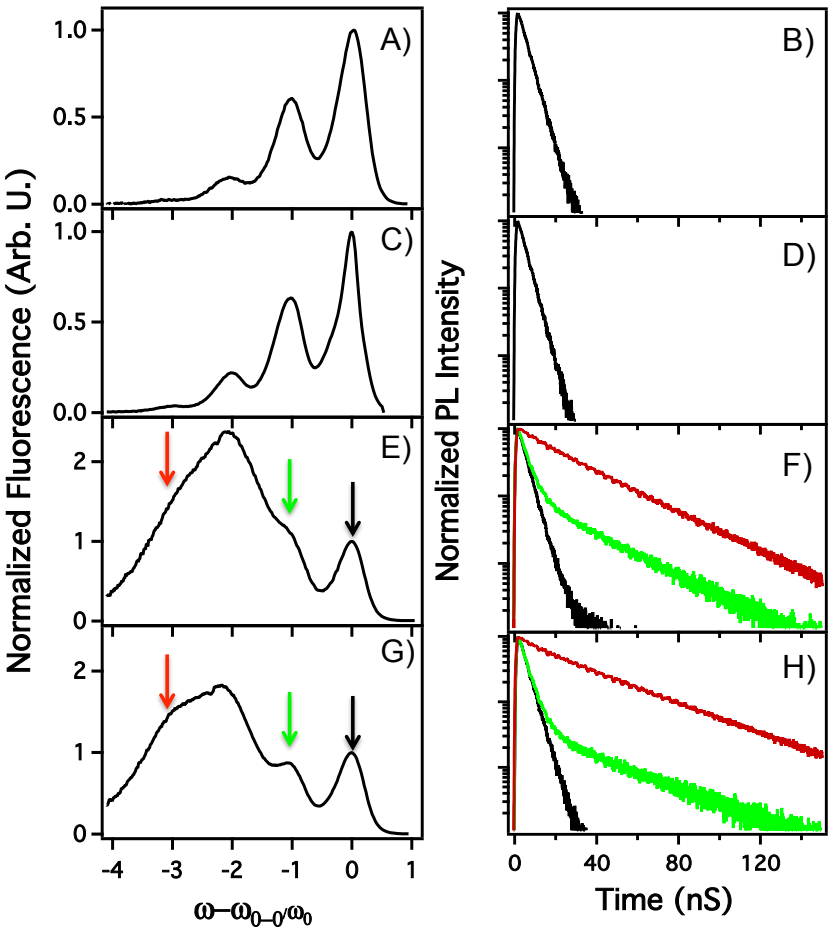

Figure 4.4: Fluorescence spectra of A),C), E) and G) and lifetime spectra B)-H). A) and E) are of the monomer PDI, B) and F) is of the P-PDI in hexane, C) and G) in O-DCB, and D) and H) in toluene. The large featureless low energy peak is of the excimer formed when PDI aggregates. The arrows are color coded to show the poinst at which the lifetimes were taken. For the monomer PDI and P-PDI in hexane, there was only one 4ns lifetime at each of the peaks, while the P-PDI in O-DCB show two lifetimes, 4ns and 25ns. The 4ns peak is the monomer like PDI, while the 25ns is the excimer from the aggregate.

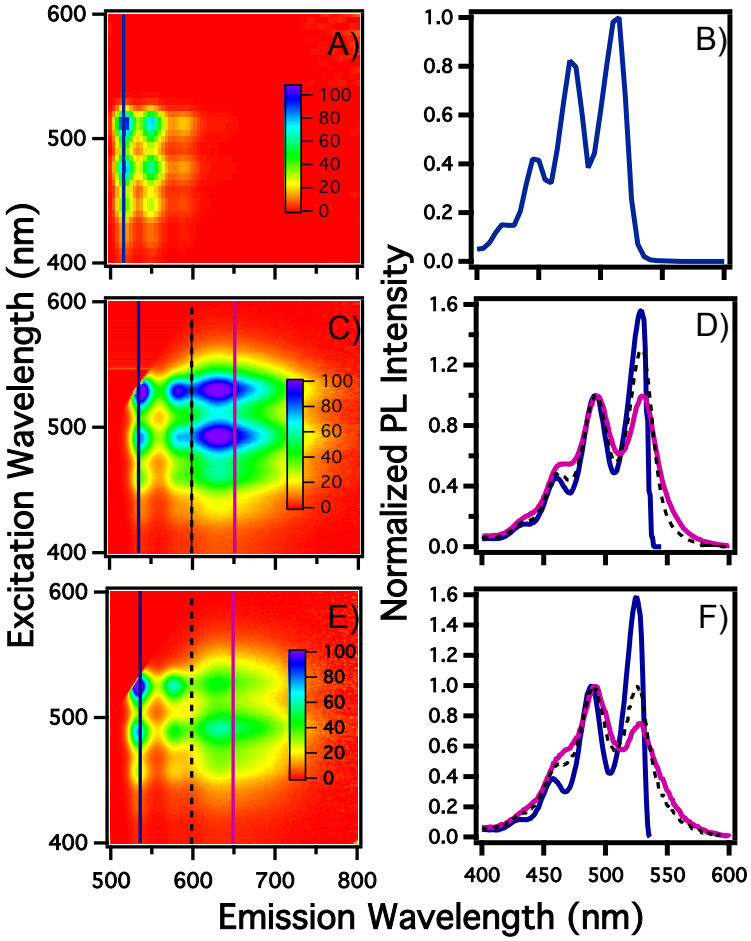

Figure 4.5: 3D spectra of PPDI in a) Hexane, b) ODCB, and c) Toluene. The left axis is excitation, the bottom axis is emission and the intensities are shown with red being 0, and purple as the highest relative intensity. The scale bar is one thousand counts per second. Line scans of the 3D spectra are shown on the right, where D), E) and F) are in hexane, ODCB, and toluene respectively. In hexane, the excitation spectra is the same at all wavelengths. In E) and F), two different excitation spectra are shown. Pink is measured at an emission of 525nm, and blue is measured at 625nm.

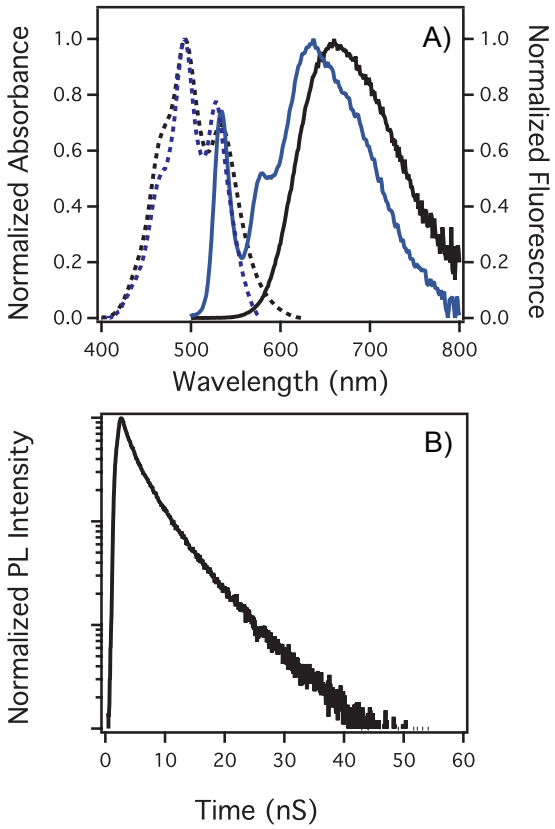

Figure 4.6: A) Absorbance (dotted black) and fluorescence spectra of P-PDI film (black) and absorbance (dotted blue) and fluorescence spectra P-PDI in Toluene (blue). B) Lifetime of films taken at 650nm. The lifetimes are multiexponential.

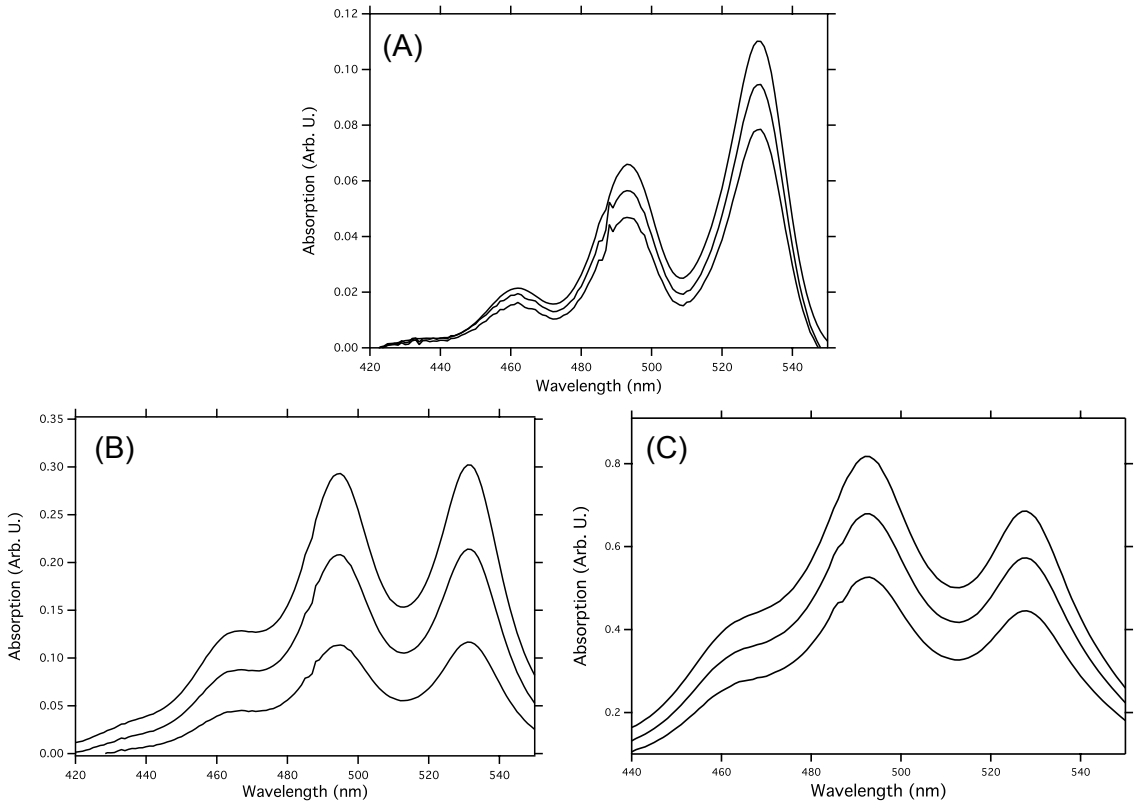

Figure 4.7: Concentration dependence on the absorption for PPDI in hexane (A), ODCB (B) and toluene (C). The higheset absorption is an order of magnitude higher concetration, but was corrected to be on the same scale. All absorptions were linear with concentration.

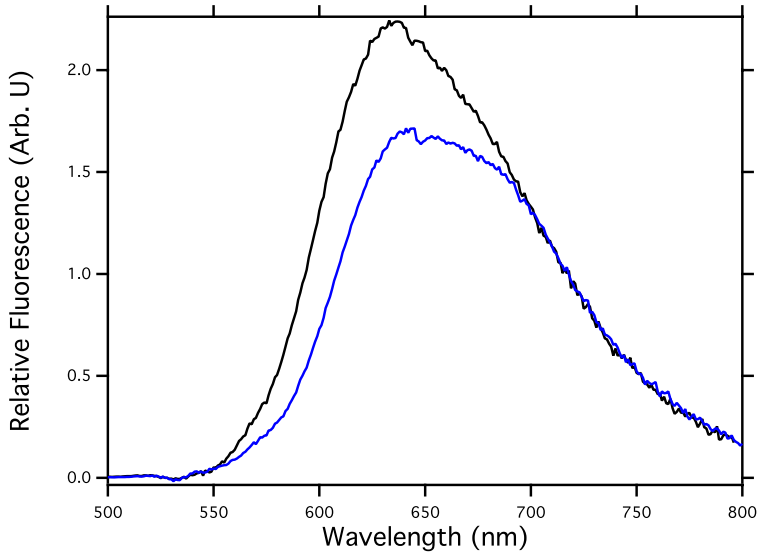

Figure 4.8: Corrected fluorescence. The monomer emission spectrum was subtracted from the polymer spectrum in ODCB (Black) and toluene (Blue), to reveal the excimer. The spectra are normalized relative to eachother to show the change in emission.

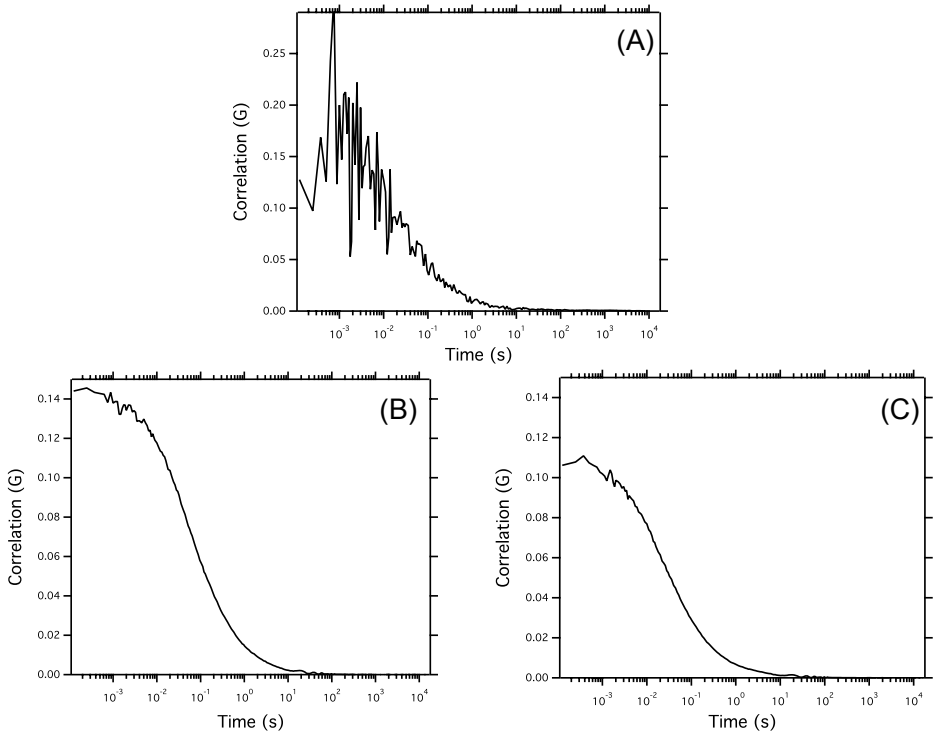

Figure 4.9: Fluorescence coorelation spectroscopy of PPDI in A) hexane, B) ODCB, and C) toluene. Within error, the data shows no polymer-polymer aggregation.

1. Tour, J. M. *Accounts of Chemical Research* **2000,** 33, (11), 791-804.

2. Chesterfield, R. J.; McKeen, J. C.; Newman, C. R.; Ewbank, P. C.; da Silva Filho, D. A.; Brédas, J.-L.; Miller, L. L.; Mann, K. R.; Frisbie, C. D. *The Journal of Physical Chemistry B* **2004,** 108, (50), 19281-19292.

3. Riede, M.; Mueller, T.; Tress, W.; Schueppel, R.; Leo, K. *Nanotechnology* **2008,** 19, (42), 424001.

4. Rajaram, S.; Armstrong, P. B.; Kim, B. J.; Fréchet, J. M. J. *Chemistry of Materials* **2009,** 21, (9), 1775-1777.

5. Hutchison, G. R.; Ratner, M. A.; Marks, T. J. *Journal of the American Chemical Society* **2005,** 127, (48), 16866-16881.

6. Kline, R. J.; DeLongchamp, D. M.; Fischer, D. A.; Lin, E. K.; Richter, L. J.; Chabinyc, M. L.; Toney, M. F.; Heeney, M.; McCulloch, I. *Macromolecules* **2007,** 40, (22), 7960-7965.

7. Shin, W. S.; Jeong, H.-H.; Kim, M.-K.; Jin, S.-H.; Kim, M.-R.; Lee, J.-K.; Lee, J. W.; Gal, Y.-S. *Journal of Materials Chemistry* **2006,** 16, (4), 384-390.

8. Balakrishnan, K.; Datar, A.; Naddo, T.; Huang, J.; Oitker, R.; Yen, M.; Zhao, J.; Zang, L. *Journal of the American Chemical Society* **2006,** 128, (22), 7390-7398.

9. Tang, T.; Qu, J.; Müllen, K.; Webber, S. E. *Langmuir* **2005,** 22, (1), 26-28.

10. Clark, A. E.; Qin, C.; Li, A. D. Q. *Journal of the American Chemical Society* **2007,** 129, (24), 7586-7595.

11. Liu, S.-G.; Sui, G.; Cormier, R. A.; Leblanc, R. M.; Gregg, B. A. *The Journal of Physical Chemistry B* **2002,** 106, (6), 1307-1315.

12. Struijk, C. W.; Sieval, A. B.; Dakhorst, J. E. J.; van Dijk, M.; Kimkes, P.; Koehorst, R. B. M.; Donker, H.; Schaafsma, T. J.; Picken, S. J.; van de Craats, A. M.; Warman, J. M.; Zuilhof, H.; Sudhölter, E. J. R. *Journal of the American Chemical Society* **2000,** 122, (45), 11057-11066.

13. Ahrens, M. J.; Sinks, L. E.; Rybtchinski, B.; Liu, W.; Jones, B. A.; Giaimo, J. M.; Gusev, A. V.; Goshe, A. J.; Tiede, D. M.; Wasielewski, M. R. *Journal of the American Chemical Society* **2004,** 126, (26), 8284-8294.

14. Kaiser, T. E.; Wang, H.; Stepanenko, V.; Würthner, F. *Angewandte Chemie International Edition* **2007,** 46, (29), 5541-5544.

15. Schwartz, E.; Palermo, V.; Finlayson, C. E.; Huang, Y.-S.; Otten, M. B. J.; Liscio, A.; Trapani, S.; González-Valls, I.; Brocorens, P.; Cornelissen, J. J. L. M.; Peneva, K.; Müllen, K.; Spano, F. C.; Yartsev, A.; Westenhoff, S.; Friend, R. H.; Beljonne, D.; Nolte, R. J. M.; Samorì, P.; Rowan, A. E. *Chemistry – A European Journal* **2009,** 15, (11), 2536-2547.

16. Huang, K.; Rhys, A. *Proceedings of the Royal Society of London. Series A. Mathematical and Physical Sciences* **1950,** 204, (1078), 406-423.

17. Spano, F. C. *The Journal of Chemical Physics* **2005,** 122, (23), 234701-15.

18. Ford, W. E.; Kamat, P. V. *The Journal of Physical Chemistry* **1987,** 91, (25), 6373-6380.

19. Bisht, P. B.; Fukuda, K.; Hirayama, S. *Chemical Physics Letters* **1996,** 258, (1–2), 71-79.

Chapter 5: Device physics of lateral organic photovoltaics: theory and experiment to understand charge separation and transport

5.1 Introduction

Organic photovoltaic cells have been actively studied for over 20 years and even though power conversion efficiencies have reached about 10%,[1] there is still much to be learned about the transport of charge carriers and recombination mechanisms within these devices. Researchers have employed several methods to study transport and recombination in bulk heterojunction (BHJ) solar cells, including: ambipolar thin film transistors,[2-4] transient photocurrents,[5] time-resolved microwave conductivity,[6] and photo-generated charge extraction in a linearly increasing voltage (photo-CELIV).[7-9] These reports have typically focused on measurements of vertical solar cell devices, but most techniques require measurement setups that analyze the transient response of solar cells. To enable steady state carrier transport measurements, we have employed a lateral BHJ device structure which was first reported earlier this year,[10] and is shown in figure 1. These structures allow measurements with length scales ranging from 10's of nm to more than 100's of μm. In contrast to vertical OPV cells in which the active layer is buried beneath metal layers and/or transport layers, the exposed nature of the active material in lateral OPVs allows for the use of spectroscopic and microscopic tools to probe charge carriers along the transport direction. Although the geometry and direction of current flow in lateral BHJ devices is different from vertical OPV devices, the carrier transport

and recombination parameters investigated using these lateral device structures provide key insights into BHJ materials and are complementary to studies performed on vertical solar cell structures. In this article, we report on the use of common confocal microscopy tools to probe charge carrier transport and operational regimes within lateral BHJ structures.

Within lateral BHJ devices, three distinct charge transport regimes occur when the total transport distance of charge carriers is longer then their drift length.[10-11] The drift length of a charge carrier is the product of the carrier's mobility, its lifetime, and the electric field acting on the carrier. Adjacent to the electrodes, space charge regions (SCR) form and most photogenerated carriers within these regions are collected in the form of photocurrent. The photocurrent flowing in the SCRs is described by

$$\boldsymbol{J_{photo} = (4\varepsilon\mu)^{1/4}(qG)^{3/4}V^{1/2}} \quad (1)$$

where ε is the dielectric constant, μ is the mobility of the accumulated charge carrier, q is the elementary charge, G is the carrier generation rate, and V is the voltage drop in the SCR.[12] Sandwiched between the SCRs, a central recombination zone will form where there is little net photogeneration and high recombination. The electrical current flowing within this zone should exhibit an ohmic behavior, which has also been recently shown.[13] The existence of a single SCR has been previously shown in many reports and would be expected in devices with short transit lengths.[10,12,14] A more recent report from Danielson *et al.*[14] as well as this report demonstrate evidence for two SCRs as well as the central recombination zone due to the increased length that charge carriers travel before extraction.

5.2 Device Theory and Numerical Simulations

The device physics of lateral BHJ devices represents a combination of photovoltaic and photoconductor physics as a result of the device geometry and mode of electrical operation. This combination of geometry and operational mode results in space charge limited device physics, which has been reported within OPV cells[15] as well as lateral BHJ devices.[16,17] Previous theoretical work predicts three transport zones where there is efficient carrier collection near (or within a drift length of) the two electrodes and a central region where very little photocurrent can be collected.[18] When there is significant asymmetry between electron and hole mobilities, one of the space charge regions (SCRs) becomes very small and the device can be considered as possessing two transport zones: one SCR and one recombination zone. Recently, Ooi *et al*. have simulated a lateral BHJ device which shows the presence of two transport regions: a space charge region where there is an accumulation of the slower carrier (carrier with lower mobility) and a recombination zone where there is little net photogeneration and most carriers recombine.[17] This simulation solves Poisson's equation as well as the drift/diffusion under appropriate boundary values to determine the carrier concentration of electrons and holes as well as the electric field and potential profile throughout the device. Full details of the numerical simulation can be found within the aforementioned reference.

In order to simulate a device with two SCRs and a central recombination zone, the asymmetry in carrier mobilities was reduced (from a factor of 10) and the simulation was run for a 20 μm lateral BHJ device where the electron mobility (μ_e) was 1.5 x 10^{-3} $cm^2/V*s$, the hole mobility (μ_h) was 1.0 x 10^{-3} $cm^2/V*s$, an applied reverse bias of 200 V, a generation rate of (G) 1.0 x 10^{21} $cm^{-3}s^{-1}$, and a bimolecular recombination coefficient (k_{BI}) of 1.0 x 10^{-12} cm^2/s. The anode for hole extraction is located at *x=0* μm and the cathode for electron extraction is located at *x=20* μm. The resulting carrier concentration as a function of position is shown in Figure 2a and the electric field and potential profile is shown in Figure 2b. Within Figure 2a, areas of unipolar carrier accumulation occur next to each electrode; holes near the anode and electrons near the cathode. The accumulation of charge carriers occurs within a few microns of each electrode because carriers are transported into this region more quickly than they can be extracted. If the potential drop in the recombination zone is small, then the *J-V* characteristics of the entire device can be described by Equation 1:

$$J_{photo} = (4\varepsilon\mu)^{1/4}(qG)^{3/4}V^{1/2} \quad (1)$$

where ε is the dielectric constant, μ is the mobility of the slower carrier, q is the elementary charge, and V is the voltage applied. Within the central zone both electrons and holes are present in approximately equal populations and most of these carriers recombine. This is a result of a small (but non-zero) electric field present within this central region, which is more than an order of magnitude smaller as compared to within the adjacent SCRs. Carriers within the recombination zone should follow ohmic *J-V* characteristics.

By comparing the carrier concentration profile (Figure 2a) and the potential profile (Figure 2b), the extents of the SCRs can be determined in multiple ways. Areas with asymmetric carrier densities are characteristic of SCRs while areas with high symmetric carrier densities are present within the recombination zone. Similarly, within the SCRs there is a roughly linear decrease in electric field as you move away from the electrode with a smaller constant electric field within the recombination zone. Transitions between the SCRs and the recombination zone can be demarcated by large changes in carrier concentration, electric field, or changes in the slope of the potential profile, and net photogeneration rate.

In addition to simulations of lateral BHJ devices with uniform illumination and applied bias, we also simulated an experiment based on non-uniform illumination, which is useful to researchers who would like to spatially resolve transport parameters within BHJ materials. This has been demonstrated recently with an experimental method called Scanning Confocal Photocurrent Microscopy (SCPM), which utilizes common confocal microscopy tools.[19] SCPM measurements have been used to determine the size of the SCRs with a lateral BHJ device under various biasing and illumination conditions. The total photocurrent of the same 20 μm lateral BHJ device was simulated for a laser spot with a FWHM of 0.5 μm at many discrete points along the transport channel. The total collected photocurrent as a function of excitation position is shown as the discrete points in Figure 2a. The areas of high collected photocurrent correspond to the extents of the SCRs adjacent to each electrode. Between the SCRs, there is a greatly reduced amount of photocurrent being collected as the laser excitation occurs within the recombination

zone and most of the photogenerated charges recombine. For laser excitation within the recombination zone, the total simulated photocurrent is 141 mA/cm^2. This is same value for simulations that only have uniform illumination and no positional dependent laser excitation which confirms that in an ideal system, any photogenerated carriers within the recombination zone recombine and do not contribute to the overall net photocurrent within a lateral BHJ device.

5.3 Photocurrent vs. Device Length

Photocurrent vs. device length from P3HT:PCBM lateral BHJ devices with lengths ranging from 100 nm to 20 μm were measured under AM1.5 illumination at various reverse bias conditions and are shown in Figure 3. The photocurrent increases as a function of reverse bias as well as of device length until the device length reaches about 5 μm. This is expected as most carriers that are photogenerated in the SCRs will be efficiently extracted and will contribute to photocurrent within the device. As the size of the SCRs has been previously shown to be 2-5 μm in these materials under the stated experimental conditions,[12,15,16] increases in device length up to this point should contribute to additional extracted photocurrent. As the device length continues to increase, only the length of the recombination zone – and not the SCRs – increases and very few additional carriers will exit the device and contribute to photocurrent. This transit length characteristic is shown in the inset of Figure 3 where device length is plotted on a linear scale. As the device length increases beyond 5 μm, the photocurrent flowing in the BHJ device saturates due to a few additional photogenerated carriers contributing to the photocurrent. The trends present in the photocurrent vs. device length data support the

existence of three transport regions and their characteristics described in the theory section.

5.4 Scanning Confocal Microscopy

The technique of Scanning Confocal Photocurrent Microscopy (SCPM) is one where an electronic device is raster scanned across a focused laser beam and the extracted photocurrent is measured via lock-in detection. This creates a map of the photogenerated carrier collection as a function of the location of carrier generation. Additionally, reflection and fluorescence information can be simultaneously acquired using the SCPM technique, which allows for the spectroscopic analysis of samples being tested.[24] SCPM is related to a technique called laser beam induced current (LBIC) which has been previously used to study morphology, photocurrent generation, and local current vs. voltage analysis in numerous material systems used for photovoltaic cells including silicon,[25] cadmium telluride,[26] copper indium gallium diselenide,[27] and organic BHJs.[28, 29] A schematic illustration of the SCPM measurement setup is shown in figure 4a.

SCPM measurements were performed on a 20 μm long lateral BHJ device with a BHJ layer of PSBTBT, poly[(4,4′-bis(2-ethylhexyl)dithieno[3,2-b:2′,3′-d]silole)-2,6-diyl-alt-(2,1,3-benzothiadiazole)-4,7-diyl], and PCBM, [6,6]-phenyl C_{61}-butyric acid methyl ester, at applied bias values of -100 V, -150 V, and -200 V and with a white light bias when appropriate. The applied bias values correspond to electric field strengths of -0.5 x 10^5 V/cm, -0.75 x 10^5 V/cm, and -1.0 x 10^5 V/cm respectively and are consistent with the internal electric field strength found in typical OPV devices at short circuit conditions. A schematic illustration of the lateral BHJ device structure is shown in Figure 4b and a

reflectance image of the measured lateral BHJ device is shown in Figure 4c. The reflectance image shows that the light reflected by the aluminum cathode is greater then the amount of reflected light coming off the gold anode, and this can be used to confirm the orientation of the device during measurement. A complete description of the measurement setup and device architecture can be found in the *Experimental* section.

An SCPM photocurrent image taken at –100 V applied bias and no white light bias is shown in Figure 5a. Photocurrent peaks can be seen extending inward a few microns from either electrode. These areas of high carrier collection efficiency correspond to the lateral extents of the SCRs. Between the SCRs, there is a region of low photocurrent (carrier collection efficiency), which corresponds to the recombination zone. Photocurrent maps taken at -150 V and -200 V applied biases are shown in Figure 5b and Figure 5c respectively. As the applied bias increases, the photocurrent peak heights as well as the extents of the space charge regions also increase.

The device architecture allows all the lines in the photocurrent map to be averaged to generate photocurrent collection profiles that can be used to quantify the SCR regions. The data in Figs. 5a-c were used to create the profiles shown in Fig. 2d. Several different methods were used to quantify the decay of the photocurrent peak. Fitting the portion of the peak adjacent to the SCR with an exponential decay yielded the smallest residuals. As a result, the photocurrent collected as a function of laser excitation position is modeled as $\boldsymbol{J \propto e^{-(\frac{x}{L_{C'}})}}$ for electrons and $\boldsymbol{J \propto e^{(\frac{x-L}{L_{A'}})}}$ for holes in the case where the cathode is located at $\boldsymbol{x = 0}$ and the anode is located at $\boldsymbol{x = L}$. The finite diameter of

the laser spot results in a peak in the collected photocurrent that is not directly at the edge of the electrode. In the case of both the anode and the cathode, the peak is shifted by ~2.1 μm toward the center of the device. Taking into account this instrument broadening, the length of the SCR adjacent to the cathode is $\boldsymbol{L_C = \sqrt{L_C'^2 + (2.1\,\mu m)^2}}$ and the length of the SCR region adjacent to the anode is $\boldsymbol{L_A = \sqrt{L_A'^2 + (2.1\,\mu m)^2}}$. Fitting to the data in Fig. 2d, the length of the space charge region adjacent to the cathode is 2.50 μm, 2.67 μm, and 2.83 μm for applied biases of -100 V, -150 V, and -200 V respectively. Similarly, the length of the space charge region adjacent to the anode is 2.77 μm, 3.07 μm, and 3.26 μm for applied biases of -100 V, -150 V, and -200 V respectively.

To determine the effect of adding white light to the system, the above SCPM measurements were repeated with a white light bias of 150 mW/cm^2. It is predicted that the addition of photogenerated carriers via a constant white light source will fill energetic traps and should increase distance from the electrodes where photogenerated carriers can be efficiently collected. The carriers that are generated from the white light source will not be measured in the photocurrent collection as they will be filtered out by the lock-in detection. Fig. 6a shows the photocurrent mapping with an applied bias of -100 V and a 150 mW/cm^2 white light bias. By comparing the SCPM measurements with and without light bias, the addition of a white light bias increases the size of the space charge region by about 40% for both electrons and holes. SCPM photocurrent maps for applied biases of -150 V and -200 V under a white light bias of 150 mW/cm^2 are shown in Figure 6b

and Figure 6c respectively. For these increased voltage biases, the length of the SCRs have increased under white light bias as compared to dark conditions.

Using the data analysis procedure described previously, the photocurrent maps have been averaged over all rows in the image to create a photocurrent profile under white light bias, which is shown in Fig. 3d. Using the same data fitting methodology, the length of the SCRs have been extracted under white light bias. The length of the space charge region adjacent to the cathode is 3.66 μm, 4.07 μm, and 4.87 μm and the length adjacent to the anode is 3.66 μm, 4.47 μm, and 4.88 μm for applied biases of -100 V, -150 V, and -200 V respectively. All of the extracted drift length values for the 20 μm lateral BHJ device are listed in Table 1.

Since the lengths of the space charge regions for the cathode and the anode are equal under white light bias, the mobility of electrons and holes should be approximately equal and can be extracted using Eq. 1. By setting the photocurrent equal to -200 nA which is the total measured photocurrent with an applied bias of -200 V, the mobility of both electrons and holes is roughly $3x10^{-4}$ $cm^2/V*s$ which is consistent with previous reports of PSBTBT:PCBM.[8, 20-22]

As these results clearly demonstrate, the SCPM technique is capable of directly measuring the spatial extents of the space charge regions in lateral BHJ devices. The lateral extent of the space charge regions in the PSBTBT:PCBM system are a 3-7 μm which should not be a efficiency limiting factor for use in vertical OPV cell structures as the typical vertical OPV cell has a carrier transit distance which is no more than a few hundred nanometers. However, the size of the SCRs yields important fundamental

information for studying charge carrier transport and recombination mechanisms within BHJ devices. Modifications to the applied bias and the addition of a white light bias result in predictable changes to the size of the SCR as predicted by previously published work. By comparing the size of two SCRs the asymmetry in electron and hole mobilities can be estimated. Specifically, under a white light bias and applied biases that mimic typical operating conditions, the extents of the SCRs for both the anode and cathode are approximately equal. This implies that the mobility asymmetry is low, which is to be expected from high performance OPV materials such as PSBTBT:PCBM.

It is well known that C_{70}-PCBM has shown better performance in OPV blends. To compare the changes in device function, we fabricated devices with blends of PSBTBT:C_{70}-PCBM. Figure 7a shows a typical SCPM image under a 150 mW/cm^2 white light bias of a 15 μm device, with a 100 V reverse bias. One photocurrent peak can be seen decaying away from the cathode a few microns. Figure 7b and 7c show the same image at a reverse bias of 150 V and 200 V, respectively. With increasing bias, the photocurrent peak height increases and extends outward, and a second peak grows in at the other electrode, the anode. Cross sections of the device under a reverse bias of 100 V, 150 V, and 200 V is shown in Figure 7d, in which the line scans were averaged across the entire device in order to quantify the SCR regions. The analysis of the SCR regions is reported earlier.[15] Again , the peaks do not appear at the electrodes due to the finite diameter of the laser spot, and must be corrected in the analysis. Correcting for the instrument broadening, the SCR region becomes $L_C = (L_C'^2 + (1.4\ \mu m)^2)^{1/2}$ for the cathode and likewise $L_A = (L_A'^2 + (1.4\ \mu m)^2)^{1/2}$ for the anode. Fitting the data, shown in the red

plots of Figure 7d, it was found the SCR adjacent to the cathode are 2.10 μm, 4.71 μm, and 5.50 μm for an applied reverse bias of 100 V, 150 V and 200 V, respectively. The length of the SCR adjacent to the anode was found to be 1.45 μm, 1.47 μm, and 1.48 μm. The size of the SCR region increases with increasing bias for the accumulated holes, and furthermore we show the SCR for accumulated holes is much greater than that for accumulated electrons for this device. Earlier we reported under white light bias with a PSBTBT:PCBM (C_{61}) device the SCRs for electronics and holes were nearly equal. However, here we have shown replacing the acceptor with C_{71}-PCBM greatly increases the transit lengths of the holes, but the electron transport length greatly diminishes. However, it is found the overall device performance of a vertical cell is enhanced with C_{71}-PCBM, which we attribute to a greater absorption in the visible wavelengths.[28] Table 2 shows the size of the space charge regions in each of the materials (P3HT:PCBM, PSBTBT:PCBM, and PSBTBT:C_{70}-PCBM). Based on these results, we believe that using BHJ materials with matched electron and hole mobilities will result in OPV cells with increased power conversion efficiencies compared to devices which have highly asymmetric carrier mobilities.

SCPM and other measurements of lateral BHJ devices provide charge transport and recombination information that is complementary to what can be acquired from traditional vertical OPV devices. For example, changes in morphology of a device can be studied using SCPM and directly related to changes in SCR. This information on the loss mechanisms within BHJ materials can provide researchers with insight on how to better

optimize BHJ materials and device architectures which is critical to improving device efficiency.

5.5 Experimental

Lateral BHJ Devices: Lateral BHJ devices were fabricated on a glass substrate. Asymmetric electrodes were defined through two sets of photolithography: one for the aluminum (Al) cathodes and one for the gold (Au) anodes. These metals were chosen to help suppress reverse bias carrier injection within the lateral BHJ device. Each of these metals was thermally evaporated with a thickness of 500 Å. The device length was either 15 or 20 μm with a $W/L = 50$. Before deposition of the BHJ layer, the substrate was dipped in a phosphoric acid solution to dissolve any aluminum oxide present on the surface of the Al electrodes. This was followed by a solvent clean to degrease the substrate, which consisted of acetone, methanol, and isopropyl alcohol. The BHJ absorber layer was deposited from a 12 mg/mL solution of PSBTBT:C_{60}-PCBM (Or C70) (1:1.5 by weight) dissolved in dichlorobenzene that was heated to 120° C for more than 12 hours. The BHJ was spun-cast on the prepared substrates at 1000 rpm for 60 seconds and this was followed by encapsulation and annealing at 120° C for 10 min. in a nitrogen atmosphere.

Scanning Confocal Photocurrent Microscopy: The image maps were obtained using an Ar Ion Laser selected at 514 nm for excitation, which was focused through a extra long

working distance 60x magnification Nikon objective. The size of the focal spot was estimated to be ~600 nm in diameter as determined by scanning across a step edge in a patterned metal film. For sample scanning capabilities a Physik Instrumente (PI) piezoelectric stage (model E-501.00) was mounted onto a Nikon Diaphot 300 inverted microscope. The excitation beam was chopped at 140 Hz using a Thorlabs Optical Chopper (Model MC2000). The photocurrent flowing in the lateral BHJ device was amplified using a Stanford Research Systems model SR570 low noise current preamplifier and measured using a Stanford Research Systems model SR830 lock-in amplifier. The fluorescence and reflectance were collected simultaneously using a 50/50 beam splitter and were collected using two Micro Photon Devices (MPDs). The lateral BHJ devices were biased using a Keithley 6430 Sub-Femtoamp Remote SourceMeter. White light illumination was provided using the quartz tungsten halogen microscope illuminator provided with the Nikon Diaphot 300 inverted microscope and had an intensity of 150 mW/cm^2.

SCR Exponential Fitting: The lateral extents of the SCRs were fit using IGOR Pro 6.22A. The convolution of a gaussian beam profile and an exponential decay function to model the photocurrent profile leads to some areas within the data profile which are not exponential. These regions occur near the edge of the device where the photocurrent peak occurs as well as in the central recombination zone where the photocurrent is low. Therefore, the areas used to fit to the length of the SCRs were chosen by plotting the photocurrent data on a log scale and fitting only the portion of the photocurrent profile

that is approximately linear. This produces regions of data to be fit along the central shoulders of the peaks. Additionally the error in the length of the SCRs has been determined to be not larger than 250 nm.

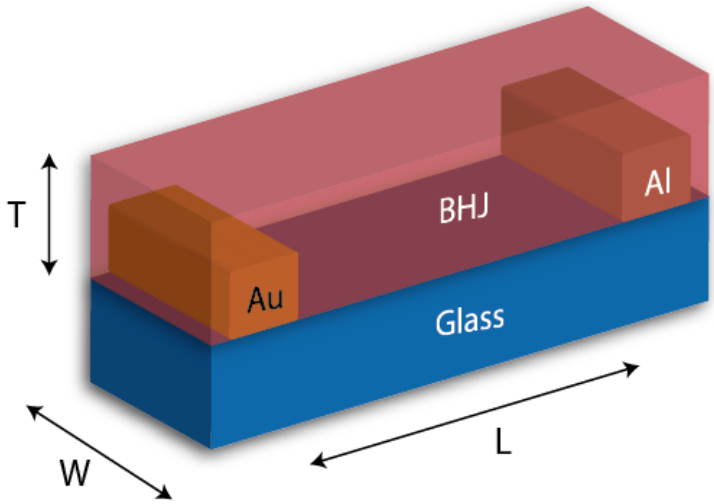

Figure 5.1: Schematic of a lateral organic photovoltaic (LOPV).

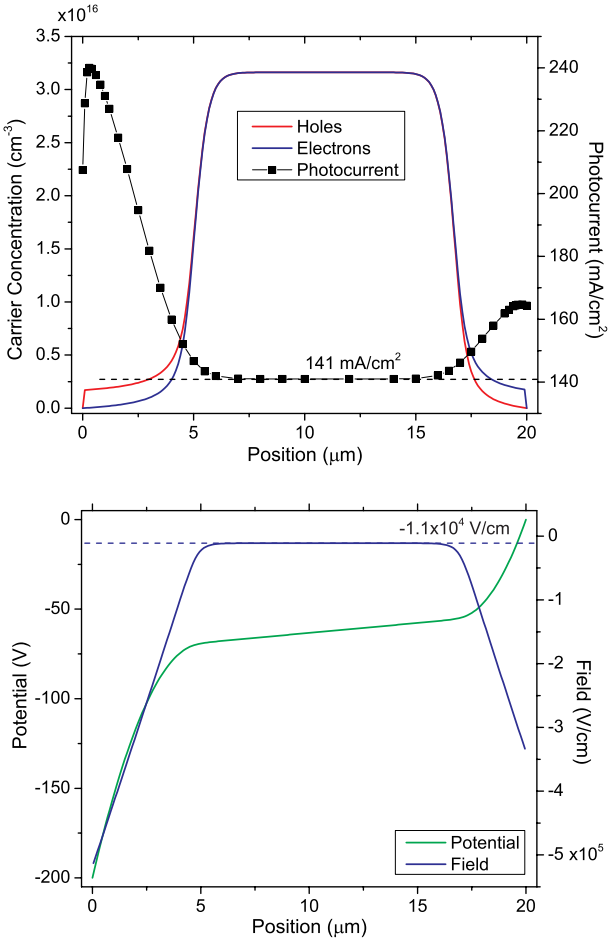

Figure 5.2: a) Carrier concentration as a function of position (solid lines) for a numerically simulated 20 μm lateral BHJ device under uniform illumination. The dotted line shows the amount of collected photocurrent as a function of excitation position with a simulated laser spot with a FWHM of 0.5 μm as well as uniform illumination. b) Simulated electric field and potential profile for the same 20 μm lateral BHJ device.

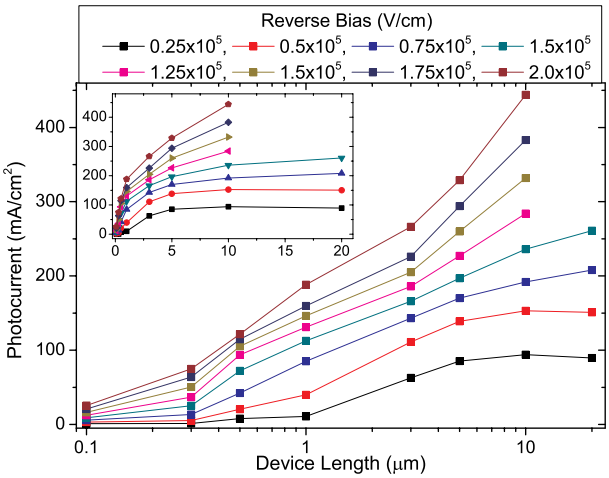

Figure 5.3: Photocurrent vs. device length (log-scale) for P3HT:PCBM lateral BHJ devices. (Inset) Photocurrent vs. device length (linear-scale) for the same devices.

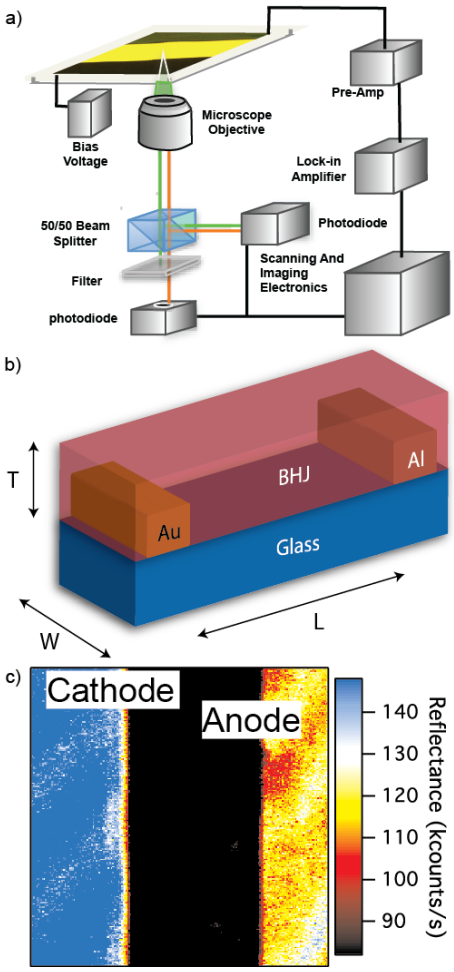

Figure 5.4: a) An illustration of a scanning confocal photocurrent microscopy (SCPM) experimental setup, b) an illustration of a lateral BHJ device, and c) a reflectance image of a 20 μm lateral BHJ device made from PSBTBT:PCBM.

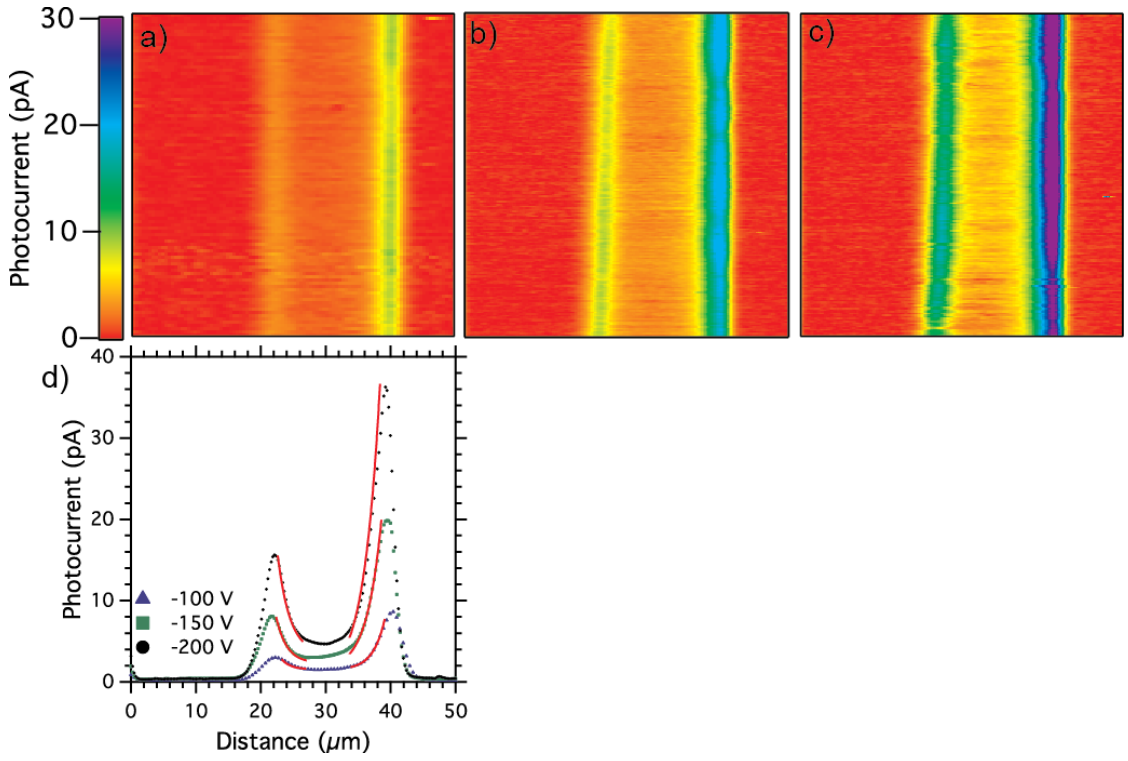

Figure 5.5: Photocurrent maps taken from a 20 μm lateral BHJ device with a a) -100 V, b) -150 V, c) -200 V externally applied bias. d) Extracted photocurrent profiles (dots) and data fits (red lines) to extract the SCR lengths from the same lateral BHJ device. Photocurrent maps are 50 μm x 50 μm.

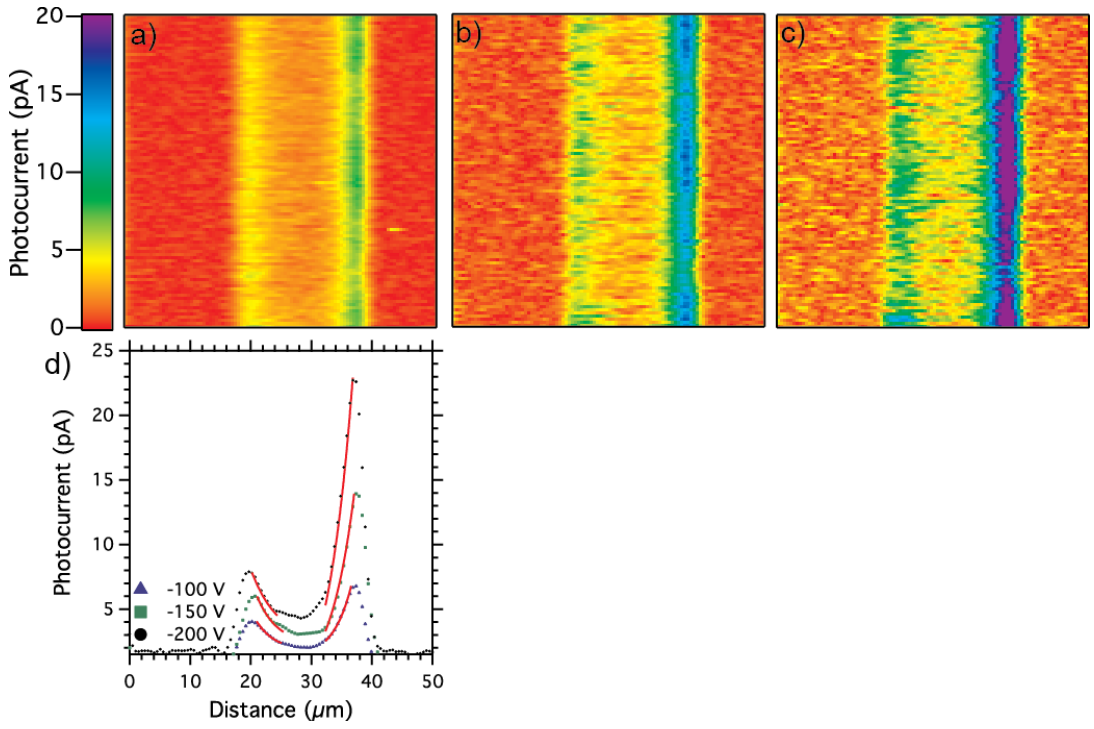

Figure 5.6: Photocurrent maps taken from a 20 μm lateral BHJ device under 150 mW/cm^2 white light bias with a a) -100 V, b) -150 V, c) -200 V externally applied bias. d) Extracted photocurrent profiles (dots) and data fits (red lines) to extract the SCR lengths from the same lateral BHJ device. Photocurrent maps are 50 μm x 50 μm.

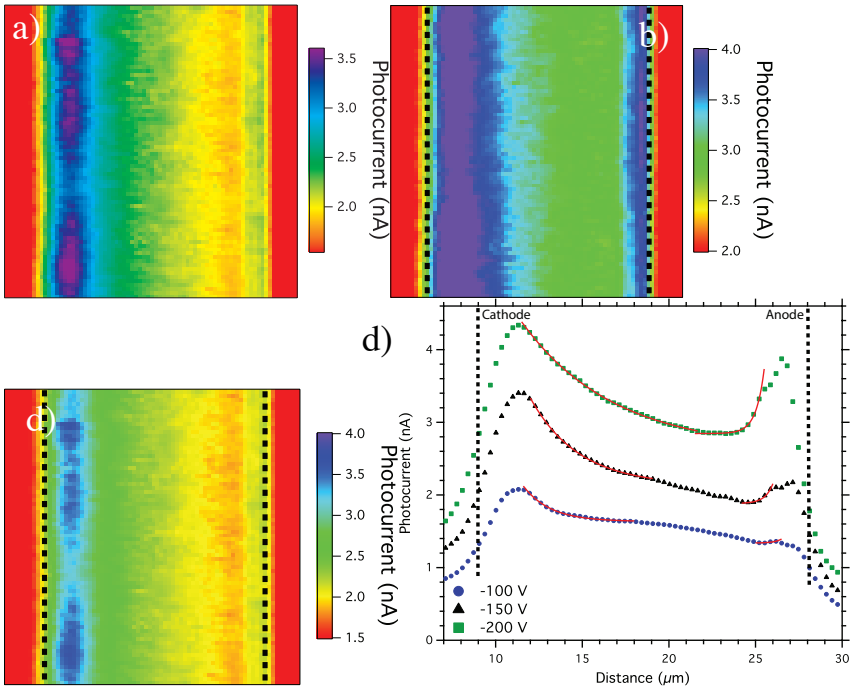

Figure 5.7: Photocurrent maps taken from a 15 μm PSBTBT:C_{71}-PCBM lateral BHJ device under 150 mW/cm^2 white light bias with an externally applied reverse bias of a) 100 V, b) 150 V, and c) 200 V. d) Extracted photocurrent profiles (dots) and data fits (red lines) to extract the SCR lengths from the same lateral BHJ device. Photocurrent maps are 32 μm x 32 μm.

Applied Bias	No White Light Bias		White Light Bias	
	Cathode SCR Length	Anode SCR Length	Cathode SCR Length	Anode SCR Length
-100 V	2.50 μm	2.77 μm	3.66 μm	3.66 μm
-150 V	2.67 μm	3.07 μm	4.07 μm	4.47 μm
-200 V	2.83 μm	3.26 μm	4.87 μm	4.88 μm

Table 5.1: Extracted SCR lengths for the SCPM measurements made at -100 V, -150 V, and -200 V applied bias with and without a white light bias.

Applied Field (V/cm)	P3HT:PCBM		PSBTBT:PCBM[12]		PSBTBT:C_{71}-PCBM	
	Cathode SCR	**Anode SCR**	**Cathode SCR**	**Anode SCR**	**Cathode SCR**	**Anode SCR**
0.5 x 10^5	2.3 μm	2.7 μm	3.7 μm	3.7 μm		
0.66 x 10^5					2.1 μm	1.5 μm
0.75 x 10^5			4.1 μm	4.5 μm		
1.0 x 10^5			4.9 μm	4.9 μm	4.7 μm	1.5 μm
1.3 x 10^5					5.5 μm	1.5 μm

Table 5.2: Lateral extent of the space charge regions for various BHJ materials

1. M. A. Green, K. Emery, Y. Hishikawa, W. Warta, E. D. Dunlop, Progress in Photovoltaics: Research and Applications 2012, 20, 12.

2. C. Lombardo, E. Danielson, Z. E. Ooi, A. Dodabalapur, Journal of Photonics for Energy 2012, 2, 021007.

3. C. Lombardo, A. Dodabalapur, Applied Physics Letters 2010, 97, 233302.

4. H. Bronstein, Z. Chen, R. S. Ashraf, W. Zhang, J. Du, J. R. Durrant, P. Shakya Tuladhar, K. Song, S. E. Watkins, Y. Geerts, M. M. Wienk, R. A. J. Janssen, T. Anthopoulos, H. Sirringhaus, M. Heeney, I. McCulloch, Journal of the American Chemical Society 2011, 133, 3272.

5. R. A. Street, S. Cowan, A. J. Heeger, Physical Review B 2010, 82, 121301.

6. A. J. Ferguson, N. Kopidakis, S. E. Shaheen, G. Rumbles, The Journal of Physical Chemistry C 2011, 115, 23134.

7. R. Österbacka, A. Pivrikas, G. Juska, K. Genevicius, K. Arlauskas, H. Stubb, Current Applied Physics 2004, 4, 534.

8. T. M. Clarke, D. B. Rodovsky, A. A. Herzing, J. Peet, G. Dennler, D. DeLongchamp, C. Lungenschmied, A. J. Mozer, Advanced Energy Materials 2011, 1, 1062.

9. D. A. M. Egbe, S. Tüirk, S. Rathgeber, F. Kühnlenz, R. Jadhav, A. Wild, E. Birckner, G. Adam, A. Pivrikas, V. Cimrova, G. n. Knöir, N. S. Sariciftci, H. Hoppe, Macromolecules 2010, 43, 1261.

10. C. Lombardo, Z.-E. Ooi, E. Danielson, A. Dodabalapur, Organic Electronics 2012, 13, 1185.

11. A. M. Goodman, A. Rose, Journal of Applied Physics 1971, 42, 2823.

12. Z.-E. Ooi, K. L. Chan, C. J. Lombardo, A. Dodabalapur, Applied Physics Letters 2012, Submitted for Publication.

13. E. Danielson, C. Lombardo, Z.-E. Ooi, A. Dodabalapuar, Advanced Materials 2012, Submitted for Publication.

14. V. D. Mihailetchi, J. Wildeman, P. W. M. Blom, Physical Review Letters 2005, 94, 126602.

15. Mihailetchi, V. D.; Wildeman, J.; Blom, P. W. M. *Physical Review Letters* 2005, *94*, 126602.

16. Lombardo, C.; Ooi, Z.-E.; Danielson, E.; Dodabalapur, A. *Organic Electronics* 2012, *13*, 1185.

17. Ooi, Z. E.; Chan, K. L.; Lombardo, C. J.; Dodabalapur, A. *Applied Physics Letters* 2012, *101*, 053301.

18. Goodman, A. M.; Rose, A. *Journal of Applied Physics* 1971, *42*, 2823.

19. Lombardo, C. J.; Glaz, M. S.; Ooi, Z.-E.; Bout, D. A. V.; Dodabalapur, A. *Physical Chemistry Chemical Physics* 2012, *In Press*.

20. Danielson, E.; Lombardo, C. J.; Ooi, Z.; Dodabalapur, A. *Organic Electronics* 2012, *Under Review*.

21. Koster, L. J. A.; Mihailetchi, V. D.; Blom, P. W. M. *Applied Physics Letters* 2006, *88*, 052104.

22. Mozer, A. J.; Dennler, G.; Sariciftci, N. S.; Westerling, M.; Pivrikas, A.; Österbacka, R.; Juska, G. *Physical Review B* 2005, *72*, 035217.

23. Pivrikas, A.; Juscaronka, G.; Mozer, A. J.; Scharber, M.; Arlauskas, K.; Sariciftci, N. S.; Stubb, H.; Ouml; sterbacka, R. *Physical Review Letters* 2005, *94*, 176806.

24. D. P. Ostrowski, M. S. Glaz, B. W. Goodfellow, V. A. Akhavan, M. G. Panthani, B. A. Korgel, D. A. Vanden Bout, Small 2010, 6, 2832.

25. J. Carstensen, G. Popkirov, J. Bahr, H. Föll, Solar Energy Materials and Solar Cells 2003, 76, 599.

26. T. Potlog, L. Ghimpu, P. Gashin, A. Pudov, T. Nagle, J. Sites, Solar Energy Materials and Solar Cells 2003, 80, 327.

27. T. A. Bull, L. S. C. Pingree, S. A. Jenekhe, D. S. Ginger, C. K. Luscombe, ACS Nano 2009, 3, 627.

28. T. J. K. Brenner, C. R. McNeill, The Journal of Physical Chemistry C 2011, 115, 19364.

29. H.-Y. Chen, J. Hou, A. E. Hayden, H. Yang, K. N. Houk, Y. Yang, Advanced Materials 2010, 22, 371.

Chapter 6: Photocurrent and fluorescent mapping of P3HT:PDI devices using Near-Field Scanning Optical Microscopy and Scanning Confocal Microscopy

Introduction

Morphology of thin film photovoltaics occurs on length scales from a few nanometers to orders of magnitude larger.[1-3] Understanding the morphology on each length scale is pertinent to understanding charge generation, separation, and transfer. For example, the blend PFB (poly(9,9′-dioctylfluorene-*co*-bis-*N*,*N*′-(4-butylphenyl)-bis-*N*,*N*′-phenyl-1,4-phenylenediamine)) and F8BT (poly(9,9′-dioctylfluorene-*co*-benzodiathiazole)) form large phase segregated islands. Although PFB and F8BT do not make efficient solar cells, they have the unique ability to allow us to study the fundamental physics of charge separation and transport, due to their relatively large morphological regions. For example, the exciplex, where the hole and electron radiatively recombine from a charge-transfer state can be easily observed in these materials at the interface of the phase separated regions.[4] This work is preliminary data, in which we use three derivatives of perylene diimide (PDI) blended with poly(3-hexylthiophene) [P3HT]. PDI is used because it has a high quantum yield,[5] has a tendency to aggregate and form different molecular architectures,[6] and has also been shown to yield high mobilities in organic field effect transistors (OFETS).[7] Substituting different side chains, which also change the solubility of PDI, can change the morphology of films. Figure 1A is a perylene diimide derivative that is not very soluble

in solution with P3HT, while figure 1B is a highly soluble derivative and figure 1C is the soluble PDI attached to a polymer backbone. The three PDIs will be shortened to insoluble PDI (ns-PDI), soluble PDI (s-PDI) and polymer-PDI (PPDI) for simplicity. Additionally, the PPDI is expected to have good energy transfer due to the unique ability of self-aggregating in good solvents to form an H-aggregate, characterized in Chapter 4. Techniques to study such systems include near-field optical microscopy, conductive AFM, and confocal microscopy.[8-11] This last chapter of my dissertation is preliminary data for using near-field and confocal microscopy to image the morphological changes in photocurrent and fluorescence in different morphologies. We also report on methods to correlate chemical composition to the morphologies by obtaining fluorescent spectra at every pixel.

Results

In order to first characterize the electronic properties of the films, devices were made by spin coating PEDOT:PSS on top of patterned ITO. The active area (blend of PDI/P3HT) was then spin coated in a glove box to make an approximately 100 nm film. Finally Al was evaporated through a shadow mask to complete the device. For microscopy purposes, a 10 nm layer of Al was evaporated and the samples were imaged through the Al or the devices were made on cover glass coated with ITO, with 100 nm of Al and the devices were imaged through the glass.

Figure 2A-C show the current-voltage (IV) curves in the light and dark for the three derivatives blended with a weight ratio of 1:1 P3HT:PDI. Figure 2A is the IV curve for the S-PDI and is the most efficient device fabricated. The short circuit current (J_{SC}) is

0.516 mA/cm^2 and the V_{OC} is ~.2 V, while ns-PDI performed an order of magnitude less efficient, the V_{OC} has tripled, but the J_{SC} is only 4.324 uA/cm^2. The PPDI efficiencies (Figure 2C) are similar to the S-PDI, where the J_{SC} is slightly lower but the V_{OC} is also ~.2 volts. In order to understand why the ns-PDI performs so much worse than the other PDIs, fluorescence optical micrographs are shown in figure 3A-3C. Due to the high fluorescence yield of PDI, the red in the images is fluorescence from the PDI only and the P3HT is mostly quenched. Figure 3A is the PPDI blended with P3HT and reveals large regions of phase segregation. Figure 3B is the S-PDI with P3HT and although it also shows quite larger areas of phase segregation, it also reveals regions in which there is strong intermixing between the two materials. Finally, in figure 3C, the NS-PDI has formed crystals on top of the P3HT. Some inferences can be made from the images as to why the S-PDI are the most efficient devices, which is most likely due to the small scale intermixing of the two materials while the NS-PDI forms large crystals and appears to be weakly mixed.

In order to further explain charge generation of these materials, scanning photocurrent microscopy was employed. The method is described in the previous chapters of this dissertation. Briefly, either near-field optical microscopy (NSOM) or confocal microscopy was used to image the photocurrent and the fluorescence, simultaneously. For near-field, pulled fiber optic tips coated with 100 nm of aluminum was used to probe the sample. Laser light at 532 nm was coupled into the fiber optic, and the tip was held at a constant height while the sample was scanned in an Aurora microscope using a piezo-electric stage in order to collect topography, electrical, and

optical images.[12-15] The confocal images were collected using 514 nm laser light selected from an Ar Ion laser. The sample was imaged using a Nikon microscope with an oil immersion objective and the corresponding fluorescence and photocurrent images were simultaneously collected. An Andor EM-CCD camera was coupled into the confocal microscope to simultaneously collect the spectra at each pixel.

Figure 4A is a topography image taken with the NSOM of a P3HT:NS-PDI film. Three crystals can be seen as raised features. The photocurrent in figure 4B shows increased photocurrent in regions that correlate to the topography. Finally, fluorescence image in figure 4C shows areas in which the fluorescence spikes. The raised features correlate directly with the fluorescence and photocurrent, and are attributed to regions in which there are PDI crystals. These small crystals seen in the NSOM images reveal that the photocurrent is predominantly coming from these areas. However, there is one spike in the photocurrent in a region that does not correlate to the topography or the fluorescence, but has the same shape as the other crystals. It is believed to be an embedded crystal, completely surrounded by P3HT and the fluorescence is quenched. This image shows that the more contact the donor and acceptor materials have, the higher photocurrent observed. Also, the large amount of quenching is also a sign of significant energy transfer between the PDI crystals and the P3HT in this area.

Although NSOM has the unique ability to measure the topography and it was shown how this could be used to correlate photocurrent based on where crystals formed in the film, the low signal to noise and difficulty to make functional devices with 10 nm

of Al brought us to use confocal microscopy for the rest of the devices. Confocal is useful because the devices can be encapsulated and imaged through the ITO.

Figure 5 shows correlated photocurrent and fluorescence maps of all three PDI derivatives blended with P3HT. Figure 5A and 5D are the NS-PDI blends. The crystals are much larger than what was seen using NSOM, which is because the large crystals had to be avoided in order to achieve high resolution images, without knicking the tip. The images show high photocurrent near the edges of the crystals, and little photocurrent on top of a crystal. Most of the photocurrent is actually observed in the P3HT. This is the opposite of what was seen in the NSOM and is expected to be due to the large crystals having a lower surface area and less mixing with the P3HT. Due to the large size of the crystals, most likely the excitons cannot diffuse out of the system when generated on a large PDI crystal. Figure 5B and E are the photocurrent and fluorescence maps of S-PDI. In both images, the fluorescence and photocurrent are very uniform. Finally, in 5C and F, the photocurrent and fluorescence maps of PPDI blends show similar morphology to the fluorescence optical micrographs. The fluorescence maps in 5C and F is anti-correlated, in which the bright spots in the image appear as low fluorescence regions. However, there are features in the photocurrent image that do not correlate with the fluorescence.

The last technique developed was to simultaneously obtain fluorescence spectra at each pixel. Figure 6A-C show the normalized fluorescence in different regions of the films in figure 5. Figure 6A is of the NS-PDI blend and is the only film that shows heterogeneity. The low fluorescent region shows spectra that are very similar to P3HT

films, while the high fluorescent regions show broad peaks typical of PDI excimer emission. Most likely, this is due to the non-soluble nature of the PDI, which tends to aggregate. There is little or no PDI intermixed with the P3HT and only the crystals are PDI rich. In Figure 6B and 6C, the spectra in each region are very similar, meaning the PDI is continuously mixed with P3HT. Although, this technique cannot quantify the amount of material mixing, it can definitively answer why the NS-PDI is much less efficient. In order to obtain efficient charge separation, donor and acceptor materials must be well intermixed.

We developed microscopy techniques to image the morphology of organic photovoltaics and correlate morphology to photocurrent and fluorescence. In order to make this technique more quantifiable, it will be used in conjunction with other experiments, such as time of flight – secondary ion mass spectrometry (TOF-SIMS) in order to first reveal high-resolution chemical compositions of a film. Other such experiments should use materials that do not have overlapping fluorescence spectra. However, materials such as PDI are extremely useful because their morphologies can be well controlled. This work was able to explain how the different morphologies affected charge separation and that more intermixing of the materials leads to higher photocurrent, most likely due to the short distances that an exciton can travel before relaxing.

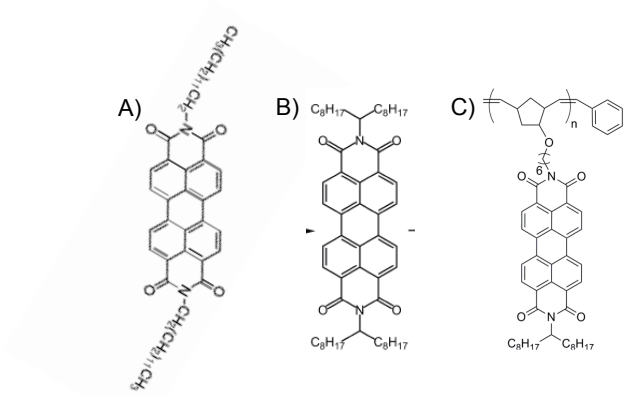

Figure 6.1: Derivatives of perylene diimide (PDI). A) is an insoluble form of PDI, B) is a soluble monomer, and C) is the soluble monomer attached to a polymer backbone.

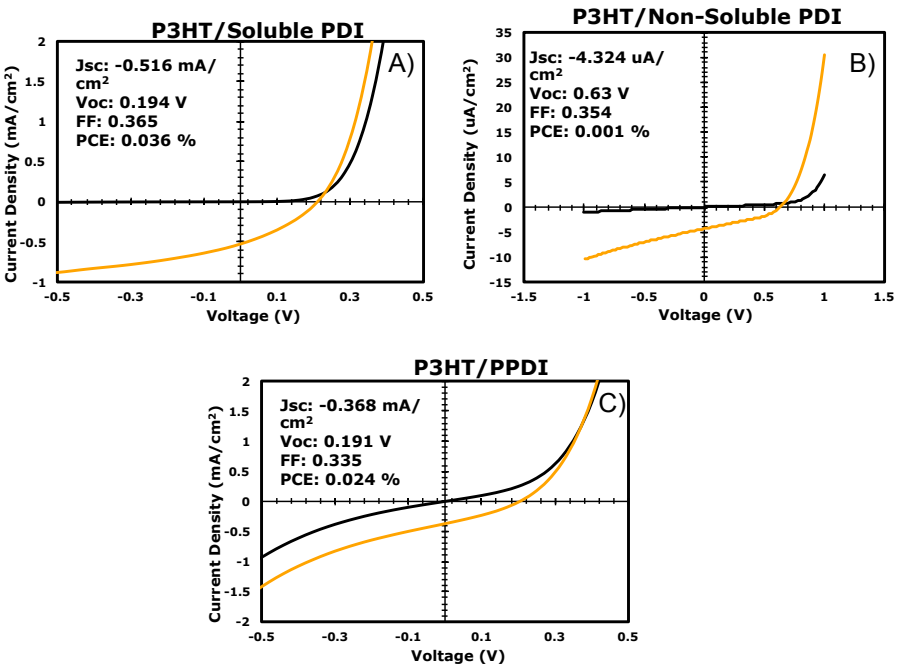

Figure 6.2: Current-voltage curves of 1:1 blends of A)P3HT/Soluble PDI, B) P3HT/Non Soluble PDI, and C) P3HT/PPDI.

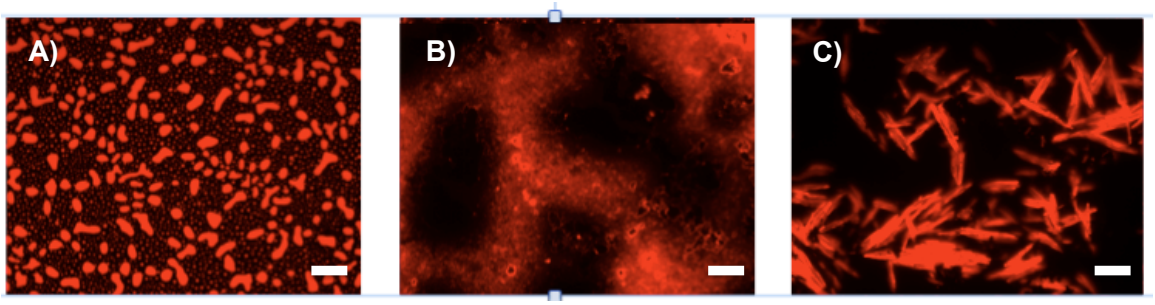

Figure 6.3: Fluorescence optical micrographs of films. Images are A) P3HT/PPDI, B) P3HT/S-PDI and C) P3HT/NS-PDI. The scale bar is 10um.

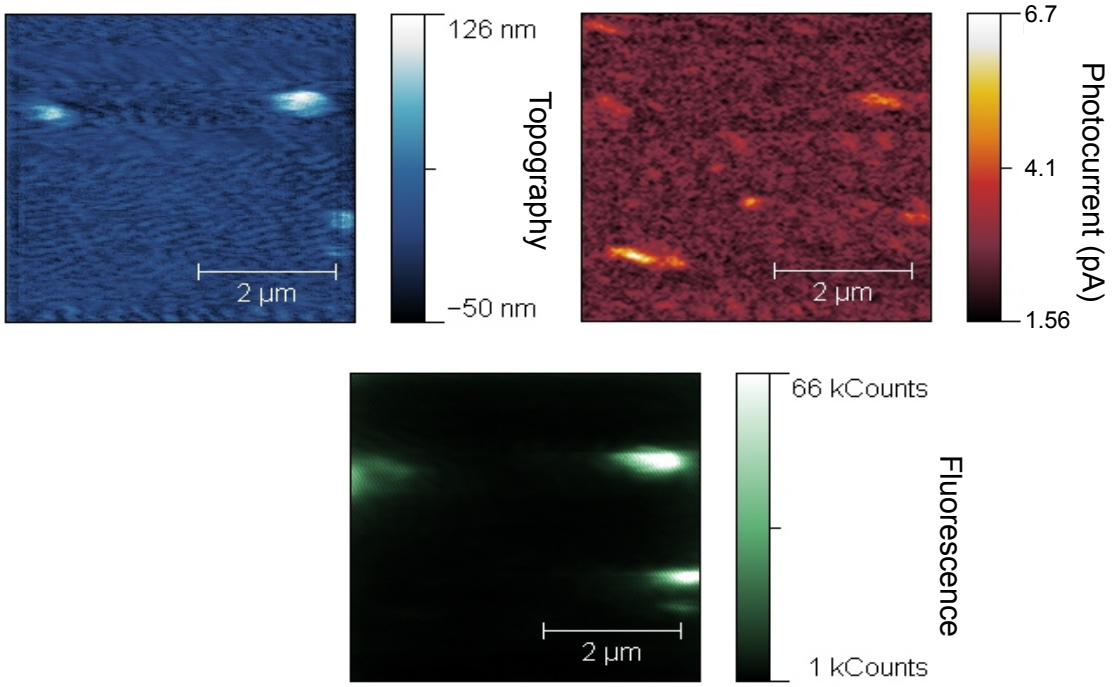

Figure 6.4: Near-field optical microscopy (NSOM) of P3HT/NS-PDI devices. A) Topography, B) Photocurrent, and C) Fluorescence taken simultaneously.

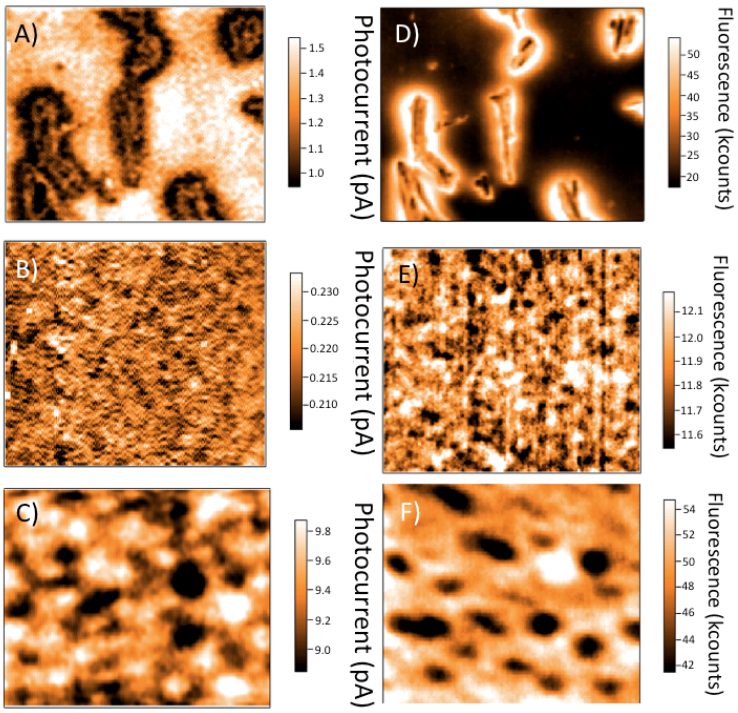

Figure 6.5: Scanning confocal microscopy images. A-C) are local photocurrent maps of P3HT/NS-PDI, P3HT/S-PDI and P3HT/PPDI, respectively. D-F) are fluorescence images of the corresponding photocurrent images taken simultaneously. Images are 20 um x 20 um.

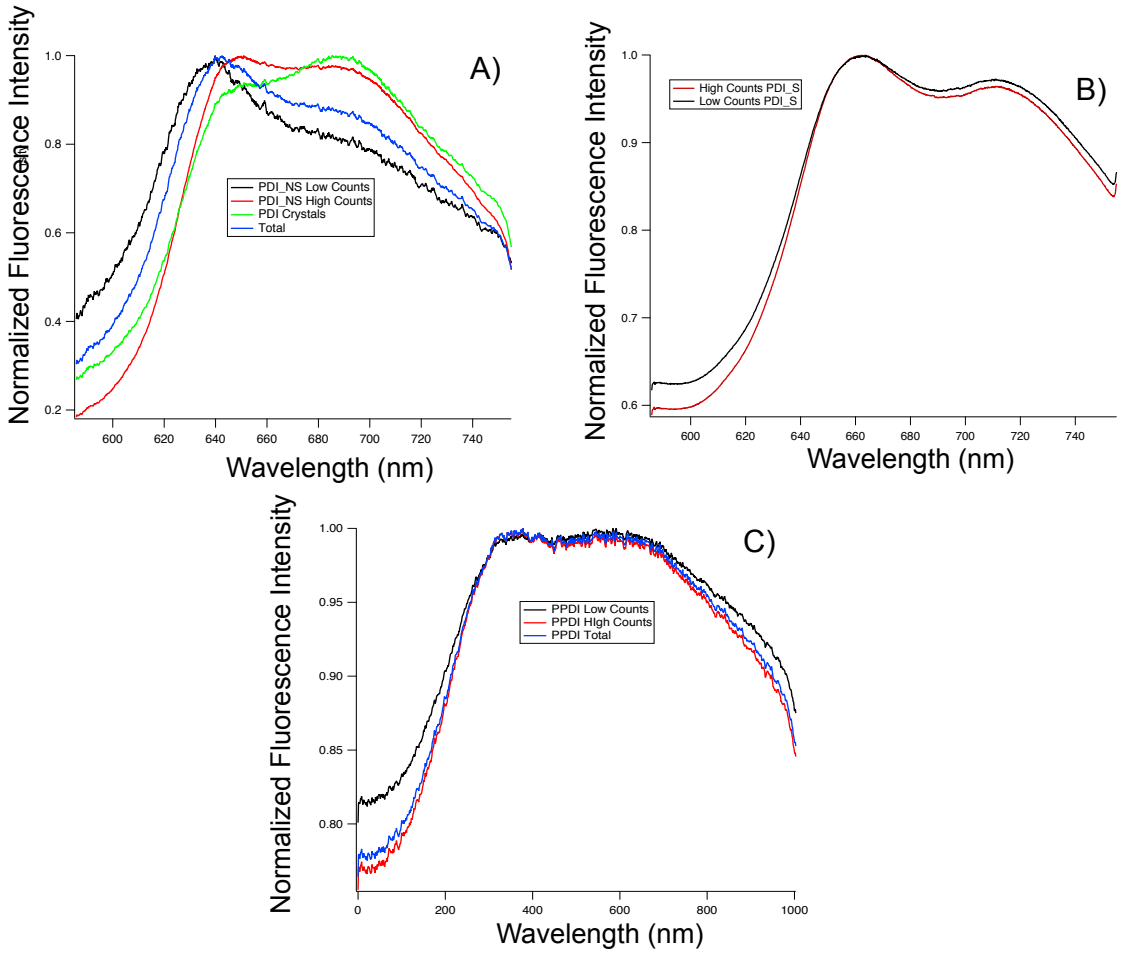

Figure 6.6: Local normalized spectra of P3HT/PDI blends. The average spetra for low and high counts are plotted. A) P3HT/NS-PDI spectra of the low fluorescent region and high fluorescent regions, as well as the PDI crystals. B) P3HT/S-PDI spectra of bright dark regions. C) P3HT/PPDI of bright and dark regions. Only in A) is there variation in fluorescence.

1. van Duren, J. K. J.; Yang, X.; Loos, J.; Bulle-Lieuwma, C. W. T.; Sieval, A. B.; Hummelen, J. C.; Janssen, R. A. J. *Advanced Functional Materials* **2004,** 14, (5), 425-434.

2. Giridharagopal, R.; Ginger, D. S. *The Journal of Physical Chemistry Letters* **2010,** 1, (7), 1160-1169.

3. Chen, W.; Xu, T.; He, F.; Wang, W.; Wang, C.; Strzalka, J.; Liu, Y.; Wen, J.; Miller, D. J.; Chen, J.; Hong, K.; Yu, L.; Darling, S. B. *Nano Letters* **2011,** 11, (9), 3707-3713.

4. Cadby, A.; Khalil, G.; Fox, A. M.; Lidzey, D. G. *Journal of Applied Physics* **2008,** 103, (9), 093715-5.

5. Tang, T.; Qu, J.; Müllen, K.; Webber, S. E. *Langmuir* **2005,** 22, (1), 26-28.

6. Schwartz, E.; Palermo, V.; Finlayson, C. E.; Huang, Y.-S.; Otten, M. B. J.; Liscio, A.; Trapani, S.; González-Valls, I.; Brocorens, P.; Cornelissen, J. J. L. M.; Peneva, K.; Müllen, K.; Spano, F. C.; Yartsev, A.; Westenhoff, S.; Friend, R. H.; Beljonne, D.; Nolte, R. J. M.; Samorì, P.; Rowan, A. E. *Chemistry – A European Journal* **2009,** 15, (11), 2536-2547.

7. Briseno, A. L.; Mannsfeld, S. C. B.; Reese, C.; Hancock, J. M.; Xiong, Y.; Jenekhe, S. A.; Bao, Z.; Xia, Y. *Nano Letters* **2007,** 7, (9), 2847-2853.

8. McNeill, C. R.; Frohne, H.; Holdsworth, J. L.; Dastoor, P. C. *Nano Letters* **2004,** 4, (12), 2503-2507.

9. McNeill, C. R.; Westenhoff, S.; Groves, C.; Friend, R. H.; Greenham, N. C. *The Journal of Physical Chemistry C* **2007,** 111, (51), 19153-19160.

10. Pingree, L. S. C.; Reid, O. G.; Ginger, D. S. *Advanced Materials* **2009,** 21, (1), 19-28.

11. Brenner, T. J. K.; McNeill, C. R. *The Journal of Physical Chemistry C* **2011,** 115, (39), 19364-19370.

12. Teetsov, J.; Vanden Bout, D. A. *The Journal of Physical Chemistry B* **2000,** 104, (40), 9378-9387.

13. Teetsov, J.; Vanden Bout, D. A. *Langmuir* **2001,** 18, (3), 897-903.

14. Blatchford, J. W.; Gustafson, T. L.; Epstein, A. J.; Vanden Bout, D. A.; Kerimo, J.; Higgins, D. A.; Barbara, P. F.; Fu, D. K.; Swager, T. M.; MacDiarmid, A. G. *Physical Review B* **1996,** 54, (6), R3683-R3686.

15. Higgins, D. A.; Vanden Bout, D. A.; Kerimo, J.; Barbara, P. F. *The Journal of Physical Chemistry* **1996,** 100, (32), 13794-13803.

Bibliography

M. Acciarri, S. Binetti, A. Racz, S. Pizzini, G. Agostinelli, *Solar Energy Materials and Solution C*. 2002, *72*, 417–424.

Ahrens, M. J.; Sinks, L. E.; Rybtchinski, B.; Liu, W.; Jones, B. A.; Giaimo, J. M.; Gusev, A. V.; Goshe, A. J.; Tiede, D. M.; Wasielewski, M. R. *Journal of the American Chemical Society* **2004,** 126, (26), 8284-8294.

V.A. Akhavan, M.G. Panthani, B.W. Goodfellow, D.K. Reid, B.A. Korgel, *Energy Express* **2010,** 18, A411–A420.

Alvarado, S. F.; Seidler, P. F.; Lidzey, D. G.; Bradley, D. D. C. *Physical Review Letters* **1998,** 81, (5), 1082-1085.

Balakrishnan, K.; Datar, A.; Naddo, T.; Huang, J.; Oitker, R.; Yen, M.; Zhao, J.; Zang, L. *Journal of the American Chemical Society* **2006,** 128, (22), 7390-7398.

Barbara, P. F.; Adams, D. M.; O'Connor, D. B. *Annual Review of Materials Science* **1999,** 29, (1), 433-469.

Betzig, E.; Finn, P. L.; Weiner, J. S. *Applied Physics Letters* **1992,** 60, (20), 2484-2486.

Bisht, P. B.; Fukuda, K.; Hirayama, S. *Chemical Physics Letters* **1996,** 258, (1–2), 71-79.

Brabec, C. J.; Zerza, G.; Cerullo, G.; De Silvestri, S.; Luzzati, S.; Hummelen, J. C.; Sariciftci, S. *Chemical Physics Letters* **2001,** 340, (3–4), 232-236.

C. J. Brabec, *Solar Energy Materials Solar C*. 2004, *83*, 273–292.

Brédas, J.-L.; Cornil, J.; Heeger, A. J. *Advanced Materials* **1996,** 8, (5), 447-452.

Bredas, J.-L, Durrant, J,R. *Accounts of Chemical Research* 2009, *42*, 1689–1690.

Brenner, T. J. K.; McNeill, C. R. *The Journal of Physical Chemistry C* **2011,** 115, (39), 19364-19370.

H. Bronstein, Z. Chen, R. S. Ashraf, W. Zhang, J. Du, J. R. Durrant, P. Shakya Tuladhar, Blom, P. W. M.; Mihailetchi, V. D.; Koster, L. J. A.; Markov, D. E. *Advanced Materials* **2007,** 19, (12), 1551-1566.

T. A. Bull, L. S. C. Pingree, S. A. Jenekhe, D. S. Ginger, C. K. Luscombe, *ACS Nano* 2009, *3*, 627–636.

A. Cadby, G. Khalil, A. M. Fox, D. G. Lidzey, *Journal of Applied Physics* 2008, *103*, 093715.

J. Carstensen, G. Popkirov, J. Bahr, H. Föll, Solar Energy Materials and Solar Cells 2003, 76, 599.

Chapin, D. M.; Fuller, C. S.; Pearson, G. L. *Journal of Applied Physics* **1954,** 25, (5), 676-677.

H.-Y. Chen, J. Hou, A. E. Hayden, H. Yang, K. N. Houk, Y. Yang, Advanced Materials 2010, 22, 371.

Chen, Z.; Dang, X.-D.; Gutacker, A.; Garcia, A.; Li, H.; Xu, Y.; Ying, L.; Nguyen, T.-Q.; Bazan, G. C. *Journal of the American Chemical Society* **2010,** 132, (35), 12160-12162.

Chen, W.; Xu, T.; He, F.; Wang, W.; Wang, C.; Strzalka, J.; Liu, Y.; Wen, J.; Miller, D. J.; Chen, J.; Hong, K.; Yu, L.; Darling, S. B. *Nano Letters* **2011,** 11, (9), 3707-3713.

Chen, Z.; Dang, X.-D.; Gutacker, A.; Garcia, A.; Li, H.; Xu, Y.; Ying, L.; Nguyen, T.-Q.; Bazan, G. C. *Journal of the American Chemical Society* **2010,** 132, (35), 12160-12162.

Chesterfield, R. J.; McKeen, J. C.; Newman, C. R.; Ewbank, P. C.; da Silva Filho, D. A.; Brédas, J.-L.; Miller, L. L.; Mann, K. R.; Frisbie, C. D. *The Journal of Physical Chemistry B* **2004,** 108, (50), 19281-19292.

Clark, A. E.; Qin, C.; Li, A. D. Q. *Journal of the American Chemical Society* **2007,** 129, (24), 7586-7595.

T. M. Clarke, D. B. Rodovsky, A. A. Herzing, J. Peet, G. Dennler, D. DeLongchamp, C. Lungenschmied, A. J. Mozer, Advanced Energy Materials 2011, 1, 1062.

Contreras, M. A.; Egaas, B.; Ramanathan, K.; Hiltner, J.; Swartzlander, A.; Hasoon, F.; Noufi, R. *Progress in Photovoltaics: Research and Applications* **1999,** 7, (4), 311-316.

Coropceanu, V.; Cornil, J.; da Silva Filho, D. A.; Olivier, Y.; Silbey, R.; Bredas, J. L. *ChemInform* **2007,** 38, (29).

Coffey, D. C.; Reid, O. G.; Rodovsky, D. B.; Bartholomew, G. P.; Ginger, D. S. *Nano Letters* **2007,** 7, (3), 738-744.

D. C. Coffey, D. S. Ginger, *Nature Materials* 2006, *5*, 735–740.

Cornil, J.; Beljonne, D.; Calbert, J. P.; Brédas, J. L. *Advanced Materials* **2001,** 13, (14), 1053-1067.

Danielson, E.; Lombardo, C.; Dodabalapur, A. *Organic Electronics* **2012**, 84770F-84770F.

Dang, X.-D.; Nguyen, T.-Q.; Cao, Y.; Bazan, G. C. *Journal of the American Chemical*

Society **2008,** 130, (11), 3282-3283.

Z. Derkaoui, Z. Kebbab, R. Miloua, N. Benramdane, *Solid State Commununications* 2009, *149*, 1231–1235.

O. Douhéret, A. Swinnen, S. Bertho, I. Haeldermans, J. D'Haen, M. D'Olieslaeger, D. Vanderzande, J. V. Manca, *Progress Photovoltaics* 2007, *15*, 713–726.

K. Durose, S. E. Asher, W. Jaegermann, D. Levi, B. E. McCandless, W. Metzger, H. Moutinho, P. D. Paulson, C. L. Perkins, J. R. Sites, G. Teeter, M. Terheggen, *Progress in Photovoltaics* 2004, *12*, 177–217.

D. A. M. Egbe, S. Tu¨rk, S. Rathgeber, F. Ku¨hnlenz, R. Jadhav, A. Wild, E. Birckner, G. Adam, A. Pivrikas, V. Cimrova, G. n. Knör, N. S. Sariciftci, H. Hoppe, Macromolecules 2010, 43, 1261.

Ellison, D. J.; Lee, B.; Podzorov, V.; Frisbie, C. D. *Advanced Materials* **2011,** 23, (4), 502-507.

Emin, S.; Singh, S. P.; Han, L.; Satoh, N.; Islam, A. *Solar Energy* **2011,** 85, (6), 1264-1282.

A. J. Ferguson, N. Kopidakis, S. E. Shaheen, G. Rumbles, The Journal of Physical Chemistry C 2011, 115, 23134.

Ford, W. E.; Kamat, P. V. *The Journal of Physical Chemistry* **1987,** 91, (25), 6373-6380.

A. Goetzberger, C. Hebling, H. W. Schock, *Materials Science and Engineering R* 2003, *40*, 1–46

Y. Q. Gao, J. K. Grey, *Journal of the American Chemical Society* 2009, *131*, 9654–9662.

Y. Q. Gao, T. P. Martin, A. K. Thomas, J. K. Grey, *Journal of Physical Chemical Letters* 2010, *1*, 178–182.

Gélinas, S.; Paré-Labrosse, O.; Brosseau, C.-N.; Albert-Seifried, S.; McNeill, C. R.; Kirov, K. R.; Howard, I. A.; Leonelli, R.; Friend, R. H.; Silva, C. *The Journal of Physical Chemistry C* **2011,** 115, (14), 7114-7119.

Giridharagopal, R.; Rayermann, G. E.; Shao, G.; Moore, D. T.; Reid, O. G.; Tillack, A. F.; Masiello, D. J.; Ginger, D. S. *Nano Letters* **2012,** 12, (2), 893-898.

Gong, X.; Wang, S.; Moses, D.; Bazan, G. C.; Heeger, A. J. *Advanced Materials* **2005,** 17, (17), 2053-2058.

Goodman, A. M.; Rose, A. *Journal of Applied Physics* 1971, *42*, 2823.

Green, M. A.; Emery, K.; Hishikawa, Y.; Warta, W.; Dunlop, E. D. *Progress in Photovoltaics: Research and Applications* **2012,** 20, (1), 12-20.

Q. Guo, G.M. Ford, H.W. Hillhouse, R. Agrawal, *Nano Lett*. **2009**, 9, 3060–3065.

Q. Guo, G. M. Ford, R. Agrawal, H. W. Hillhouse, Prog. Photovoltaics: Research and Applications **2012**, doi: 10.1002/pip.2200.

Heeger, A. J.; Bazan, G. C. *Journal of the American Chemical Society* **2009,** 131, (51), 18220-18221.

Higgins, D. A.; Kerimo, J.; Vanden Bout, D. A.; Barbara, P. F. *Journal of the American Chemical Society* **1996,** 118, (17), 4049-4058.

Higgins, D. A.; Vanden Bout, D. A.; Kerimo, J.; Barbara, P. F. *The Journal of Physical Chemistry* **1996,** 100, (32), 13794-13803.

H. Hoppe, T. Glatzel, M. Niggemann, A. Hinsch, M. C. Lux-Steiner, N. S. Sariciftci, *Nano Letters* 2005, *5*, 269–274.

Huang, K.; Rhys, A. *Proceedings of the Royal Society of London. Series A. Mathematical and Physical Sciences* **1950,** 204, (1078), 406-423.

Hutchison, G. R.; Ratner, M. A.; Marks, T. J. *Journal of the American Chemical Society* **2005,** 127, (48), 16866-16881.

Kaiser, T. E.; Wang, H.; Stepanenko, V.; Würthner, F. *Angewandte Chemie International Edition* **2007,** 46, (29), 5541-5544.

Kahn, A.; Koch, N.; Gao, W. *Journal of Polymer Science Part B: Polymer Physics* **2003,** 41, (21), 2529-2548.

P. V. Kamat, *Journal of Physical Chemistry C* 2008, *112*, 18737–18753.

Kitts, C. C.; Bout, D. A. V. *The Journal of Physical Chemistry B* **2009,** 113, (35), 12090-12095.

Kline, R. J.; DeLongchamp, D. M.; Fischer, D. A.; Lin, E. K.; Richter, L. J.; Chabinyc, M. L.; Toney, M. F.; Heeney, M.; McCulloch, I. *Macromolecules* **2007,** 40, (22), 7960-7965.

Koster, L. J. A.; Mihailetchi, V. D.; Blom, P. W. M. *Applied Physics Letters* 2006, *88*, 052104.

F. C. Krebs, *Sol. Energ. Mater. Sol. C*. 2009, *93*, 394–412.

Kulkarni, A. P.; Tonzola, C. J.; Babel, A.; Jenekhe, S. A. *Chemistry of Materials* **2004,** 16, (23), 4556-4573.

Kwak, E.-S.; Kang, T. J.; Vanden Bout, D. A. *Analytical Chemistry* **2001,** 73, (14), 3257-3262.

Lee, J.; Vandewal, K.; Yost, S. R.; Bahlke, M. E.; Goris, L.; Baldo, M. A.; Manca, J. V.; Voorhis, T. V. *Journal of the American Chemical Society* **2010,** 132, (34), 11878-11880.

Liu, S.-G.; Sui, G.; Cormier, R. A.; Leblanc, R. M.; Gregg, B. A. *The Journal of Physical Chemistry B* **2002,** 106, (6), 1307-1315.

Liu, G.; Li, A.-Y.; An, D.; Wu, H.-B.; Zhu, X.-H.; Li, Y.; Miao, X.-R.; Deng, W.-L.; Yang, W.; Cao, Y.; Roncali, J. *Macromolecular Rapid Communications* **2009,** 30, (17), 1484-1491.

Lombardo, C. J.; Glaz, M. S.; Ooi, Z.-E.; Vanden Bout, D. A.; Dodabalapur, A. *Physical Chemistry Chemical Physics* **2012,** 14, (38), 13199-13203.

Lombardo, C.; Dodabalapur, A. *Applied Physics Letters* **2010,** 97, (23), 233302-3.

Lombardo, C.; Danielson, E.; En Ooi, Z.; Dodabalapur, A. *Journal of Photonics for Energy* **2012,** 2, (1), 021007-1.

Lombardo, C.; Ooi, Z.-E.; Danielson, E.; Dodabalapur, A. *Organic Electronics* **2012,** 13, (7), 1185-1191.

Maturová, K.; van Bavel, S. S.; Wienk, M. M.; Janssen, R. A. J.; Kemerink, M. *Advanced Functional Materials* **2011,** 21, (2), 261-269.

McNeill, C. R.; Frohne, H.; Holdsworth, J. L.; Dastoor, P. C. *Nano Letters* **2004,** 4, (12), 2503-2507.

C. R. McNeill, B. Watts, L. Thomsen, W. J. Belcher, A. L. D. Kilcoyne, N. C. Greenham, P. C. Dastoor, *Small* 2006, *2*, 1432–1435.

B. E. McCandless, W. N. Shafarman, Chemical Surface Deposition of Ultra-thin Semiconductors, *U.S. Patent 6,537,845*, March 25, 2003.

C. R. McNeill, H. Frohne, J. L. Holdsworth, P. C. Dastoor, *Synthesis Methods* 2004, *147*, 101–104.

C. R. McNeill, H. Frohne, J. L. Holdsworth, J. E. Furst, B. V. King, P. C. Dastoor, *Nano Letters* 2004, *4*, 219–223.

Michels, M. A. J.; Janssen, R. A. J. *Nano Letters* **2005,** 5, (4), 579-583.

Mihailetchi, V. D.; Wildeman, J.; Blom, P. W. M. *Physical Review Letters* 2005, *94*, 126602.

Minemoto, T.; Hashimoto, Y.; Satoh, T.; Negami, T.; Takakura, H.; Hamakawa, Y. *Journal of Applied Physics* **2001,** 89, (12), 8327-8330.

Mozer, A. J.; Dennler, G.; Sariciftci, N. S.; Westerling, M.; Pivrikas, A.; Österbacka, R.; Juska, G. *Physical Review B* 2005, *72*, 035217.

Nelson, J. *Current Opinion in Solid State and Materials Science* **2002,** 6, (1), 87-95.

D. C. Olson, S. E. Shaheen, R. T. Collins, D. S. Ginley, *Journal of Physical Chemistry C* 2007, *111*, 16670–16678.

Ooi, Z. E.; Chan, K. L.; Lombardo, C. J.; Dodabalapur, A. *Applied Physics Letters* **2012,** 101, (5), 053301-5.

Ostrowski, D. P.; Glaz, M. S.; Goodfellow, B. W.; Akhavan, V. A.; Panthani, M. G.; Korgel, B. A.; Vanden Bout, D. A. *Small* **2010,** 6, (24), 2832-2836.

Ostrowski, D. P.; Lytwak, L. A.; Mejia, M. L.; Stevenson, K. J.; Holliday, B. J.; Vanden Bout, D. A. *ACS Nano* **2012,** 6, (6), 5507-5513.

R. Österbacka, A. Pivrikas, G. Juska, K. Genevicius, K. Arlauskas, H. Stubb, Current Applied Physics 2004, 4, 534.

Otsubo, T.; Aso, Y.; Takimiya, K. *Journal of Materials Chemistry* **2002,** 12, (9), 2565-2575.

V. Palermo, M. Palma, P. Samori, *Advanced Materials* 2006, *18*, 145–164.

V. Palermo, M. B. J. Otten, A. Liscio, E. Schwartz, P. A. J. de Witte, M.A. Castriciano, M.M. Wienk, F. Nolde, G. DeLuca, J.J.L.M. Cornelissen, R. A. J. Janssen, K. Müllen, A. E. Rowan, R. J. M. Nolte, P. Samorì, *Journal of the American Chemical Society* 2008, *130*, 14605–14614.

M. G. Panthani, V. Akhavan, B. Goodfellow, J. P. Schmidtke, L. Dunn, A. Dodabalapur, P. F. Barbara, B. A. Korgel, *Journal of the American Chemical Society* 2008, *130*, 16770–16777.

L. S. C. Pingree, O. G. Reid, D. S. Ginger, *Advanced Materials* 2009, *21*, 19–28.

L. S. C. Pingree, O. G. Reid, D. S. Ginger, *Nano Letters* 2009, *9*, 2946–2952.

T. Potlog, L. Ghimpu, P. Gashin, A. Pudov, T. Nagle, J. Sites, Solar Energy Materials and Solar Cells 2003, 80, 327.

Pivrikas, A.; Juscaronka, G.; Mozer, A. J.; Scharber, M.; Arlauskas, K.; Sariciftci, N. S.; Stubb, H.; Ouml; sterbacka, R. *Physical Review Letters* 2005, *94*, 176806.

Rajaram, S.; Armstrong, P. B.; Kim, B. J.; Fréchet, J. M. J. *Chemistry of Materials* **2009,** 21, (9), 1775-1777.

Ramanathan, K.; Contreras, M. A.; Perkins, C. L.; Asher, S.; Hasoon, F. S.; Keane, J.; Reid, O. G.; Rayermann, G. E.; Coffey, D. C.; Ginger, D. S. *The Journal of Physical Chemistry C* **2010,** 114, (48), 20672-20677.

Riede, M.; Mueller, T.; Tress, W.; Schueppel, R.; Leo, K. *Nanotechnology* **2008,** 19, (42), 424001.

R. Riehn, R. Stevenson, D. Richards, D.-J. Kang, M. Blamire, A. Downes, F. Cacialli, *Advanced Functional Materials* 2006, *16*, 469–476.

Repins, I.; Contreras, M. A.; Egaas, B.; DeHart, C.; Scharf, J.; Perkins, C. L.; To, B.; Noufi, R. *Progress in Photovoltaics: Research and Applications* **2008,** 16, (3), 235-239.

L. J. Rozanski, C. W. Cone, D. P. Ostrowski, D. A. Vanden Bout, *Macromolecules* 2007, *40*, 4524–4529.

M. J. Romero, A. J. Morfa, T. H. Reilly, J. van de Lagemaat, M. Al-Jassim, *Nano Letters*

2009, *9*, 3904–3908.

Scheer, R.; Walter, T.; Schock, H. W.; Fearheiley, M. L.; Lewerenz, H. J. *Applied Physics Letters* **1993,** 63, (24), 3294-3296.

Schwartz, E.; Palermo, V.; Finlayson, C. E.; Huang, Y.-S.; Otten, M. B. J.; Liscio, A.; Trapani, S.; González-Valls, I.; Brocorens, P.; Cornelissen, J. J. L. M.; Peneva, K.; Müllen, K.; Spano, F. C.; Yartsev, A.; Westenhoff, S.; Friend, R. H.; Beljonne, D.; Nolte, R. J. M.; Samorì, P.; Rowan, A. E. *Chemistry – A European Journal* **2009,** 15, (11), 2536-2547.

B. R. Saunders, M. L. Turner, *Adv. Colloid Interfaces* 2008, *138*, 1–23.

Seo, J. H.; Gutacker, A.; Walker, B.; Cho, S.; Garcia, A.; Yang, R.; Nguyen, T.-Q.;

Shaheen, S. E.; Brabec, C. J.; Sariciftci, N. S.; Padinger, F.; Fromherz, T.; Hummelen, J. C. *Applied Physics Letters* **2001,** 78, (6), 841-843.

Shin, W. S.; Jeong, H.-H.; Kim, M.-K.; Jin, S.-H.; Kim, M.-R.; Lee, J.-K.; Lee, J. W.; Gal, Y.-S. *Journal of Materials Chemistry* **2006,** 16, (4), 384-390.

Spanggaard, H.; Krebs, F. C. *Solar Energy Materials and Solar Cells* **2004,** 83, (2–3), 125-146.

Spano, F. C. *The Journal of Chemical Physics* **2005,** 122, (23), 234701-15.

Spano, F. C. *Chemical Physics* **2006,** 325, (1), 22-35.

Spano, F. C. *Accounts of Chemical Research* **2009,** 43, (3), 429-439.

K. Song, S. E. Watkins, Y. Geerts, M. M. Wienk, R. A. J. Janssen, T. Anthopoulos, H. Sirringhaus, M. Heeney, I. McCulloch, Journal of the American Chemical Society 2011, 133, 3272.

R. A. Street, S. Cowan, A. J. Heeger, Physical Review B 2010, 82, 121301.

Struijk, C. W.; Sieval, A. B.; Dakhorst, J. E. J.; van Dijk, M.; Kimkes, P.; Koehorst, R. B. M.; Donker, H.; Schaafsma, T. J.; Picken, S. J.; van de Craats, A. M.; Warman, J. M.; Zuilhof, H.; Sudhölter, E. J. R. *Journal of the American Chemical Society* **2000,** 122, (45), 11057-11066.

Tang, T.; Qu, J.; Müllen, K.; Webber, S. E. *Langmuir* **2005,** 22, (1), 26-28.

Teetsov, J.; Vanden Bout, D. A. *The Journal of Physical Chemistry B* **2000,** 104, (40), 9378-9387.

Teetsov, J.; Vanden Bout, D. A. *Langmuir* **2001,** 18, (3), 897-903.

N. M. Thantsha, E. Q. B. Macabebe, F. J. Vorster, E. E. van Dyk, *Phys. B-Condensed Matter* 2009, *404*, 4445–4448.

Thejo Kalyani, N.; Dhoble, S. J. *Renewable and Sustainable Energy Reviews* **2012,** 16, (5), 2696-2723.

Teunis van, W.; Jurjen, W.; Paul, W. M. B. *Semiconductor Science and Technology* **2006,** 21, (3), 387.

Todorov, T.; Mitzi, D. B. *European Journal of Inorganic Chemistry* **2010,** 2010, (1), 17-28.

Tour, J. M. *Accounts of Chemical Research* **2000,** 33, (11), 791-804.

Uchida, S.; Xue, J.; Rand, B. P.; Forrest, S. R. *Applied Physics Letters* **2004,** 84, (21), 4218-4220.

Vanden Bout, D. A.; Kerimo, J.; Higgins, D. A.; Barbara, P. F. *The Journal of Physical Chemistry* **1996,** 100, (29), 11843-11849.

Veldman, D.; Ipek, O. z.; Meskers, S. C. J.; Sweelssen, J. r.; Koetse, M. M.; Veenstra, S. C.; Kroon, J. M.; Bavel, S. S. v.; Loos, J.; Janssen, R. A. J. *Journal of the American Chemical Society* **2008,** 130, (24), 7721-7735.

Wada, T.; Kohara, N.; Nishiwaki, S.; Negami, T. *Thin Solid Films* **2001,** 387, (1–2), 118-122.

Wu, H.; Huang, F.; Mo, Y.; Yang, W.; Wang, D.; Peng, J.; Cao, Y. *Advanced Materials* **2004,** 16, (20), 1826-1830.

Xu, Y.; Yang, R.; Peng, J.; Mikhailovsky, A. A.; Cao, Y.; Nguyen, T.-Q.; Bazan, G. C. *Advanced Materials* **2009,** 21, (5), 584-588.

X. Yang, J. Loos, *Macromolecules* 2007, *40*, 1353–1362.

Yang, X.; Loos, J.; Veenstra, S. C.; Verhees, W. J. H.; Wienk, M. M.; Kroon, J. M.; Young, D.; Romero, M.; Metzger, W.; Noufi, R.; Ward, J.; Duda, A. *Progress in Photovoltaics: Research and Applications* **2003,** 11, (4), 225-230.Yang, R.; Xu, Y.;

Vita

Micah Glaz was born in Camarillo, CA and raised in Palmdale, CA. After graduating from Highland High School he attended college at the University of California, Davis working under Dr. William M. Jackson in the Department of Chemistry and Dr. Kate M. Scow in the Department of Land, Air and Water Resources. He graduated in 2006 with a bachelor of science in Chemistry. He worked for Air Toxics, Ltd. as an extractions chemist before attending the University of Texas at Austin in 2007 to begin his graduate studies in Physical Chemistry under Dr. David A. Vanden Bout.

Permanent email: micahglaz@gmail.com

This dissertation was typed by the author.